DOCTOR OF PHILOSOPHY

Pulsating flow studies in a planar wide-angled diffuser upstream of automotive catalyst monoliths

Mat Yamin, Ahmad Kamal

Award date:
2012

Awarding institution:
Coventry University

Pulsating Flow Studies in a Planar Wide-angled Diffuser Upstream of Automotive Catalyst Monoliths

By

Ahmad Kamal Mat Yamin

PhD

May 2012

PULSATING FLOW STUDIES IN A PLANAR WIDE-ANGLED DIFFUSER UPSTREAM OF AUTOMOTIVE CATALYST MONOLITHS

AHMAD KAMAL MAT YAMIN, M. Sc.

A thesis submitted in partial fulfilment of the University's requirements for the Degree of Doctor of Philosophy

May 2012

ACKNOWLEDGEMENTS

I would like to express my appreciation to my director of studies Professor S. F. Benjamin. His guidance, frequent discussions and sparkling ideas have given me great assistance throughout this project. I consider myself very fortunate to be counted as one of his students.

I also wish to thanks Dr. C. A. Roberts, my supervisor, for her encouragement, advice and enlightening discussions both on experiment and CFD techniques. Special appreciation is given to Mr. R. Gartside, Mr. L. King and Mr. C. Thorneycroft for their technical advice, assistance and craftsmanship in the manufacture of the test rigs for this project. Thanks are also addressed to M. Gall for assisting me in setting up the test rigs and the CFD models. The technical support from Dr. M. Hyde and Dr. S. Aleksandrova is also acknowledged. Many thanks to P. J. Skusiewicz for his kindness and friendship I enjoyed so much.

I am indebted to UTeM (Universiti Teknikal Malaysia Melaka) and MOHE (Ministry of Higher Education), Malaysia for providing the financial support throughout my study.

Last but not least, a special word of appreciation goes to my family for their love and encouragement throughout my study. Without their support, I would not have been able to complete this project.

ABSTRACT

Automotive catalytic converters are used extensively in the automotive industry to reduce toxic pollutants from vehicle exhausts. The flow across automotive exhaust catalysts is distributed by a sudden expansion and has a significant effect on their conversion efficiency. The exhaust gas is pulsating and flow distribution is a function of engine operating condition, namely speed (frequency), load (flow rate) and pressure loss across the monolith. The aims of this study are to provide insight into the development of the pulsating flow field within the diffuser under isothermal conditions and to assess the steady-state computational fluid dynamics (CFD) predictions of flow maldistribution at high Reynolds numbers.

Flow measurements were made across an automotive catalyst monolith situated downstream of a planar wide-angled diffuser in the presence of pulsating flow. Cycle-resolved Particle Image Velocimetry (PIV) measurements were made in the diffuser and hot wire anemometry (HWA) downstream of the monoliths. The ratio of pulse period to residence time within the diffuser (J factor) characterises the flow distribution. During acceleration the flow remained attached to the diffuser walls for some distance before separating near the diffuser inlet later in the cycle. Two cases with J ~ 3.5 resulted in very similar flow fields with the flow able to reattach downstream of the separation bubbles. With J = 6.8 separation occurred earlier with the flow field resembling, at the time of deceleration, the steady flow field. Increasing J from 3.5 to 6.8 resulted in greater flow maldistribution within the monoliths; steady flow producing the highest maldistribution in all cases for the same Re.

The oblique entry pressure loss of monoliths were measured using a one-dimensional steady flow rig over a range of approach Reynolds number ($200 \leq Re_a \leq 4090$) and angles of incidence ($0^o \leq \alpha \leq 70^o$). Losses increased with α and Re at low mass flow rates but were independent of Re at high flow rates being 20% higher than the transverse dynamic pressure.

The flow distribution across axisymmetric ceramic 400 cpsi and perforated 600 cpsi monoliths were modelled using CFD and the porous medium approach. This requires knowledge of the axial and transverse monolith resistances; the latter being only

applicable to the radially open structure. The axial resistances were measured by presenting uniform flow to the front face of the monolith. The transverse resistances were deduced by best matching CFD predictions to measurements of the radial flow profiles obtained downstream of the monolith when presented with non-uniform flow at its front face.

CFD predictions of the flow maldistibution were performed by adding the oblique entry pressure loss to the axial resistance to simulate the monolith losses. The critical angle approach was used to improve the predictions, i.e. the oblique entry loss was limited such that the losses were assumed constant above a fixed critical angle, α_c. The result showed that the perforated 600 cpsi monolith requires the entrance effect to be restricted above $\alpha_c = 81^o$, while the losses were assumed constant above $\alpha_c = 85^o$ for the ceramic 400 cpsi monolith. This might be due to the separation bubble at the monolith entrance being restricted by the smaller hydraulic diameter of the perforated monolith thus limiting the oblique entry loss at the lower incidence angle.

TABLE OF CONTENTS

LIST OF TABLES

LIST OF FIGURES

LIST OF ABBREVIATIONS AND SYMBOLS

Abbreviations

1-D	One-dimensional
2-D	Two-dimensional
3-D	Three-dimensional
Al_2O_3	Aluminium oxide
Ce	Cerium
CFD	Computational fluid dynamics
CCC	Closed-couple catalyst
CO	Carbon monoxide
CO_2	Carbon dioxide
cpsi	Cells per square inch
CR	Contraction area ratio
HC	Hydrocarbons
H_2O	Water
H-P	Hagen-Poiseuille relationship
HWA	Hot-wire anemometry
K-W	Küchemann and Weber
LES	Large eddy simulation
LDV	Laser doppler velocimetry
M-T	Moore and Torrence
N_2	Nitrogen
NO_x	Oxides of nitrogen
Nd-YAG	Neodymium-doped yttrium aluminium garnet
Pt	Platinum
PIV	Particle image velocimetry
RANS	Reynolds-averaged Navier-Stokes
Rh	Rhodium
RPM	Revolution per minute
SIMPLE	Semi-Implicit Method for Pressure-Linked Equations
TWC	Three-way catalytic converter
UBC	Under body catalyst

VFM Viscous flow meter

Symbols

A	Coefficient in equation (1.9)
A_1	Inlet area, m^2
A_2	Outlet area, m^2
b	Width of the 2-D diffuser, m
C	A constant used in equation (1.5), dimensionless
C_{pe}	Static pressure coefficient at the point of maximum pressure in the nozzle, dimensionless
C_{pi}	Static pressure coefficient at the point of minimum pressure in the nozzle, dimensionless
d_{diff}	Diffraction limited particle image diameter, μm
d_h	Hydraulic diameter
d_{image}	Particle image diameter, μm
d_p	Particle diameter, μm
f	Pulsation frequency, Hz
$f_\#$	Lens F-number, dimensionless
f_{app}	Apparent friction Fanning factor, dimensionless
$f\mathrm{Re}_c$	friction Fanning factor for fully developed flow, dimensionless ($f\mathrm{Re}_c$ = 14.227 for a square cross-section)
F_e	Parameter used in nozzle design, dimensionless
F_i	Parameter used in nozzle design, dimensionless
G_e	Parameter used in nozzle design, dimensionless
G_i	Parameter used in nozzle design, dimensionless
g	Standard gravity, 9.81 m/s^2
H_1	Half inlet height of 2-D nozzle
H_2	Half outlet height of 2-D nozzle
J	$U_{in}/(L_d.f)$, dimensionless
K_{Obl}	Non-dimensional oblique entry pressure loss, dimensionless
$K_{Obl,Pred}$	Non-dimensional theoretical oblique entry pressure loss, dimensionless
$K(\infty)$	Additional pressure loss term for developed flow, dimensionless ($K(\infty)$ = 1.43 for a square cross-section)

L	Length of the monolith, m
L_d	Length of the diffuser, m
L_t	Total length of the nozzle, m
M	Magnification, dimensionless
$\dot{m}_1$	Inlet mass flow rate, kg/s
$\dot{m}_2$	Outlet mass flow rate, kg/s
N	Number of image, dimensionless
n	Exponent in equation (1.9)
P_L	Monolith pressure drop, Pa
P_{Obl}	Oblique entry loss, Pa
P_{s1}	Static pressure at point 1, Pa
P_{s2}	Static pressure at point 2, Pa
P_i	Inertial resistance, kg/m^4
P_v	Viscous resistance, kg/m^3s
ΔP	Pressure drop across the monolith, Pa
ΔP_m	Pressure loss due to fully developed flow across monolith, Pa
ΔP_d	Pressure loss due to developing flow at the entrance of the channels + pressure loss due to fully developed flow across monolith, Pa
Re	Reynolds number based on upstream inlet pipe diameter, dimensionless
Re_a	Approach Reynolds number ($\rho U_1 d_h/\mu$), dimensionless
Re_c	Channel Reynolds number ($\rho U_c d_h/\mu$), dimensionless
T	Pulse period, s
t	Time, s
U_1	Mean inlet velocity, m/s
U_2	Mean outlet velocity, m/s
U_c	Mean channel velocity, m/s
U_{Mean}	Cycle-averaged mean velocity, m/s
u_{Mean}	Cycle average velocity, m/s
u	Axial velocity, m/s
U	Velocity magnitude, $\sqrt{u^2 + v^2}$, m/s
v	Transverse velocity, m/s
W_1	Inlet height, m
W_2	Outlet height, m

X^+	Non-dimensional monolith length, dimensionless
y	Distance from the wall or distance across the monolith, m
y^+	Normalized distance from the wall, dimensionless

Greek symbols

α	Angle of incidence, degrees
α_c	Critical angle of incidence, degrees
α_1	Kinetic energy correction factors for inlet velocity U_1, dimensionless
α_2	Kinetic energy correction factors for exit velocity U_2, dimensionless
ϵ	Turbulent dissipation rate, m^2/s^3
κ	Turbulent kinetic energy, m^2/s^2
μ	Dynamic viscosity of the fluid, kg/m.s
υ	Kinematic viscosity of the fluid, m^2/s
θ	Half included diffuser angle, degress
ε	Porosity of the substrate, i.e. the ratio of the open area to the total cross sectional channel area, dimensionless
ρ	Density of fluid, kg/m^3
ρ_p	Particle density, kg/m^3
λ	Wavelength, nm

Subscript

a	Approach
c	Critical
d	Diffuser
e	Point of wall-velocity maximum
i	Point of wall-velocity minimum
h	Hydraulic
p	Particle
1	Inlet plane
2	Exit plane
∞	Far upstream and downstream

CHAPTER 1: INTRODUCTION

1.1 Introduction

Internal combustion engines are currently being manufactured at high volume for vehicle propulsion systems due to their advantages of higher top speed, longer range and the convenience of refuelling compared to alternative power plants (Electric vehicles, hybrids, etc.). However, they produce a relatively large amount of pollution that has a damaging impact on the environment and human health. Therefore government legislation to control emission limits, such as the European Union standards, has become increasingly stringent. This is illustrated in Table 1.1 which shows emission regulations for passenger cars. The emission standards were originally specified in Directive 70/220/EEC followed by a number of amendments, i.e. Euro1 (1992), Euro 2 (1996), Euro 3 (2000) and Euro 4 (2005). In 2007, this Directive was superseded by Regulation 715/2007 which ratified Euro 5 (2008, Current legislation) and Euro 6 (2014). To meet these standards catalytic converters are used extensively on both diesel and petrol vehicles.

Table 1.1: EU Emission Standards for Passenger Cars
(Source: http://www.dieselnet.com/standards/eu/ld.php)

Catalysts comprise of either ceramic or metallic monoliths featuring thousands of parallel channels through which exhaust gas flows with hydraulic diameter of ~1 mm to provide ample surface area for high conversion efficiency. Monoliths are typically washcoated with aluminium oxide (Al_2O_3) that supports the noble metals such as Platinum (Pt) and Rhodium (Rh) to reduce the activation energy so that the reaction can occur at lower temperatures and higher rates. Pt oxidises carbon monoxide (CO), and unburned hydrocarbons (HC) to carbon dioxide (CO_2) and water (H_2O) respectively, whilst Rh reduces nitrous oxides (NO_x) to nitrogen (N_2) and the released oxygen atoms are used for oxidation reactions. This so-called three-way catalyst used on gasoline engines provides simultaneous conversion around the stoichiometric air to fuel ratio point, i.e. 14.6. To broaden the conversion efficiency during rich/lean perturbations, Cerium (Ce) has been a part of the noble metal mixture to provide oxygen storage.

The monoliths have been designed to have as short a length as possible to minimize the system backpressure and thus their diameter is larger than the upstream exhaust pipe. A large expansion is always employed to connect the inlet pipe to the front face of the catalyst due to the space constraints. This leads to flow separation at the inlet to the diffuser and a non-uniform distribution of flow in front of the monolith. Figure 1.1 shows a typical assembly featuring a monolith situated downstream of a wide-angled diffuser along with a representation of the flow field within the diffuser with steady flow. The exhaust stream is shown separating at the diffuser inlet forming a jet which traverses the body of the diffuser before spreading rapidly as it approaches the monolith. Part of the flow recirculates and part enters the monolith. This situation leads to premature deactivation of the catalyst in areas of high flow, reduction in conversion efficiency, increase in system pressure loss and poor utilisation of the catalyst. Testing and simulation work are often carried out to optimise the exhaust flow distribution and improve the efficiency of the catalyst systems. The latter is based on computational fluid dynamics (CFD) techniques where virtual prototypes of designs can be analyzed.

Stricter emission legislation has meant monoliths are now located closer to the engine in order to reduce light-off times. These so called closed-couple catalysts (CCC) often use either a cascade architecture or high cell density monoliths. The cascade design is a combination of CCC and under body catalyst (UBC); the latter is

located underneath the vehicle, a metre or two downstream of the engine to reduce emissions post-light-off. The monolith with high cell density provides similar benefits in conversion efficiency as its surface area is increased and the diffusion path for the emissions to reach the noble metals is reduced. However, this approach has some drawbacks in terms of cost and system backpressure. With metallic monoliths, the flat and corrugated foils can be perforated before being wound together. Figure 1.2 shows the radially open structure. This so-called perforated monolith permits radial flow between adjacent channels thus providing more uniform flow across the catalyst and therefore improving its utilization.

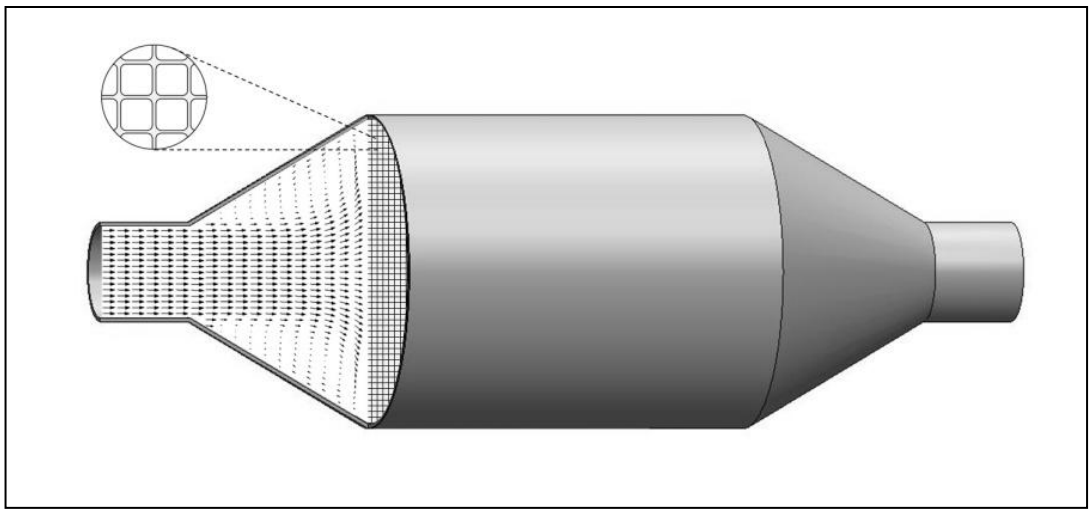

Figure 1.1: Schematic showing catalyst configuration comprising a monolith in an exhaust system, catalyst channels and flow separation in the diffuser

For either type of configuration, the flow distribution in the front of the monolith is affected by the strong pulsating flow as the exhaust gas enters the diffuser volume. Engine test bed evaluation of different converter geometries and configurations is very time consuming and expensive. Hence, considerable effort has been directed towards (i) investigating the flow maldistribution under the effect of the pulsating flow and (ii) optimising the flow using CFD studies. The following section discusses previous work relating to pulsating flow and CFD studies in automotive catalysts. The latter is confined to steady cases since the predictions of pulsating flow are less common.

Figure 1.2: Radially open structure
(Source: http://www.emitec.com/en/technology/pe-design-gb.html)

1.2 Literature review

Over the years many experimental and numerical studies have been reported on the flow maldistribution within automotive catalysts. In this section a brief review is presented with the emphasis on the effect of pulsating flows and steady-state CFD studies, the main subjects of this thesis.

1.2.1 Experimental studies

As described in the previous section, packaging constraints cause flow maldistribution within the monoliths due to separation at the entrance of the expansion. Many studies have been performed over the years to investigate the effect of system geometry on the flow distribution and converter performance; for example Howitt and Sekella (1974), Zygourakis (1989) and Weltens et al. (1993). Indeed, the degree of flow uniformity across the monolith is often used as an indicator for the acceptability of a particular design. The system geometry is often complex and the exhaust is pulsating and so interacting factors affect the distribution.

The easiest way to perform the parametric studies is by means of conducting investigations under non-pulsating or steady conditions which is justifiable for flow through UBC configurations. Under such conditions measurements can be made using steady flow rigs which permit a more comprehensive analysis of the flow field within the diffuser and the flow distribution across the monolith. The latter can be

obtained from hot wire anemometry (HWA) or pitot measurements at the rear of the monolith because the flow is unidirectional as it exits the channels. The upstream flow field can be obtained from Particle image velocimetry (PIV) measurements in the diffuser which also provides a useful database for comparison with CFD.

Within the research group at Coventry University, Clarkson (1995) studied the effect of expansion angle, Reynolds number and monolith length on the flow distribution within axisymmetric catalytic converters. The results showed that the flow maldistribution increases with increasing diffuser angle and Re. On the other hand, increasing the monolith length flattens the velocity profiles due to higher downstream resistance. Haimad (1997) investigated the effect of flow conditions at the inlet to the diffuser and found less maldistribution with uniform inlet flow in contrast to fully developed flow.

PIV measurements in the upstream diffuser have also been reported by several groups for steady flow. Shuai et al. (2001) examined diffuser and monolith designs and compared measurements with CFD predictions. In a recent study Turner et al (2011) similarly studied the flow field upstream of a diesel particulate filter. Ilgner et al (2001) made PIV measurements upstream of an auto-thermal gas reformer but significant image distortion due to wall curvature restricted the field of view where reliable data could be obtained. Using a planar diffuser optical distortion was minimised by Quadri et al (2009a). By comparing the upstream flow field (PIV) with that measured downstream of the monolith using HWA it was demonstrated that the monolith radically redistributes the flow as it enters the channels.

With the introduction of CCC designs, the steady flow analysis is inappropriate as the flow is highly pulsating. Such studies that have been performed for these systems have been made using either rigs or running engines e.g. Hwang et al (1995), Bressler et al (1996), Zhao et al (1997), Park et al (1998) and Benjamin et al (2006). Whilst of great practical importance they most often feature “production type” exhausts which are geometrically complex providing limited access for flow measurements.

To simplify the situation many studies have been conducted by incorporating a pulse generator into a stationary flow rig, often with simpler axisymmetric geometries. Benjamin et al. (2001) measured the effect of flow pulsations on the flow distribution within ceramic contoured monoliths by measuring the cycle-averaged flow distribution at the exit to the monoliths using HWA. Contoured monoliths were shown to be less sensitive to changes in flow rate and pulsation frequency when compared to a standard monolith.

Liu et al. (2003) investigated the effect of pulse shapes. Pulses with higher peak/mean ratio produced less maldistributed flow at all frequencies. Benjamin et al (2002) studied the effect of pulse frequency (16 - 100 Hz) and Re (2×10^4 - 8×10^4) on the flow distribution within monoliths of different lengths with 60^o and 180^o diffusers. Both cycle-averaged and phase-averaged velocity profiles were presented. Flow maldistribution within the monoliths was shown to be correlated with a non-dimensional parameter J (reciprocal of the Strouhal number) defined as the ratio of pulse period to residence time within the diffuser; as J increased the flow maldistribution also increased. Persoons et al. (2003) found a similar correlation between their measure of flow uniformity and a scavenging ratio S (defined in a very similar way to J) for the case of a more complex system geometry.

Whilst these studies were able to derive useful correlations between flow maldistribution and system parameters it is often difficult to interpret the findings in terms of processes within the diffuser itself. A few studies have been reported on the mechanisms of flow separation through simple open diffusers with pulsating and oscillating flows. However it should be kept in mind that conditions associated with exhaust after-treatment systems are somewhat different in several key aspects; the flow is essentially pulsating and the proximity of the monolith will have a significant effect on flow development in the diffuser. Smith and King (2007) and King and Smith (2011) obtained oscillating and pulsating PIV measurements in open planar diffusers. Their flow rig is capable of velocity oscillation amplitudes up to 50 m/s at frequencies of 7 to 120 Hz and steady flows up to 40 m/s. These are flow conditions approximately representative of engine exhausts. In Smith and King (2007) PIV measurements were made on diffusers with included angles up to 30^o. With oscillating flow, during the acceleration part of the cycle, the flow remained attached in spite of very large adverse pressure gradients. During deceleration the flow was

more prone to separation. Oscillating and pulsating flows at the same point of the cycle (start of deceleration) were also compared. For both cases flow is shown separating near the diffuser inlet but is able to reattach in the former case.

In a recent study King and Smith (2011) reported on further observations made under oscillating conditions. Separation was found to begin high in the diffuser and propagated downward; the flow was able to remain attached further into the diffuser with larger Re, small displacement amplitudes and smaller diffuser angles. They also showed that the extent of flow separation grows with a non-dimensional displacement amplitude, a function of the maximum velocity and pulsation frequency. The expression is similar to J introduced by Benjamin et al (2002).

1.2.2 CFD studies

The Reynolds-averaged Navier-Stokes (RANS) approach is widely used in commercial CFD packages to solve the flow field upstream and downstream of the monolith. RANS modelling has been tested against data obtained from an asymmetric planar diffuser with 10 degree expansion angle. Using this data base, Iaccarino (2001) showed that the κ-ϵ model did not detect the separation completely and gave poor agreement with measurements. However the V2F model captured the separation zone and agreed well with the measurements of the mean velocity. In particular, the turbulent intensity was well predicted before the separation zone, however, the model underestimated the level of kinetic energy after the reattachment; similar behaviours can be observed in the V2F calculations conducted by Durbin (1995), the 3-dimensional, unsteady large-eddy simulation LES computations by Kaltenbach et al. (1999) and recent predictions conducted by Apsley and Leschziner (2000) using quadratic and cubic non-linear κ-ϵ models. It was suggested that this was due to the presence of strong three-dimensional effects after the flow separation.

The multi-channel monolith can be represented as a porous medium with a distributed resistance applied to the entire region to lessen the computational demands. For non-perforated monoliths, the resistance can be described by Hagen-Poisieulle (H-P) relationship in the flow direction for fully developed laminar flow

since the maximum channel Re typically varies between 400 and 1500. According to Benjamin et al. (1996), the H-P relationship loses validity for X^+ less than 0.02 and a better approach is to use Shah's correlation (1978) which takes into account the additional pressure loss due to its developing boundary layer. The flow is made unidirectional by applying large transverse resistances. For a radially open structure (Perforated monoliths), knowledge of the resistances in the directions perpendicular to the flow is required. Kaiser et al. (2007) measured asymmetric radial flow downstream of the perforated monolith by placing an eccentric orifice plate with an off-centre circular hole at its front face. They developed a three-dimensional CFD model and the transverse resistances were deduced by adjusting them to have the same measured values of pressure drop and flow distribution. The results showed that the perforations in the transverse direction help the flow to spread more favourably within the monolith. Similar patterns have been reported by Lotti et al. (2005) for the close-coupled system.

CFD studies on axisymmetric catalyst systems at Re = 6 x 10^4 have been conducted by Benjamin et al. (1996). They showed that using the H-P formulation to describe the resistance within the porous medium under-predicted the flow maldistribution within the catalysts due to the inadequate description of the pressure loss since the flow enters the channels obliquely resulting in an extra pressure loss as illustrated in Figure 1.1.

Benjamin et al. (2001) have attempted to improve predictions of the flow maldistribution across the axisymmetric systems for a range of Reynolds number ($2x10^4$ < Re < $8x10^4$), by incorporating a theoretical expression, derived by Küchemann and Weber (1953) (abbreviated as K-W), for oblique entry losses in heat exchangers. They showed that the entrance effect improves the prediction of maximum velocities which is an important piece of information as catalyst aging is associated with areas of high mass flow rate. On the other hand, the simulations under-predicted the minimum velocities due to the entrance effect being too high at very large angles of attack occurring at radial positions approximately two-thirds towards the periphery resulting in much higher secondary peaks near the wall. Similar findings have been observed by Benjamin et al. (2003) for the close-coupled system at Re = $6x10^4$.

The oblique entry loss correlations have been experimentally derived for flow entering catalyst monolith channels using different methodologies to verify the theoretical expression. Persoon et al. (2008) conducted the measurements by presenting swirling flow upstream of the monolith and found the losses were approximately half of those deduced by K-W based on measurements up to $\alpha = 33^{o}$.

Quadri et al. (2009b) measured the oblique entry pressure loss by introducing the flow at an angle of incidence to the front face of the monolith over a range of Reynolds numbers ($200 \leq Re_a \leq 2200$) and angle of incidence ($0^{o} < \alpha < 75^{o}$). They found that the K-W expression does not agree well with the data and the correlation derived by Persoon et al. (2008) was not applicable for the entrance effect at high incidence. An expression formulated by Moore and Torrence (1977) based on the finned tube bundles, underestimated the losses at low angle.

An improved correlation for the entrance effect was found as a function of Reynolds number and angle of incidence ($0 - 75^{o}$). The correlation was incorporated into a CFD code to predict the flow maldistribution across an axisymmetric system using the V2F model for a range of Reynolds numbers ($4x10^{4} < Re < 8x10^{4}$). They found it is necessary to restrict the oblique entry loss above a critical angle of 81^{o} to improve the predictions at regions of the monolith where the angle of incidence was greater than this. This methodology was justified by assuming that the separation bubble due to the oblique entry flow at the channels' entrance has a maximum size and the degree of flow separation is essentially restricted by the channel height.

Table 1.2 and Table 1.2 summarise the descriptions of the formulations for monolith and oblique entry losses in this section. The non-dimensional oblique pressure loss coefficient is defined as

$$K_{Obl} = \frac{P_{Obl}}{(1/2)\rho {U_1}^2} \qquad (1.1)$$

where P_{Obl} is the oblique entry pressure loss and U_1 is the approach velocity.

Table 1.2: Formulations for monolith pressure drops

Formulation	Definition
Hagen-Poisieulle (H-P)	$\frac{\Delta P_m}{L} = 2f\mathrm{Re}_c\frac{\mu U_c}{{d_h}^2}$ (1.2)
Shah (1978)	$\frac{\Delta P_d}{(1/2)\rho {U_c}^2} = (f_{app}\mathrm{Re}_c)(4X^+) = (f\mathrm{Re}_c)(4X^+) + K(x)$ (1.3) $X^+ = \frac{X}{d_h \mathrm{Re}_c}$ (1.4) $f_{app}\mathrm{Re}_c = \frac{3.44}{\sqrt{X^+}} + \frac{(f\mathrm{Re}_c) + \frac{K(\infty)}{4(X^+)} - 3.44/\sqrt{X^+}}{1 + C(X^+)^{-2}}$ (1.5)

Table 1.3: Formulations for oblique entry pressure losses

Küchemann and Weber (1953) or K-W	$K_{Obl} = \sin^2\alpha$ (1.6)
Moore and Torrence (1977) or M-T	$K_{Obl} = (1 - \cos\alpha)^2$ (1.7)
Persoon et al. (2008)	$K_{Obl} = 0.459\sin^2\alpha$ (1.8)
Quadri et al. (2009b)	$K_{Obl} = A\mathrm{Re}_a^{n(\alpha)}\sin^2\alpha$ (1.9)

	A	*n(α)*
$30^o \leq \alpha \leq 45^o$	0.021	0.5
$55^o \leq \alpha \leq 70^o$	0.18	0.24
$\alpha = 75^o$	0.525	0.1

1.3 Aims and objectives

The key findings from previous work are summarized. The pulsating flow study across a simple diffuser is still under researched and not representative of automotive catalyst systems as the proximity of the monolith affects the flow development in the diffuser as shown in Figure 1.1. Benjamin et al. (2001), Benjamin et al (2002), Liu et al. (2003) and Persoons et al. (2003) have established useful correlations between system parameters and flow maldistribution within automotive catalysts under

pulsating flow. However, without measurements within the diffuser it is difficult to interpret the exit flow distribution in terms of processes within the diffuser.

An improved methodology to predict flow maldistribution for axisymmetric catalyst systems has been presented by Quadri et al. (2009b), i.e. by restricting the oblique entry loss above a critical angle of 81^{o}. However, the approach has not been experimentally validated and the oblique entry loss was derived over a low range of Re. In addition the methodology has yet to be implemented at higher Reynolds number and for other monolith types, such as perforated monoliths. The axisymmetric modelling is promising to deduce the transverse resistances of these structures which lessen the computational demand.

This thesis aims to provide insight into the development of the pulsating flow field for a relatively simple yet representative after-treatment configuration under isothermal conditions and to assess the steady-state CFD predictions of flow maldistribution at high Reynolds numbers.

The specific objectives are as follows:

a. To measure the pulsating flow fields within a planar diffuser situated upstream of the monolith at two different of J factors using cycle-resolved PIV technique.
b. To investigate the oblique entry pressure losses at high Reynolds number and to determine the critical angle.
c. To assess the empirical entrance effect and the critical angle approach by comparing the CFD predictions of flow maldistribution to the measurements at high Reynolds number.
d. To develop a CFD model of an axisymmetric perforated monolith catalyst and to investigate the impact of perforation on the flow maldistribution.

1.4 Thesis outline

Chapter 2 describes the apparatus and methods which encompass the experimental flow rigs and instrumentation used in this thesis. Chapter 3 discusses the steady and the phase-resolved PIV measurements across a two-dimensional automotive monolith catalyst. Results from the measurements of the oblique entry pressure loss for flow entering the monolith are presented in Chapter 4. Chapter 5 provides the pressure drop data and flow maldistribution within the ceramic and perforated monolith catalysts. In Chapter 6, the CFD methodology and predictions of flow distribution across axisymmetric systems are presented. Finally, a summary of the main conclusions and recommendations for future work is covered in Chapter 7.

CHAPTER 2: EXPERIMENTAL APPRATUS AND METHODS

2.1 Introduction

This chapter describes the experimental methodology used to carry out the isothermal measurements that are presented in this thesis and the test conditions are summarized in Appendix A. The air flow rigs were built in-house and are described in this chapter so as to provide a useful reference for future work. The uncertainty analysis in the instrumentation is provided at the end of this chapter.

2.2 Catalyst flow laboratory

Measurements were made in the Coventry University Catalyst Flow Laboratory under isothermal conditions. The ambient air was pumped into large receivers using an air compressor unit. A 55 kW electric motor drives the screw-type compressor to deliver 8.24 m^3/min compressed air and provides a pressure differential of 13 bar (gauge). The compressed air is supplied to the flow rig from two receivers via a cock valve. A 12 litres cylindrical plenum is located upstream of the flow rig to suppress the reverse flow during the pulsating flow study. The isothermal condition was achieved as the amount of air that was used for every measurement is far less than the capacity of the receivers. The temperature at the monolith outlet was continuously monitored and was normally about 20^{o}C. During an experiment they varied by at most 2 – 3^{o}C.

Mass flow rates were determined using a custom built viscous flow meter (abbreviated as VFM) located upstream of the flow rigs as shown in Figure 2.1. The VFM contains a multi-channel monolith across which the pressure drop ΔP is measured using a digital manometer. According to equation (1.2) in Table 1.2, the mass flow rate is proportional to the pressure drop for fully developed laminar flow and thus forms a basis for VFM calibration. To obtain the mass flow rates, a flexible pipe connected the VFM to a plenum chamber attached to a converging nozzle to produce a uniform flow. Velocity profiles at the exit of the nozzle were measured along horizontal and vertical axes for different ΔP.

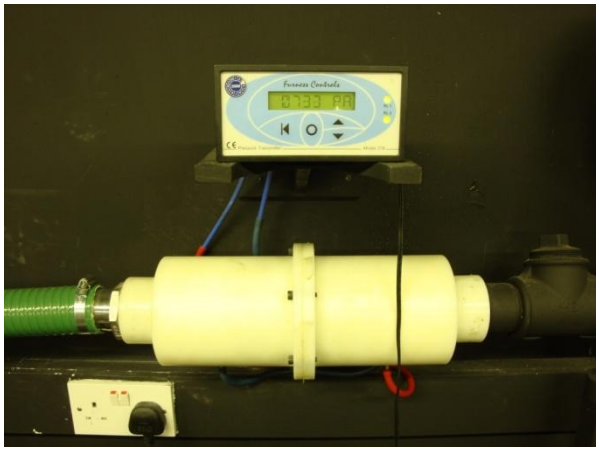

Figure 2.1: Viscous flow meter

The mass flow rate was calculated by integration across each of the four radii and averaging results. Figure 2.2 illustrates the calculation method. The cross-section of the nozzle outlet was divided into concentric annuli of width δr and area δA at a mean radius r_i. If the velocity through an annulus is u_i, the mass flow rate $\delta \dot{m}$ is $\rho(2\pi r_i \delta r)u_i$. Hence, the total mass flow rate through the nozzle, $\dot{m}$ becomes

$$\dot{m} = 2\pi\rho\Sigma u_i r_i \delta r \qquad (2.1)$$

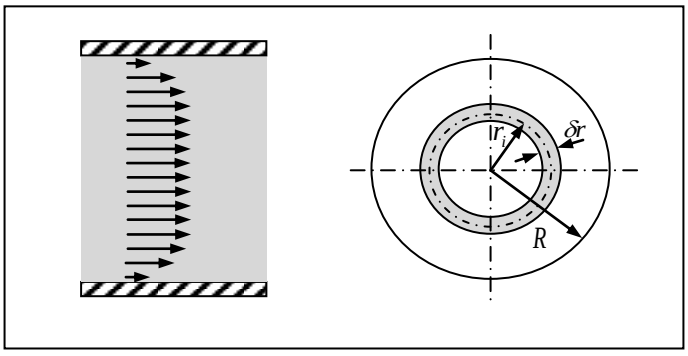

Figure 2.2: Integration method for calculating the total mass flow rate

The VFM was calibrated for low and high pressure lines using a digital manometer model FCO16 (Range ± 199.9 mm H_2O and accuracy of ±1 digit or ±1% of the reading) and FCO318-4W (Range ± 10 kPa and accuracy of ±0.25% of the reading) from Furness Controls respectively. Figure 2.3 and Figure 2.4 show the profiles are approximately one dimensional. Figure 2.5 and Figure 2.6 show the VFM calibration charts of low pressure line and high pressure line for mass flow rates up to ~24 g/s

and ~218 g/s respectively with linear correlations between pressure drops and mass flow rates as well as mean velocities.

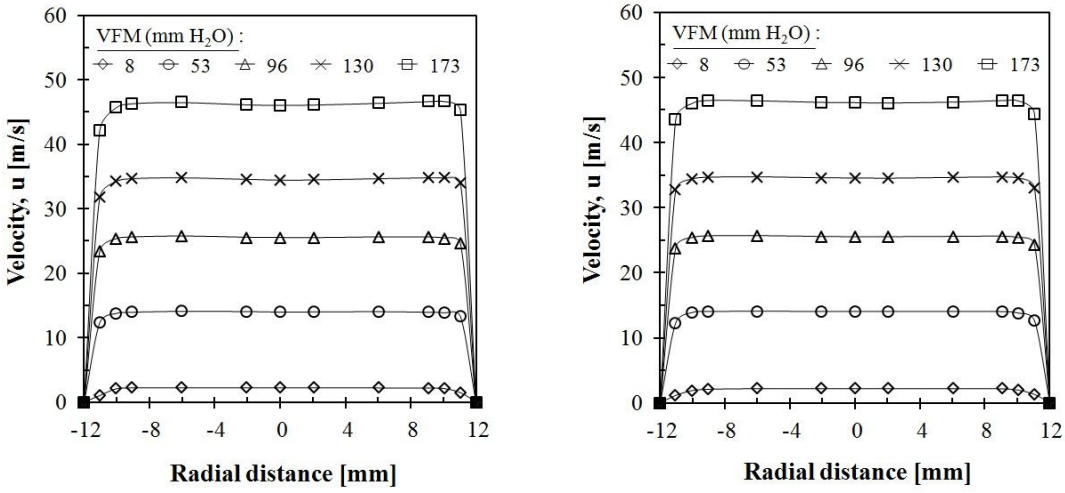

(a) x-axis (b) y-axis

Figure 2.3: Velocity profiles along 24 mm diameter nozzle exit; x and y refer to orthogonal axes at the nozzle exit

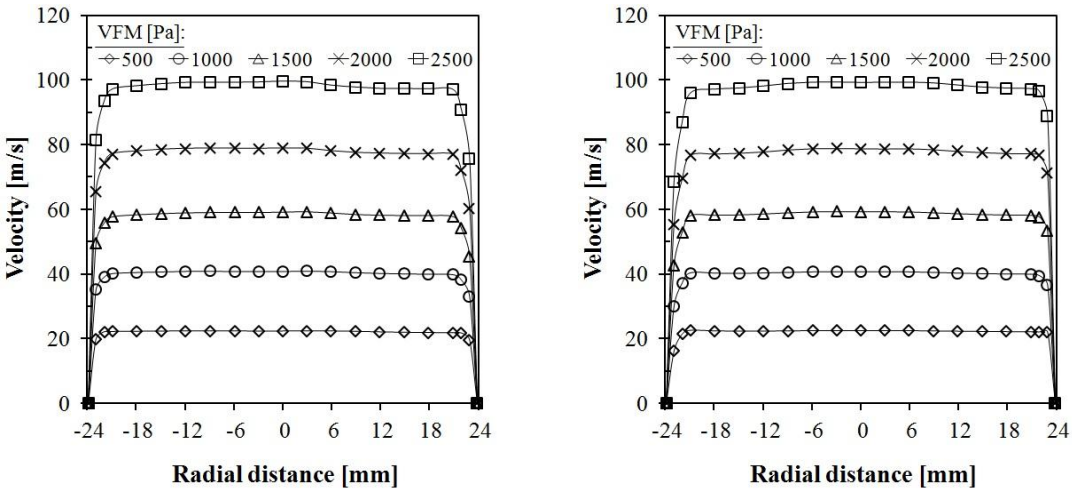

(a) x-axis (b) y-axis

Figure 2.4: Velocity profiles along 48 mm diameter nozzle exit; x and y refer to orthogonal axes at the nozzle exit

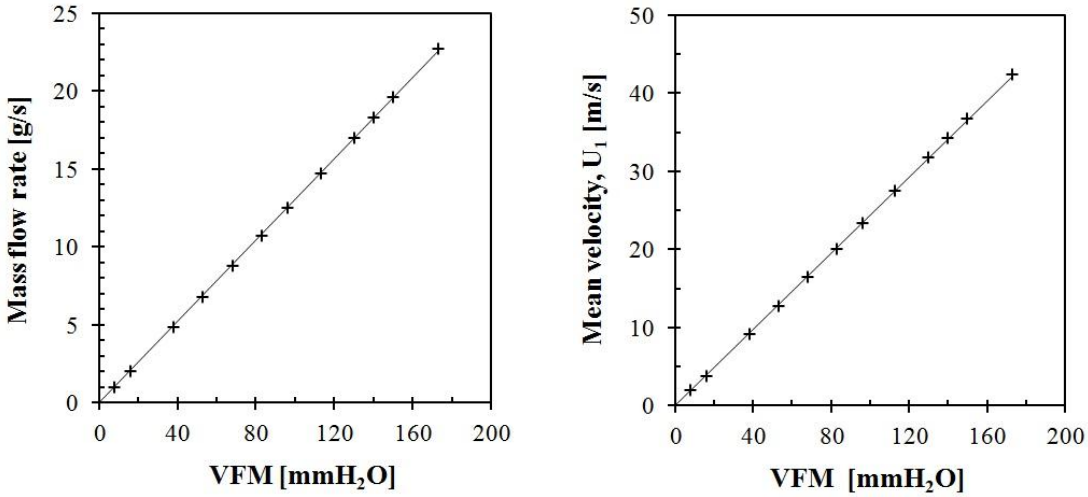

(a) Mass flow rate (b) Mean velocity

Figure 2.5: VFM correlations for low-pressure line

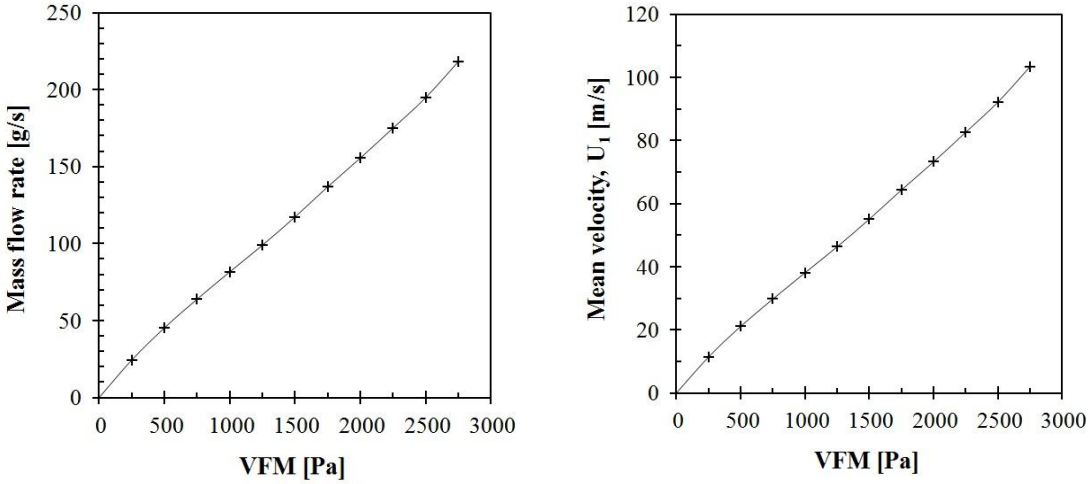

(a) Mass flow rate (b) Mean velocity

Figure 2.6: VFM correlations for high-pressure line

2.3 Pulsating flow measurements

This section presents the methodology to perform cycle-resolved 2-D PIV measurements made in a wide-angled planar diffuser placed upstream of automotive catalyst monoliths presented with pulsating flow. The planar diffuser enables maximum optical access and simplifies measurement as the flow is approximately two-dimensional. Whilst idealised it is expected to show many of the flow features common to more complex systems and, to a first approximation, may be thought of as representative of oval or elliptical designs. A similar approach has been used by Quadri et al. (2009a) for steady flow measurements. Measurements were conducted at pulsation frequency of 50Hz and 100Hz to represent exhaust pulses of a 4 cylinder engine at 1500 RPM and 3000 RPM respectively.

2.3.1 Isothermal 2-D flow rig

Figure 2.7 shows the schematic and photograph of the rig. It was supplied with compressed air via a plenum (2) incorporating a flow straightener (3) placed upstream of an axisymmetric nozzle (4). Pulsations are generated by a pulse generator (5) placed downstream of the nozzle as used in previous studies (Benjamin et al. 2002). A 12 mm aluminium housing contains a cast iron plate with four regularly spaced openings. A DC motor rotates the plate which periodically interrupts the flow. Timing signals and rotational speed are obtained from an optical-electrical transducer (± 5V output voltage) within the rotor assembly. Non-pulsating flow was achieved by fixing the rotor in one of its fully open positions. A flow straightener (6) was placed downstream of the rotor and a resonator box (7) was installed in order to shape the pulses. The plenum (8) mixes seeding particles supplied by a particle generator (9); the flow straightener (10) in the plenum minimizes any swirl components.

The rectangular nozzle (11) produces a uniform velocity profile into the planar diffuser (12). Thus well-defined inlet boundary conditions are generated suitable for CFD modelling. The nozzle has been designed with a contraction ratio of 4, i.e. the ratio of the nozzle entrance to its outlet, using Morel's method (1977) as in Appendix B. The method provides design procedures to compute the nozzle length

and shape with knowledge of acceptable adverse pressure gradients in the vicinity of the nozzle inlet and outlet to prevent flow separation based on analytical equations of inviscid (non-viscous) flow.

The diffuser is integrated with an inlet duct of 24 mm length. As shown in Figure 2.8(a), the diffuser section has inlet dimensions W_1 (= 24 mm) x b (= 96 mm), a total included angle of approximately 60^o, length L_d = 48 mm and an outlet W_2 (= 78 mm) x b (= 96 mm). Two-dimensional flow was generated by taking the width to inlet height ratio (b/W_1) greater than 4 to 5 (Schetz et. al. (1999)). The walls of the whole diffuser were made from crown glass with wall thicknesses of 6 mm for maximum optical access. Figure 2.8(b) shows the photograph of the nozzle-diffuser assembly.

Cordierite monoliths (13) of length 27 mm or 100 mm were positioned downstream of the diffuser. The unwashcoated monoliths had channel hydraulic diameter of 1.12 mm, a nominal cell density of 62 cells/cm^2 or 400 cpsi and a porosity, ε of 0.77. An outlet sleeve (14) of length 50 mm was used to minimise disturbance by surrounding air when making HWA measurements at the exit from the monolith.

(a)

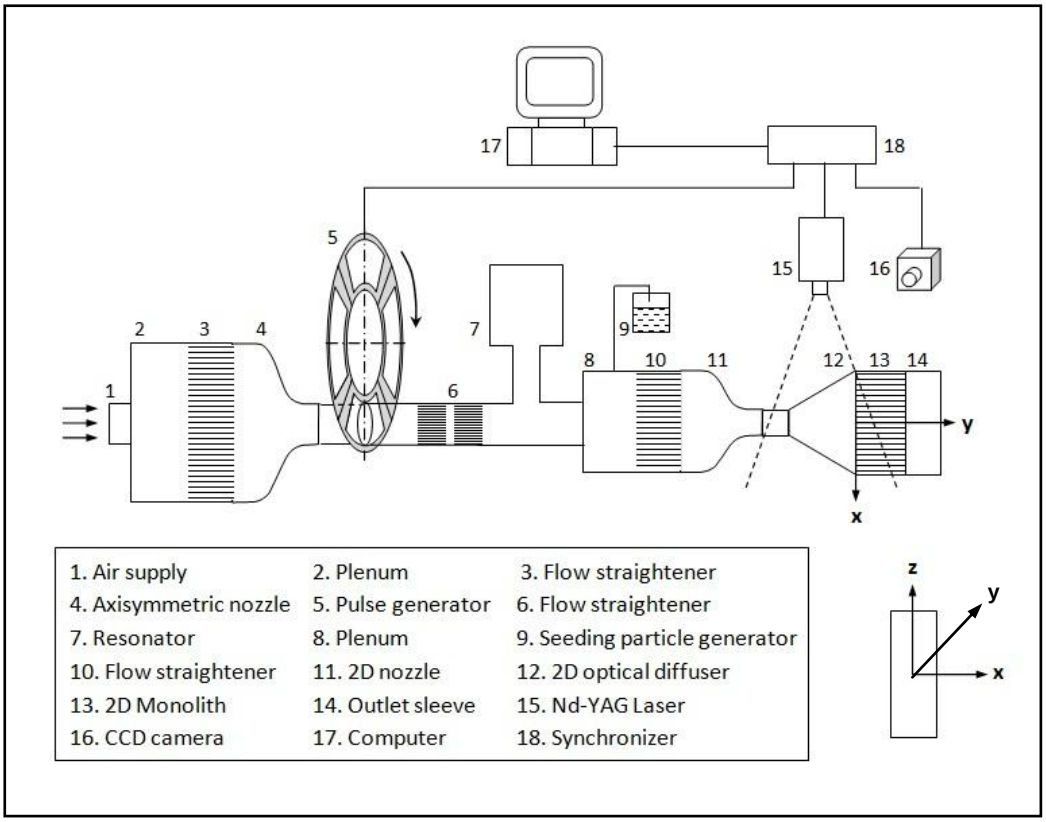

1. Air supply	2. Plenum	3. Flow straightener
4. Axisymmetric nozzle	5. Pulse generator	6. Flow straightener
7. Resonator	8. Plenum	9. Seeding particle generator
10. Flow straightener	11. 2D nozzle	12. 2D optical diffuser
13. 2D Monolith	14. Outlet sleeve	15. Nd-YAG Laser
16. CCD camera	17. Computer	18. Synchronizer

(b)

Figure 2.7: Pulsating flow rig; (a) Schematic, (b) Photograph; x and z refer to axes in the plane of the nozzle outlet; the dotted lines in (a) represent the field of illumination emanating from the laser.

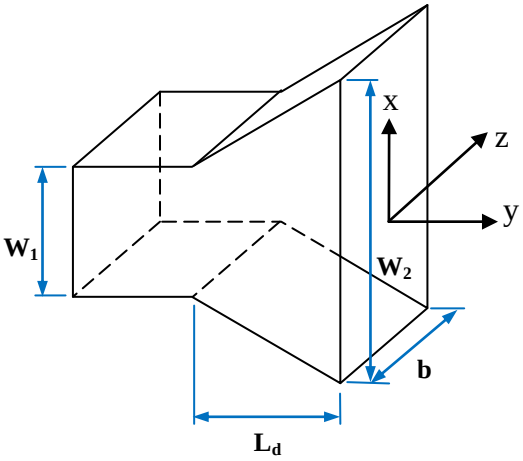

a) Dimensional diagram

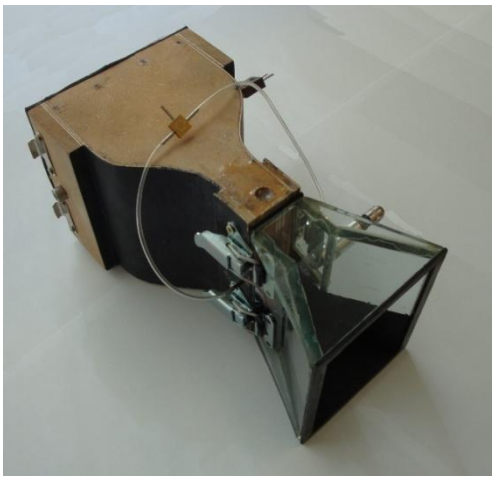

b) Nozzle-diffuser assembly

Figure 2.8: 2-D diffuser; (a) Dimensional diagram (b) Nozzle-diffuser assembly

A TSI IFA 300 constant temperature HWA system was used to measure the axial velocity within the inlet to the diffuser and at the exit of the monolith. The probes were 5 µm platinum plated tungsten wires (Dantec 55 P11) and were calibrated using a fully automatic TSI 1129 calibration rig. A 1MHz 4 channel 12 bit A/D converter was used to convert the IFA output voltage (within ± 5 V) to a digital signal, which was then processed by the ThermalPro software to compute the instantaneous and time-averaged velocity. The signals were channelled into the A/D board of the IFA 300 system. Signals from the pulse generator and HWA probe were logged simultaneously. Using the timing signal HWA velocity profiles were derived by phase-averaging over 50 cycles. A sampling size of 2048 points was used with the sampling rate of 2 kHz for flow pulsating frequencies of 50Hz and 4 kHz for 100Hz to obtain 40 data points per cycle.

2.3.2 Pulse shapes

A Helmholtz resonator was used to shape the pulses. The resonator consists of a narrow neck attached to a large cavity whereas the 'springiness' of the air inside the cavity causes the volume of air in and near the neck to vibrate. By changing the relative dimensions between these components a resonator can be tuned to a particular frequency

$$f = \frac{c}{2\pi}\sqrt{\frac{A}{Vl}} \tag{2.2}$$

where c = speed of sound, i.e. 343.2 m/s, A is the neck area (m^2), V is the volume (m^3), and l the neck length (m).

Figure 2.9 and Figure 2.10 show the effect of the resonator on the pulse shapes observed in the centre of the inlet duct at f = 50 Hz and 100 Hz using HWA. The dimensional data of the resonator is listed in Table 2.1. The low frequency resonator reflects the waves at 100 Hz to cancel out the resonant frequency at 50 Hz and thus approximately generates sinusoidal pulse shapes. The high frequency resonator smoothes the pulse shapes with minimum variations of peak/mean ratio. A further examination shows that the velocity traces correspond well with the PIV data as presented in Appendix C.

Table 2.1: Dimensional data of the Helmholtz resonators

A (cm^2)	L (cm)	V (cm^3)	f (Hz)
4.524	100	1.331	100
22.062	50	8.228	400

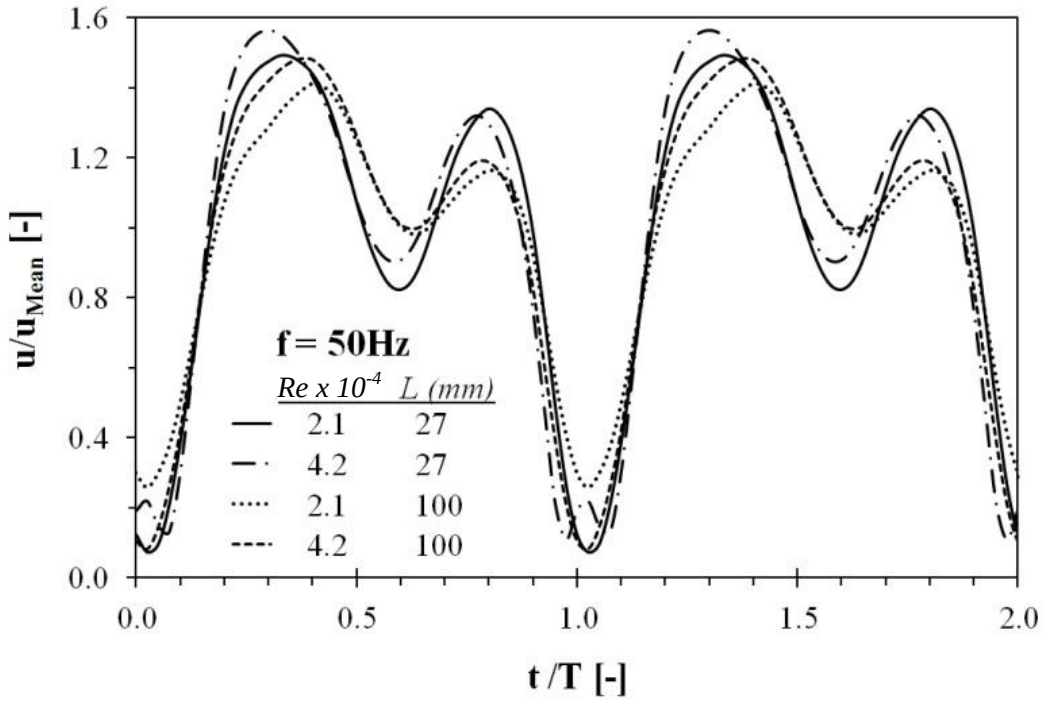

(a) without resonator

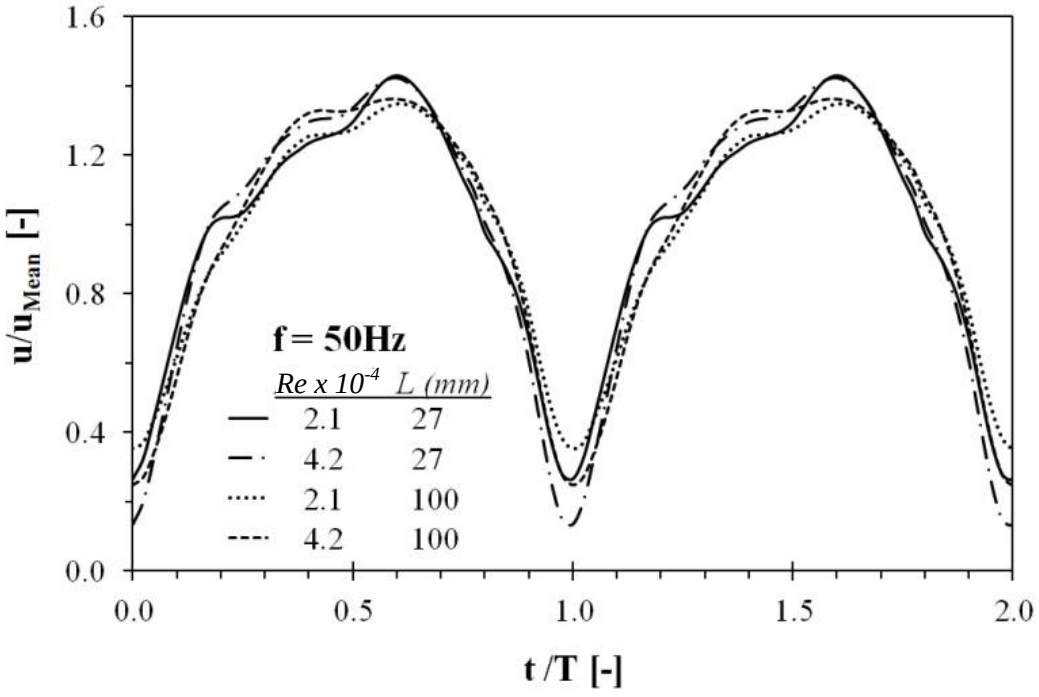

(b) with resonator 100 Hz

Figure 2.9: Inlet pulse shapes at 50 Hz without and with resonator 100Hz; t is the time, T pulse period, u phase-averaged velocity, u_{Mean} cycle-averaged velocity, L refers to the monolith length.

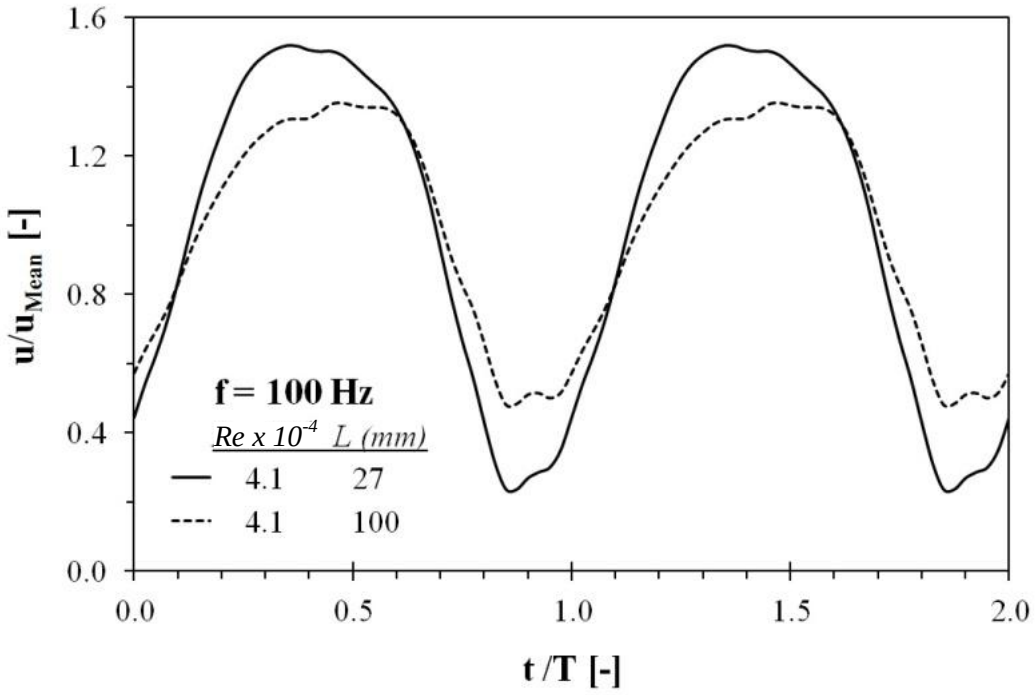

a) without resonator

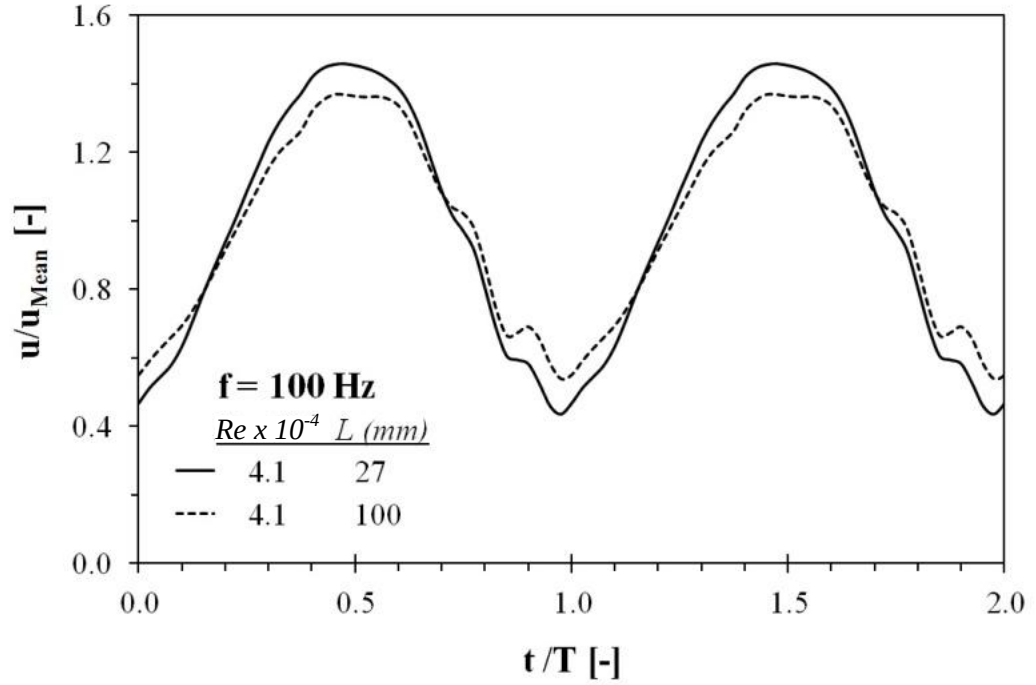

b) with resonator 400 Hz

Figure 2.10: Inlet pulse shapes at 100 Hz without and with resonator 400Hz; t is the time, T pulse period, u phase-averaged velocity, u_{Mean} cycle-averaged velocity

2.3.3 PIV setup

The PIV technique was introduced in the late 80's and relies on the basic principle of distance over time to yield velocity. Figure 2.7(a) illustrates the main components of the system comprising seeding particle generator, Nd-YAG laser, CCD camera, computer and synchronizer. The system is capable of non-intrusively mapping the whole velocity fields from one measurement and thus reducing data acquisition times over point-based measurement methods, i.e. Laser Doppler Velocimetry (LDV) and HWA.

As shown in Figure 2.7(a), the light reflecting particles are illuminated twice by the Nd-YAG laser (15) with a known time separation and a CCD camera (16) is used to capture the two successive exposures of the illuminated plane in two images. This technique is known as "frame-straddling". The INSIGHT-3G software on the computer (17) divided each image into a grid with each interrogation window encompassing 7 – 15 particles and all particles are assumed to have the same velocity. The synchronizer (18) provides the timing and sequencing of the image acquisition such that the displacement of the fastest particles is less than one-quarter of the window size. In contrast to the autocorrelation technique, the knowledge of image sequence eliminates the directional ambiguity and the cross-correlation technique is used to determine the dominant displacement of a group particles within a small interrogation region. The timing signal from the flow chopper was used to phase-lock the PIV acquisition. A trigger delay generator integrated in the software gives the capability to shift the relative acquisition times within a cycle.

Generally the seeding particles should be small enough to faithfully follow the flow and big enough to scatter sufficient light for the camera to detect them. The latter involves setups in recording hardware as discussed later in this section. The first requirement is satisfied when the settling velocity of the particle under gravity, u_∞ is negligible compared to the dominant velocity. According to Stokes drag formula

$$u_\infty = \frac{g{d_p}^2(\rho_p - \rho_f)}{18\mu} \tag{2.3}$$

where d_p and ρ_p are the particle diameter and density respectively, and μ and ρ_f are the fluid viscosity and density respectively.

To minimize u_∞ due to the large density difference, the flow was seeded by a six-jet atomizer as shown in Figure 2.11 at 25 psi to produce very small olive oil droplets with a mean diameter of approximately 0.6 μm. The high-velocity jet draws the oil up through a tube and breaks them up into droplets. The smaller droplets atomize and exit through an outlet tube, while the larger impinge on the spherical impactor. Figure 2.12 shows the droplet distribution from the atomizer used with olive oil. From equation (2.3), $u_\infty \sim 9.8$ μm/s ($\rho_p \approx 913$ kg/m^3) and hence negligible compared to the actual velocity.

Figure 2.11: Photo (left) and schematic (right) TSI Model 9306 Six-Jet Atomizer (Courtesy TSI Incorporated)

Figure 2.12: Particle size distribution of an olive oil aerosol (Courtesy TSI Incorporated)

The pulsed doubled cavity Nd-YAG laser was used as a light source to illuminate the flow. Table 2.2 lists the main specification of the Solo 120 laser supplied by New Wave Research Inc. A short burst of light energy within 3 – 5 ns from the 120 mJ Nd-YAG lasers could produce an instantaneous power in the range of 24 - 40 MW. This demonstrates why this pulsed laser has been classified as a safety hazard. A cylindrical lens of -25 mm focal length was combined with a spherical lens of 500 mm to transform the circular beam from the Nd-YAG laser into an approximately 1 mm thickness light-sheet at a stand-off distance of 0.5 m to illuminate the seeded flow.

Table 2.2: Specification of the Solo 120 laser

Energy	2 x 120 mJ/pulse at 532 nm
Repetition rate	15 Hz
Beam diameter	4.5 mm
Pulse width	3-5 ns
Relative jitter	1 ns, with respect to external trigger

A 4-megapixel CCD camera with a resolution of 2048 x 2048 pixel (1 pixel = 7.4 μm) and maximum sampling frequency of 17 Hz was used to capture the flow field. The camera coupled with a 105 mm lens was placed 0.8 m from the measurement plane to cover a 80 mm x 60 mm region of interest resulting in a magnification factor, M of 0.155. The calibration factor was obtained by acquiring an image of a plane black target placed at the measurement plane inside the optical diffuser as defined by the laser sheet as shown in Figure 2.13. The calibration target is an equally spaced grid of white dots with the distance between the dots being 5 mm. From the recorded image, the distance between 10 dots was 1049 pixels and gave a calibration factor of 47.66 x 10^{-3} mm/pixel. As recommended, the laser was set to low power (60 mJ) during the calibration process and triggered externally using the INSIGHT 3G software.

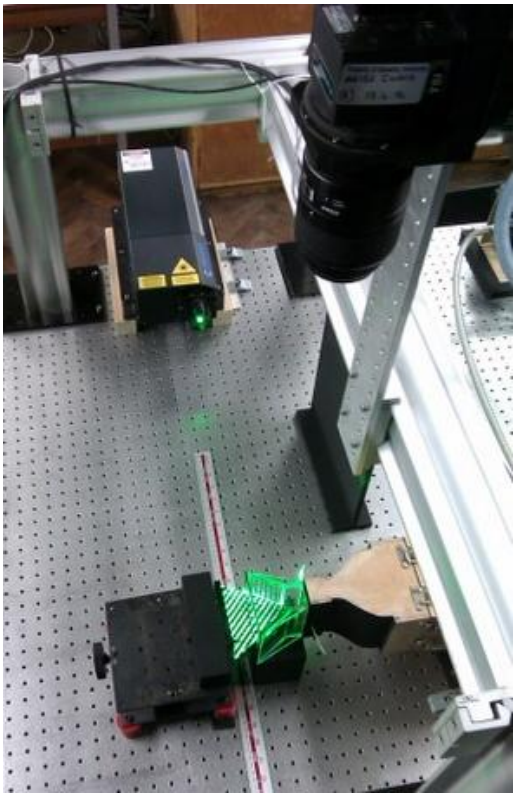

Figure 2.13: Two-dimensional calibration

The displacement of the particle is measured based on the center of each particle image and thus the f-number ($f_{\#}$) of 11 was used to achieve a particle image diameter above 2 pixels so that the center of the particle could be more accurately determined (Rafell and Willert(1998)). Figure 2.14 shows the distribution of the image diameter of particles d_{image} determined by particle size d_p, magnification M, and diffraction limited particle image diameter d_{diff}

$$d_{image} = \sqrt{(M.d_p)^2 + {d_{diff}}^2} = \sqrt{(M.d_p)^2 + (2.44 \cdot f_{\#} \cdot \lambda(M+1))^2} \qquad (2.4)$$

where λ is the wavelength of the incident light (532 nm). The PIV data were processed using INSIGHT-3G software and plotted using Techplot 11. The recursive Nyquist method with an initial grid size of 64 x 64 and a final grid of 32 x 32 pixels yielded 95% of valid vectors in each field and vector resolution of 0.76 x 0.76 mm. This method processes the PIV images in two passes using an image shifting algorithm. In the first processing pass the images are processed on an un-shifted interrogation window to give the vector fields with 50% window overlap. Based on the vector fields obtained in the first processing pass the interrogation windows of

the second frame are shifted to provide a strong correlation in the second processing pass.

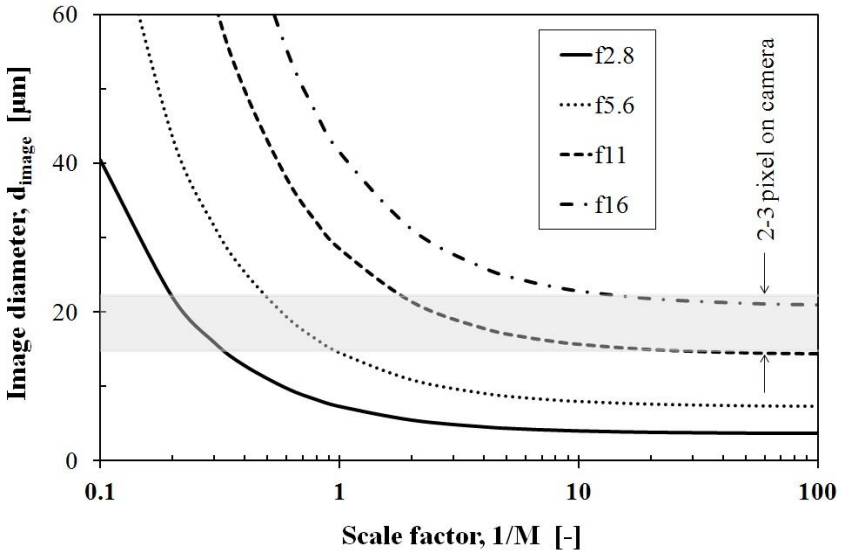

Figure 2.14: Effect of aperture stop (f-number) on image size

Figure 2.15 shows PIV data processing to obtain correct velocity measurements. The white grid marks the interrogation window size of 32 x 32 pixel as shown in Figure 2.15(a). The laser sheet has been obstructed at the sealed joints at the inlet and outlet of the diffuser, in the latter case up to a distance of 2.5 mm from the front face of the monolith. These regions were excluded from the process by masking the region of interest with a white dash line (Figure 2.15(b)). The raw vector map obtained from the cross-correlation process was validated to identify the bad vectors by comparing with neighbouring vectors. All vectors over the median value of 5 x 5 neighbours were marked as invalid with red colour in Figure 2.15(c). Figure 2.15(d) shows the vector statistics of the validated vectors. In this case, low seed density may lead to the invalid (spurious) vectors. The bad vectors were replaced by interpolation from the neighbouring vectors. Finally the vector fields were smoothed by a low-pass filter and the substituted vectors are indicated by yellow colour. The flow fields were averaged based on 100 vector fields. The investigation of the effect of sample size is provided in Appendix D.

(a)

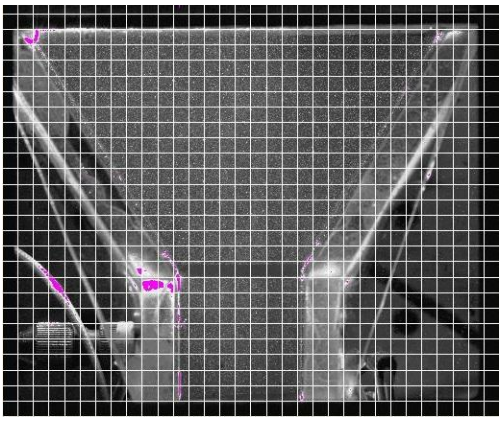

(b)

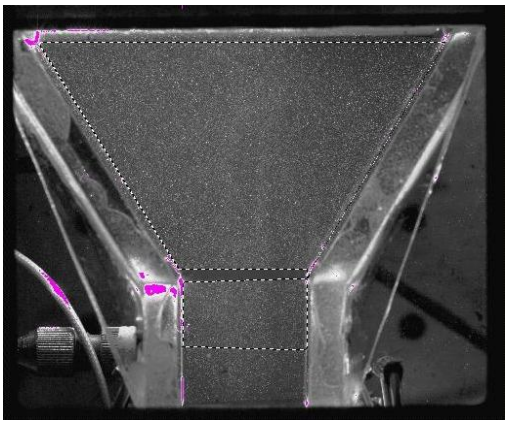

(c)

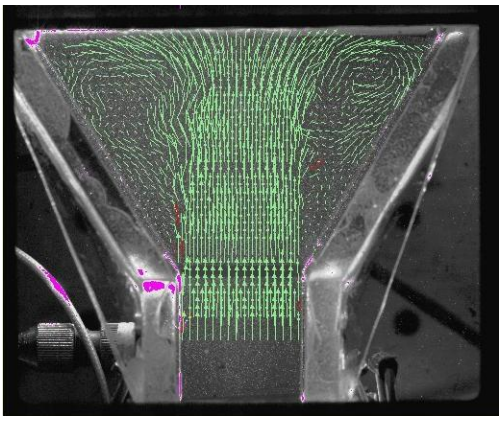

(d)

	U	V	Velocity Magnitude
Mean	-0.065463	-2.787107	2.787876
Standard Deviation	1.013616	2.636895	2.825002
Minimum	-4.259152	-6.226481	7.543835
Maximum	3.936070	2.976996	4.935094
Total Vector Count	4,373		
Good Vector Count	4,332		
Bad Vector Count	41		
Interpolated Vector Count	0		
Good Vector Percent	99.062		
Bad Vector Percent	0.937		
Interpolated Vector Percent	0		

(e)

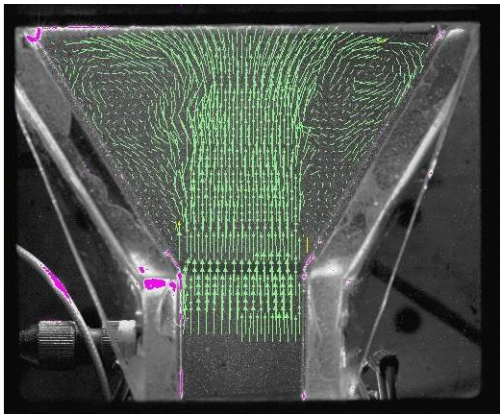

(f)

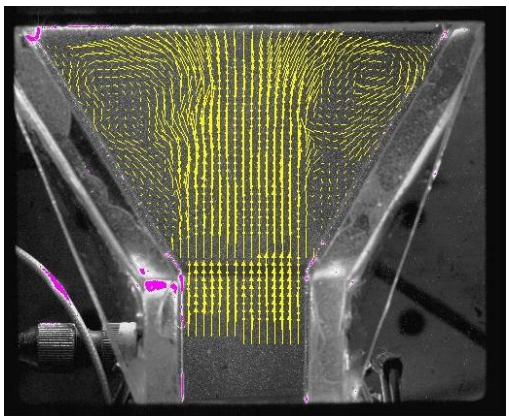

Figure 2.15: Post processing of PIV data.

Note: (a) Image (b) Masking (c) Local validation (d) Vector statistics (e) Interpolation and (f) Low-pass filter

2.4 Oblique flow loss measurements

This section presents the method to investigate the oblique flow losses at high flow rates and to validate the critical angle approach. Quadri et al. (2009b) developed an isothermal one-dimensional steady flow rig capable of introducing the flow to the front face of the monolith over a range of angles of incidence ($0 – 75^{o}$) as shown in Figure 2.16. The pipes with inside diameter of 55 mm were used to channel a uniform flow from the nozzle to the cylindrical monolith with diameter of 300 mm. Clearly the maximum angle of incidence is only restricted by the size of the pipe or monolith. Therefore this approach is promising for this study.

Figure 2.16: Schematic diagram of the flow rig for measuring oblique flow loss (Quadri et al. (2009b))

Replacing the pipes with a smaller diameter for the measurements at high angles of incidence is less expensive than manufacturing a larger diameter of cylindrical monolith. Hence, the measurements at high Reynolds number can be achieved for the same mass flow rate when the size of the pipe is reduced. However, a new contracting nozzle is required to match with the replacement pipes. The contour of the nozzle was constructed based on Morel's procedure (1975) as attached in Appendix E. A pipe with inside diameter of 24 mm has been chosen for the measurements providing a maximum angle of incidence of 85^{o} as shown in Figure 2.17. The velocity profiles downstream of the nozzle indicate that the flow is approximately uniform as shown in Figure 2.3.

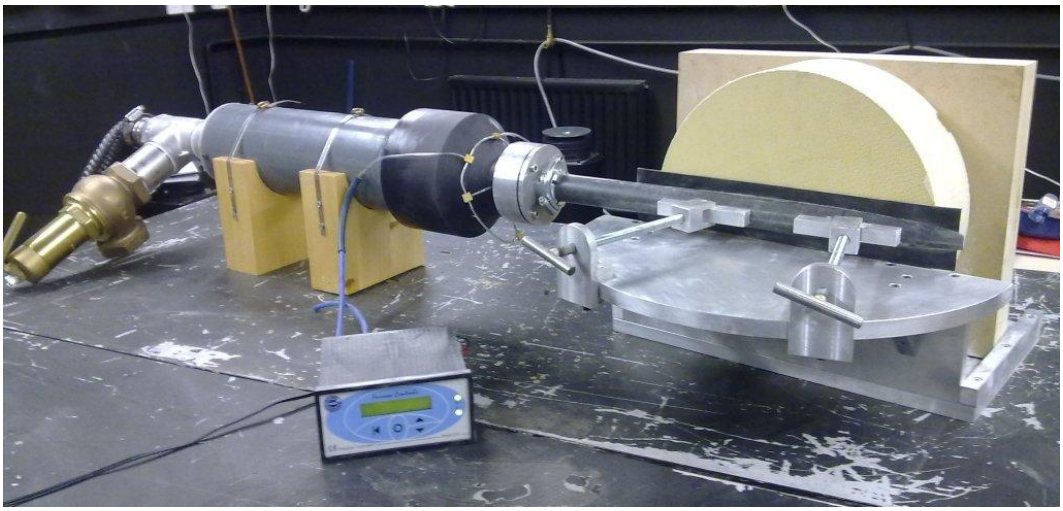

Figure 2.17: Isothermal one-dimensional steady flow rig

The methodology to measure the oblique flow loss using the rig has been described by Quadri et al. (2009b). With reference to Figure 2.16 the total pressure loss across the system is given by:

$$P_{t1} - P_{t2} - P_L - P_{Obl} = 0 \tag{2.5}$$

with

$$P_{t1} = P_{s1} + \frac{1}{2}\rho\alpha_1 {U_1}^2 \tag{2.6}$$

$$P_{t2} = P_{s2} + \frac{1}{2}\rho\alpha_2 {U_2}^2 \tag{2.7}$$

where P_{t1} and P_{t2} are the total pressure at points 1 and 2 respectively; P_L is the monolith pressure loss at zero incidence; P_{Obl} is oblique entry pressure loss; P_{s1} and P_{s2} are the static pressure at 1 and 2; α_1 and α_2 are the kinetic energy pressure correction factors at 1 and 2; and U_1 and U_2 are the average velocities at 1 and 2. α_1 and α_2 are unity for one-dimensional flow. The additional pressure loss due to the length of the upstream pipe that varies with α is implicitly considered when measuring the pressure differential Ps_1-Ps_2.

Hence, equation (2.5) can be rewritten, assuming α_1 and α_2 are 1.0

$$P_{Obl} = (P_{s1} - P_{s2}) + (1/2)\rho\left({U_1}^2 - {U_2}^2\right) - P_L \tag{2.8}$$

A viscous flow meter was located upstream the test rig to monitor the mass flow rate and thus the upstream velocity U_1 can be determined from Figure 2.5. The velocity downstream of the monolith U_2 was obtained from the law of conservation of mass.

$$\dot{m}_1 = \dot{m}_2$$

$$\rho A_1 U_1 = \rho A_2 U_2$$

$$U_2 = \frac{A_1 U_1}{A_2} \tag{2.9}$$

The pressure drop across the monolith was obtained from the measurements at zero incidence ($U_1 = U_2$) and thus equation (2.8) is reduced to

$$P_L = (P_{s1} - P_{s2}) \tag{2.10}$$

The magnitude of P_L is essentially a function of the mean channel velocity $U_c = (U_2/\varepsilon)$ and thus it is smaller when α increases.

With reference to Figure 2.16, equation (2.8) is normalized using the dynamic head based on U_1 to give a non-dimensional oblique pressure loss defined as

$$K_{Obl} = \frac{P_{Obl}}{(1/2)\rho U_1} = \frac{(P_{s1} - P_{s2}) + (1/2)\rho\left(U_1{}^2 - U_2{}^2\right) - P_L}{(1/2)\rho U_1{}^2} \tag{2.11}$$

The measurements were conducted for cordierite monoliths of length 17 mm and 27 mm. The unwashcoated monoliths had channel hydraulic diameter of 1.12 mm, a nominal cell density of 62 cells/cm^2 or 400 cpsi and a porosity of 0.77. The differential static pressure measured between stations 1 and 2 was obtained using a digital manometer model FCO318-4W (± 10 kPa) from Furness Controls.

2.5 Flow studies of axisymmetric systems

This section describes the experiments to provide the data for simulation work presented in Chapter 6. The porous medium technique was used to model the flow distribution for ceramic and perforated monoliths. It requires knowledge of axial and transverse monolith resistance. The latter is applicable for the perforated monolith to simulate the radial flow within the structure. Section 2.5.1 describes the measurement techniques to obtain the axial resistance, i.e. by presenting uniform flow to the front face of the monolith. Section 2.5.2 presents the configurations of geometrically different flow assemblies (i.e. Assemblies 1, 2 and 3) to obtain the hot-wire velocity profiles downstream of the monoliths. Assembly 1 provides the data to validate CFD predictions of the flow maldistribution within the monolith. The transverse resistance was deduced from Assemblies 2 and 3 to establish the generality of the method, i.e. by best matching the radial flow profiles to the CFD predictions. The ceramic 400/6 monolith of 400 cpsi cell density and of 6 mil wall (i.e. 0.006" or 0.15 mm) featured unwashcoated channels of square cross-section with a hydraulic diameter of 1.12 mm, and a porosity of 0.77, whilst the perforated 600/1.5 monolith of 600 cpsi cell density and of 1.5 mil wall (i.e. 0.0015" or 0.04 mm) featured washcoated channels of sinusoidal cross-section with hydraulic diameter of 0.71 mm, and a porosity of 0.75.

2.5.1 Monolith axial resistance

Monolith resistances of the two different structures were measured using two different techniques. Figure 2.18 illustrates the experimental configurations. Since the flow is unidirectional within the ceramic monolith, a uniform flow from the nozzle exit of diameter 55 mm was presented across a small section of its front face (Figure 2.18(a)). For the radially open monolith, it is necessary to provide a uniform velocity over the whole front face of the structure. Figure 2.18(b) shows the experimental setup for this measurement with a narrow angled 10 degree-diffuser employed to connect the nozzle exit to the front face of the monolith. As the flow expands within the diffuser, the boundary layer develops along the walls and thus a flow straightener was installed to improve the flow uniformity as shown in Figure

2.19. With this setup the flow profiles downstream of the monolith showed that the flow within the structure is acceptably uniform as illustrated in Figure 2.20. The pressure loss was measured using a digital manometer model FCO318-4W (± 50.00 kPa) from Furness Controls and was deduced from the average of four-point pressure tapings situated upstream of the monolith.

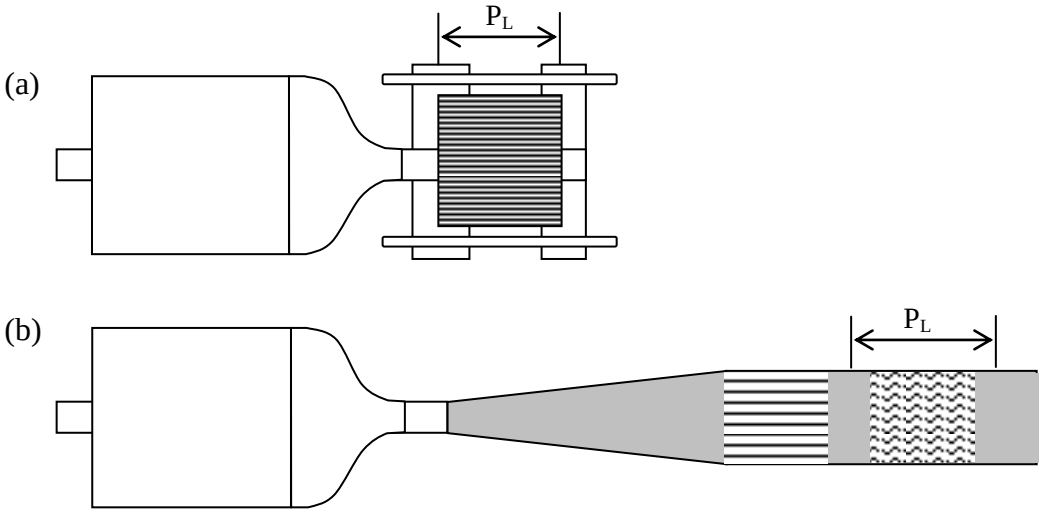

Figure 2.18: Axial resistance measurements (Schematic); a) Ceramic b) Perforated

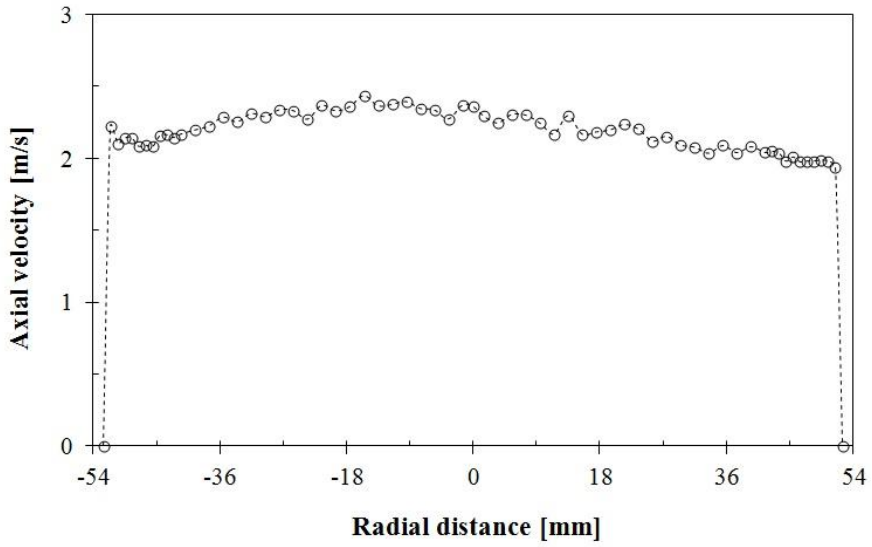

Figure 2.19: Velocity profile downstream of 10^o diffuser at Re = 1.9 x 10^4

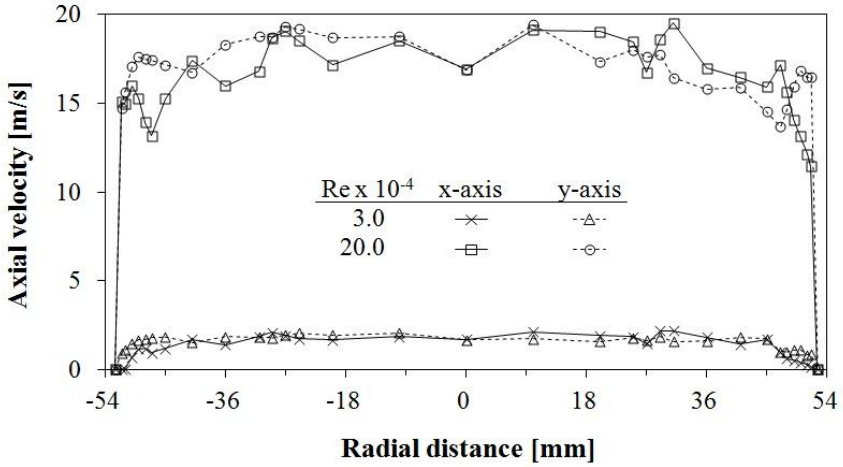

Figure 2.20: Flow distributions downstream of the perforated monolith

2.5.2 Hot-wire velocity profiles

Figure 2.21 shows the schematic layouts of three different assemblies where the velocity profiles at the rear of the monolith were obtained from HWA measurements. Photographs of the configurations are shown in Figure 2.22. The assemblies were directly coupled to the nozzle exit so that the flow entering the monoliths is uniform thus providing well defined inlet boundary conditions for CFD analysis. The axially symmetric geometries also simplify the numerical modelling and require fewer measurement data to validate the models.

Assembly 1 represents a simple configuration of automotive catalysts with the geometrical data as listed in Table 2.3. A wide angled diffuser was placed upstream of the ceramic and perforated monoliths and the flow distribution within the monolith was obtained from the HWA measurements at its exit. The measurement plane was located 40 mm downstream of the monolith to prevent the jet effect from neighbouring channels.

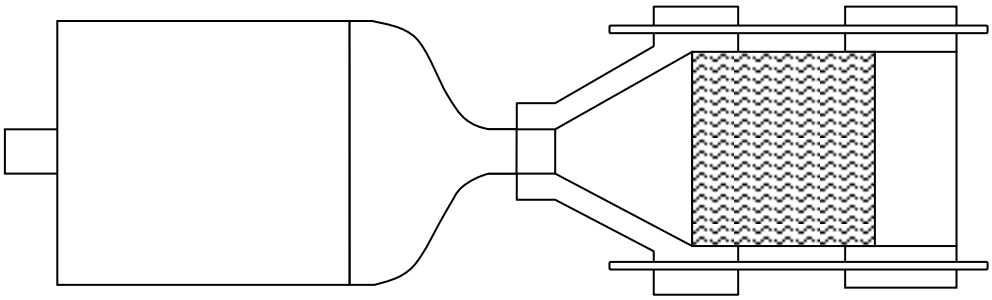

(a) Assembly 1

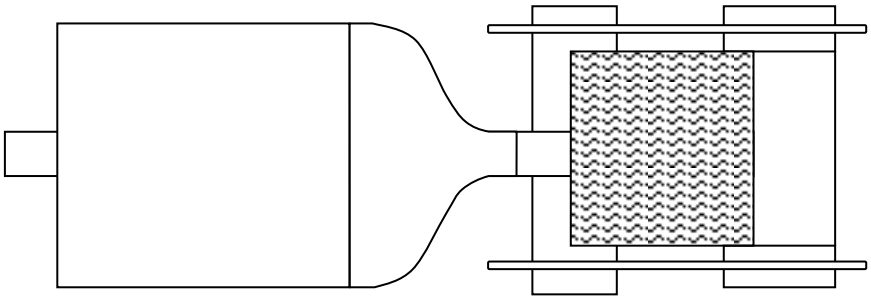

(b) Assembly 2

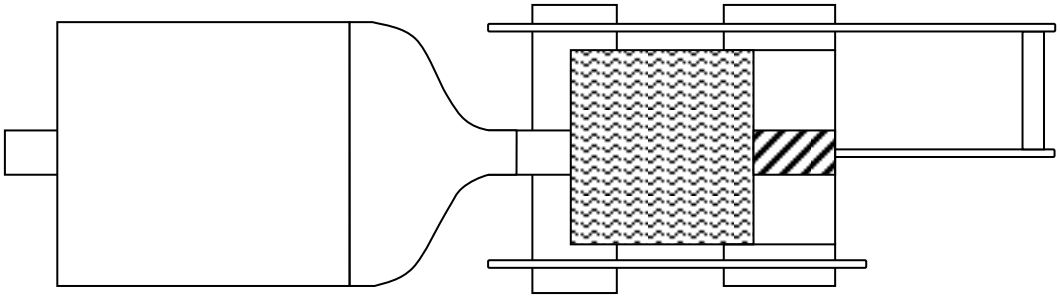

(c) Assembly 3

Figure 2.21: Layout for geometrically different flow assemblies (Schematic)

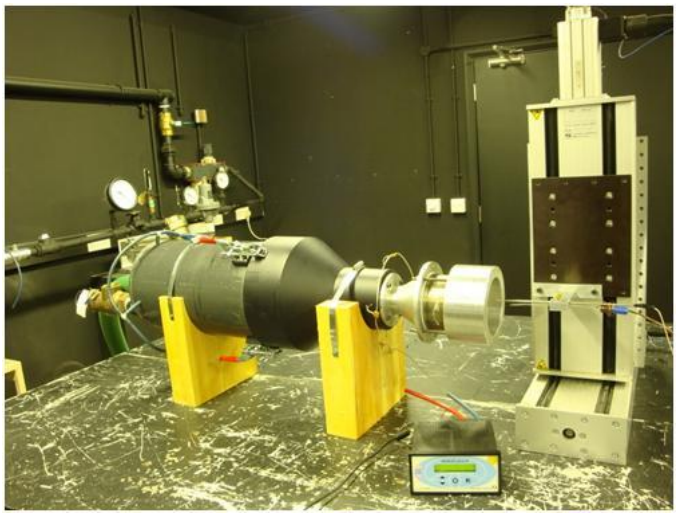

(a) Assembly 1

(b) Assembly 2

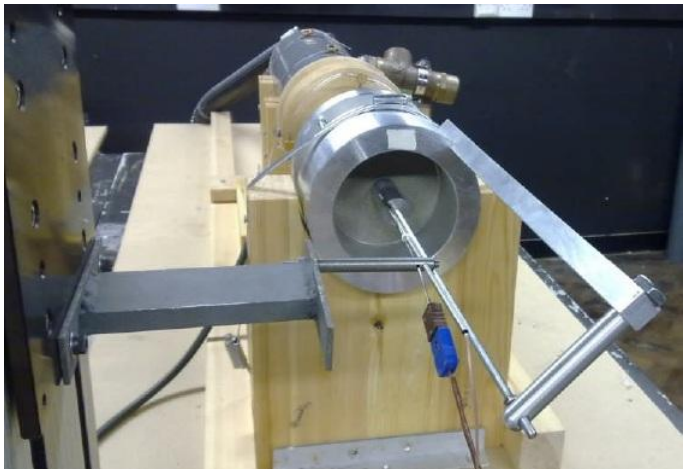

(c) Assembly 3

Figure 2.22: Photographs for geometrically different flow assemblies

Table 2.3: Geometrical data for Assembly 1

	Ceramic 400 cpsi	Perforated 600 cpsi
a. Inlet pipe		
Diameter (mm)	55	48
Length (mm)	55	48
b. Diffuser		
Included angle (deg)	60	60
Length (mm)	53	52
c. Monolith		
Diameter (mm)	116	105
Length (mm)	75	70
d. Outlet sleeve		
Length (mm)	40	40
	2.11	2.19

In Figure 2.21, Assemblies 2 and 3 were devised to force the flow to diffuse laterally within the perforated monolith. For Assembly 2, the non-uniform inlet flow condition was achieved by placing the monolith in direct contact at the nozzle exit to a small section of the front face of the brick whilst the rear of the brick was fully open. While for Assembly 3 the set up at the front face of the monolith was kept the same, but the rear of the monolith was partly covered by a rod with diameter of the same as the nozzle exit such that the velocity profiles measured downstream of the monolith is affected by the radial flow within the radially open structure. For both assemblies, the exposed front face of the monolith was sealed by a rubber gasket and a metal sleeve was placed at the outlet of the monolith. A nozzle with the outlet diameter of 24 mm was used for these tests.

2.6 Uncertainty analysis

2.6.1 Hot-Wire Anemometry (HWA)

According to Finn (2005), calibrator, transfer function, voltage resolution and atmospheric conditions are the primary sources of the velocity measurement uncertainty. The IFA 300 and the other commercial anemometers have low drift, low noise and good repeatability so these factors were relatively small in comparison with other error sources and were neglected.

Calibrator uncertainty

Air Velocity Calibrator Model 1129 was used to establish a relation between the bridge voltage and the velocity reference. Using Benoulli's equation, the flow velocity was determined from the differential pressure measured by the MKS Baratron Type 220D Pressure Transducer with the relative standard uncertainty of ± 0.15%. In addition, the equation takes into account the atmospheric pressure and the ambient temperature for the purpose of density correction.

Transfer function

During the calibration process, the probe was exposed to a set of known velocities and the voltages were recorded. Their relation was established by a fourth-order polynomial curve fit and represents the transfer function for data conversion from voltages into velocities. The uncertainty due to the calibration curve fitting is stochastic with a normal distribution and the relative standard uncertainty is estimated at ± 0.5%.

Voltage resolution

The bridge voltage was acquired via an A/D converter board, which was 12-bit over a range of ±5 V. The resolution of the voltage was equal to ½ of the smallest bit value, i.e:

$$\text{Voltage resolution} = \pm\frac{1}{2}\left(\frac{10V}{2^{12}bits}\right) = \pm\ 0.001\text{V}$$

Since it resulted in a small velocity resolution (≈ 0.1%) this uncertainty was considered negligible.

Atmospheric condition

The variation in temperature and pressure from the time of the calibration to the time of the measurements may lead to velocity uncertainty. However it was negligible as the density correction was carried out during measurements

The overall uncertainty in the HWA measurements resulted mainly from the uncertainty in the calibrator, transfer function, voltage resolution, and the atmospheric variation. Combining these sources resulted in an overall uncertainty of ±1%.

2.6.2 Particle Image Velocimetry (PIV)

The main sources of uncertainty for the two-dimensional flow measurement were calibration uncertainty and image interval and image displacement.

Calibration uncertainty

The calibration uncertainty can be attributed to the calibration board alignment and the normal view angle to the illumination plane. When all the white dots on the calibration target were illuminated, the former was found negligible (≈ 0.05 %) considering 50 mm reference length and 1 mm thickness of laser light sheet. The latter was estimated by the standard deviation of the least distances between the dots on the calibration target. It gave a standard deviation of ± 0.2 pixels or an uncertainty of ± 0.4 pixels with a 95 % level confidence as a normal distribution of the crosses was assumed. The uncertainty in the displacement was approximately 1.75 %, for the final spot size of 32 x 32 pixels.

Image interval

The uncertainty in image interval was determined by the timing accuracy of the laser pulses. The maximum laser pulse width and the shortest image interval used for the experiment were 5 ns and 11000 ns respectively. Since the maximum laser pulse duration is only 0.05% of the measurement interval, the laser timing fluctuations during the two consecutive exposures was negligible.

Image displacement

The particle diameter and grid engine contribute to the uncertainty in image displacement. In this study, the former was negligible as there was no pixel-locking with the particle diameters of 2 - 3 pixels. To increase the detectability of the correlation peak, the recursive Nyquist grid method was used to process the data and hence the latter was also considered negligible.

Combining all of these effects, the absolute uncertainty in the velocity was ±1.75%. The overall uncertainty in vorticity $\omega = \partial u/\partial y - \partial v/\partial x$ involves variations in velocity and spatial location. Therefore, the overall uncertainty in vorticity was 5%.

CHAPTER 3: PULSATING FLOW IN A PLANAR DIFFUSER UPSTREAM OF AUTOMOTIVE CATALYST MONOLITHS

3.1 Introduction

This chapter presents cycle-resolved two-dimensional Particle Image Velocimetry (PIV) measurements made in a wide-angled planar diffuser placed upstream of automotive catalyst monoliths presented with pulsating flow. The spatial and temporal velocity distribution at the exit of the monoliths was also recorded using hot wire anemometry (HWA). To characterize the flow distribution the ratio of pulse period to residence time within the diffuser (J factor) was used. Measurements were obtained for J~3.5 and 6.8 and for two lengths of monolith, i.e. 27 and 100 mm.

3.2 Steady flow

The results from steady flow measurements are presented first. Figure 3.1 shows velocity profiles across both planes at the centre of the nozzle exit at different Reynolds numbers, Re. Re is defined as $U_{in}d_h/\upsilon$ where U_{in} is the mean velocity at the diffuser inlet, d_h the hydraulic diameter of the nozzle (38.4 mm) and υ the kinematic viscosity. The velocity profiles are acceptably uniform and the flow fields within the diffuser would be expected to be symmetrical and two-dimensional. The spatial velocity distribution was also obtained 40 mm downstream of the 27 mm monolith as shown in Figure 3.2; at this distance jets exiting neighbouring channels mix sufficiently to provide smooth profiles (Benjamin et. al. 1996). These profiles are representative of the flow distribution within the monolith as the flow essentially remains uni-directional as it exits the channels. To investigate the degree of two-dimensional flow within the diffuser, the velocity profiles were plotted at various distances from the side walls as shown in Figure 3.3. Profiles are acceptably symmetrical as anticipated and two-dimensional which minimize the error in the PIV measurements.

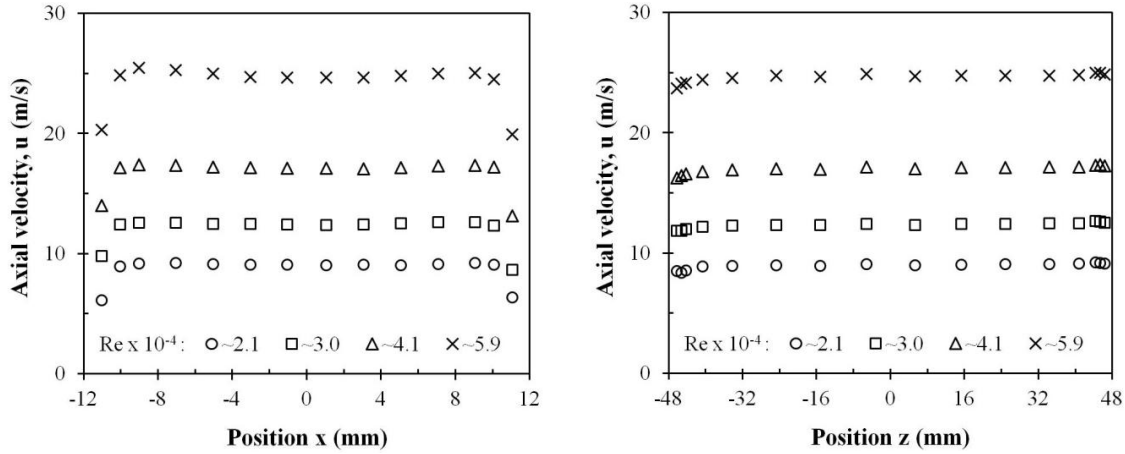

Figure 3.1: Velocity profiles across the centre of the nozzle exit measured across both planes with HWA.

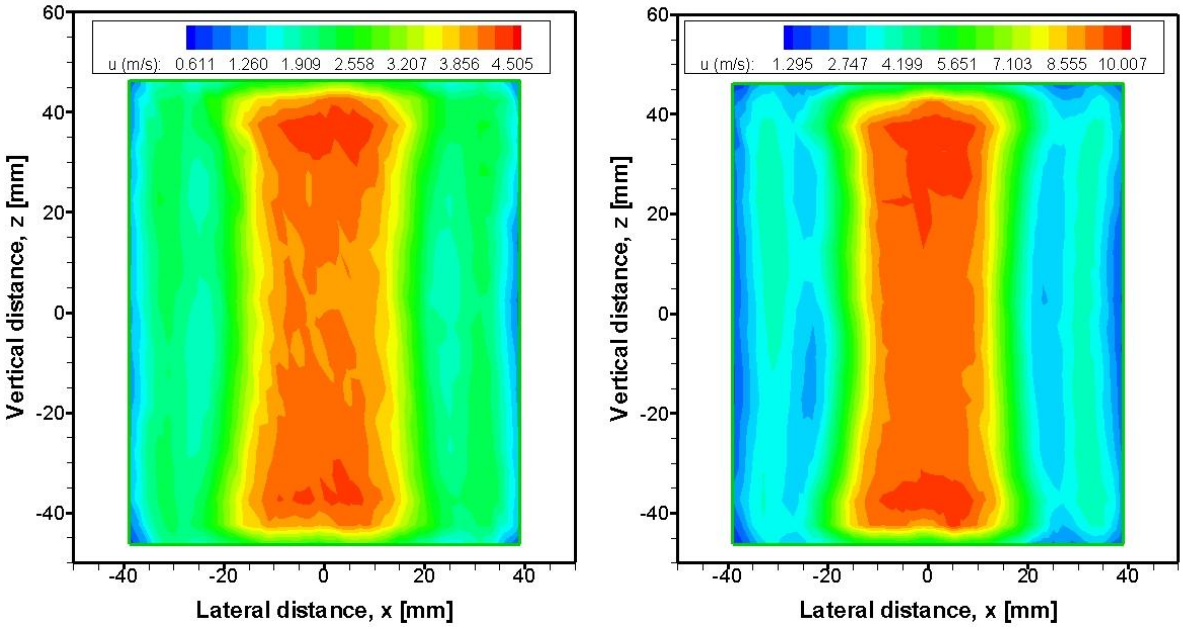

Figure 3.2: HWA velocity map on the back of 27 mm catalyst at Re = 2.2 x10^4 (Left) and 4.2x10^4 (Right)

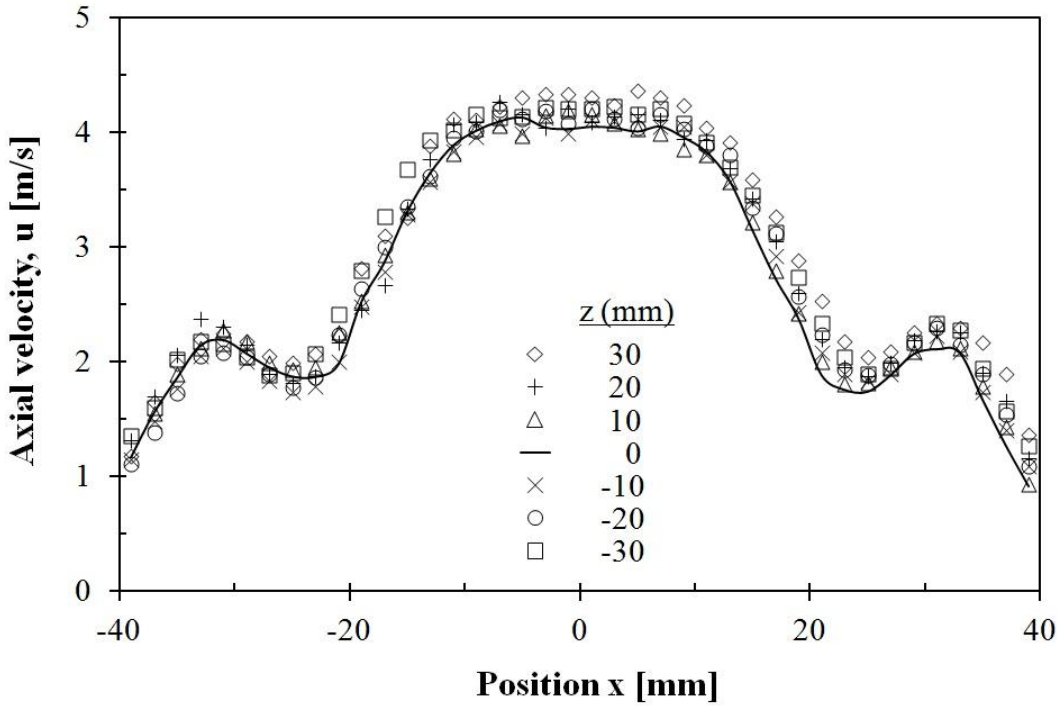

(a) Re = 2.2 x10^4

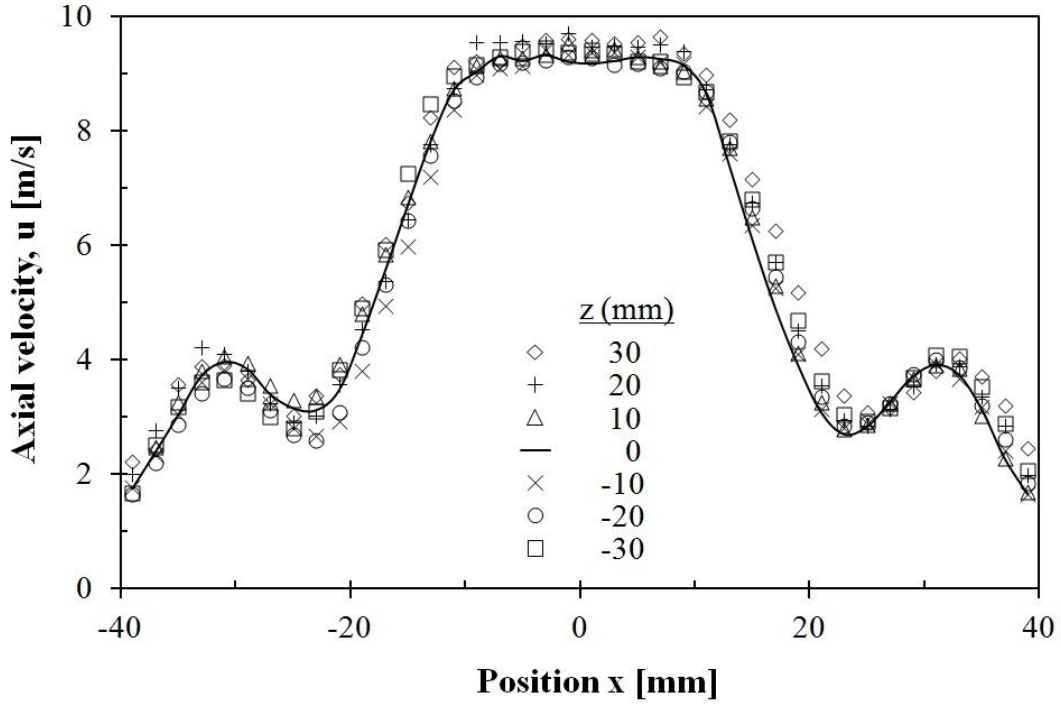

(b) Re = 4.2 x10^4

Figure 3.3: HWA velocity profiles at exit from 27 mm monolith for different vertical position z; Re = (a) 2.2 x10^4 and (b) 4.2x10^4

Figure 3.4 shows normalized velocity and vorticity maps as the average of 100 consecutive fields for Re = 4.4×10^4 and monolith length 27 mm. The flow field is essentially symmetric. Some data loss occurred at the sealed joints at the inlet and outlet of the diffuser, in the latter case up to a distance of 2.5 mm from the front face of the monolith. However, the bulk of the flow field in the diffuser is captured. Flow separation at the inlet results in a planar jet that traverses the diffuser. On approaching the monolith it spreads rapidly, part entering the monolith channels, part reversing to feed the two large recirculating vortices. This vortex-pair confines and narrows the jet resulting in non-dimensional velocities greater than 1 near the diffuser inlet. Vorticity generated within the shear layer between the jet and the surrounding fluid is convected downstream and diffused within the two large recirculating vortices. The central region of the jet has low vorticity corresponding to its potential core.

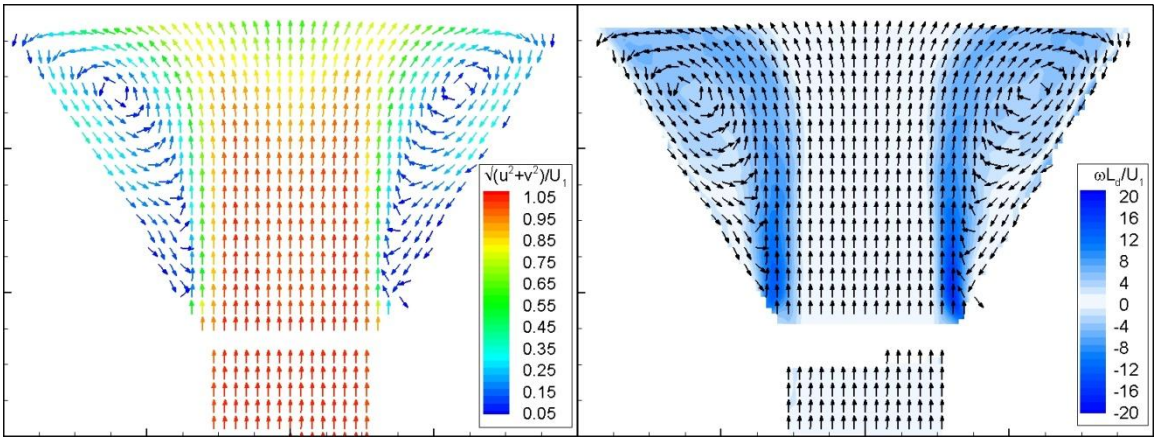

Figure 3.4: Steady flow normalised vector and vorticity fields. Re = 4.3×10^4, monolith length L = 27 mm, u axial and v transverse velocities, U_1 inlet mean velocity, ω vorticity and L_d length of diffuser

Figure 3.5 shows contours of normalized velocity for two Re and both monoliths. The shear layers at the sides of the jet are clearly shown as are the saddle-shape profiles in its potential core; similar features have been observed by Quadri et al. (2009a). With lower Re and greater downstream resistance (longer monolith) the flow profiles near the front face of the monolith are flattened. Flow distribution within the monoliths obtained from HWA are superimposed with PIV velocity profiles across the diffuser at a distance of 2.5 mm from the front face of the monoliths as shown in Figure 3.6. This again illustrates profile flattening with the lower Re and longer monolith. Similar results have been reported for axisymmetric systems (Benjamin et al 1996).

Of particular note is the significant difference in profile shape between the PIV and HWA. The flow distribution changes radically between 2.5 mm and the front face of the monolith. This flow restructuring is complex and is determined by the losses associated with the flow entering the channels plus viscous losses within the channels themselves. At the jet centre-line, where velocities are greatest, the latter dominate and a radial pressure gradient is formed across the front face of the monolith thus spreading the jet. Consequently, away from the centre-line, fluid approaches the channels obliquely at an angle of incidence which increases with radial distance. Oblique entry losses are very significant at high incidence and can exceed viscous losses ((Quadri et al (2009b), Persoons et al (2008)) thus forcing more flow towards the walls. As it approaches the wall it decelerates and the local pressure increases, which encourages flow through the outer channels. The net result is the formation of the secondary velocity peaks within the monolith about 10 mm from the wall.

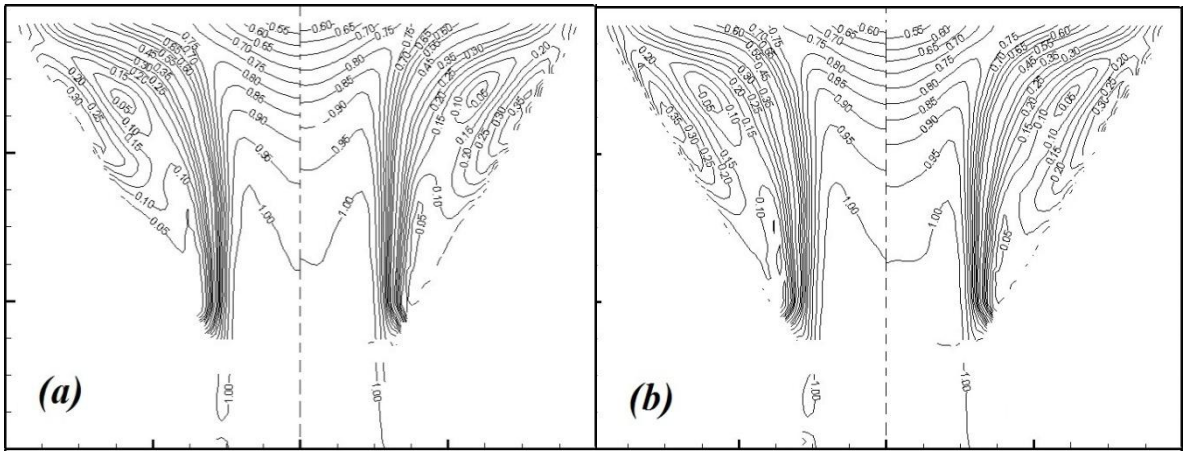

Figure 3.5: Contours of normalised velocities with steady flow (a) Re = 2.3 x 10^4 (left), Re = 6.2 x 10^4 (right), L = 27 mm (b) Re = 6.2 x 10^4, L = 27 mm (left), 100 mm (right)

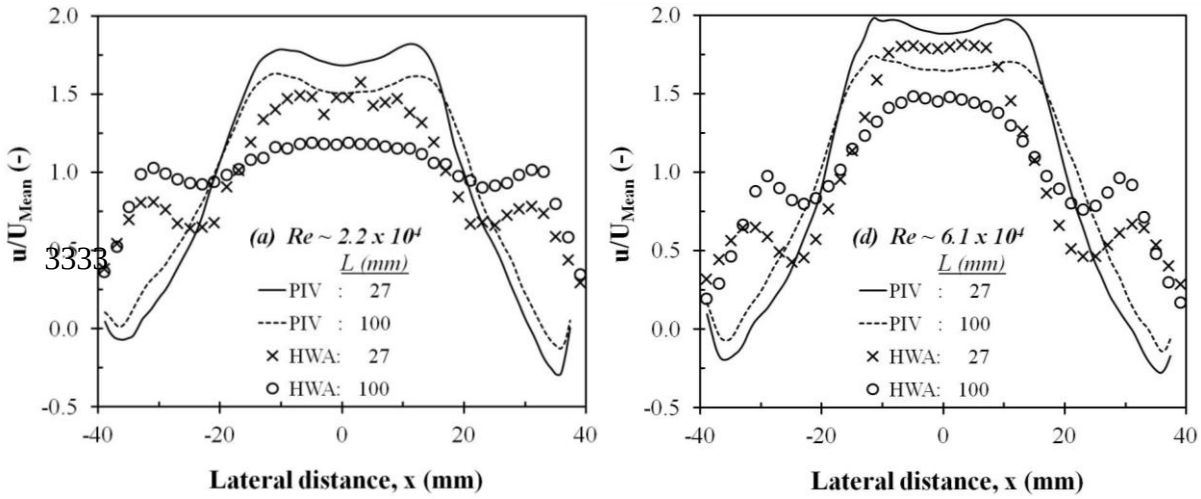

3333

Figure 3.6: Steady flow. Normalised axial velocity distributions 2.5 mm upstream (PIV) and 40 mm downstream (HWA); u axial velocity, U_2 mean velocity downstream of the monolith

3.3 Pulsating Flow

PIV and HWA measurements were obtained for cases shown in Table 3.1. Measurements were obtained for Re = $2.2x10^4$ and ~$4.2x10^4$ and at 50 and 100 Hz with monoliths of length L=27 and 100 mm. Flow regimes may be characterized by a parameter J defined as the ratio of pulse period to residence time in the diffuser. J is given as $U_{in}/L_d f$, where U_{in} is the mean inlet velocity, f pulse frequency and L_d, the length of the diffuser. The cases with J~ 3.5 correspond to Re = $2.2x10^4$, f = 50 Hz and Re ~ $4.2x10^4$, f = 100 Hz. The cases for J=6.8 correspond to Re ~ $4.2x10^4$, f = 50 Hz. In a previous study for an axisymmetric assembly the flow maldistribution within the monolith was found to be correlated with J (Benjamin et al 2002). Steady flow may be considered as the limiting case as J approaches infinity, i.e. pulse period becomes infinitely long.

Figure 3.7 shows pulse shapes measured by HWA at the centre of the inlet duct. Whilst some variation exists between the two frequencies they exhibit similar peak/mean ratios and are largely independent of Re and monolith length. An example of velocity profiles at the inlet to the diffuser is shown in Figure 3.8. The profiles were obtained as phase-averages at various non-dimensional times (t/T) throughout the cycle. Profiles are flat as for the steady flow cases.

Table 3.1: Test cases

PIV measurements						
Case	1	2	3	4	5	6
L [mm]	27	100	27	100	27	100
f [Hz]	50	50	50	50	100	100
Re x 10^{-4}	2.24	2.25	4.19	4.19	4.16	4.21
J [-]	3.6	3.6	6.8	6.8	3.4	3.4
HWA measurements						
Re x 10^{-4}	2.18	2.19	4.10	4.12	4.09	4.12
J [-]	3.5	3.6	6.8	6.8	3.4	3.4

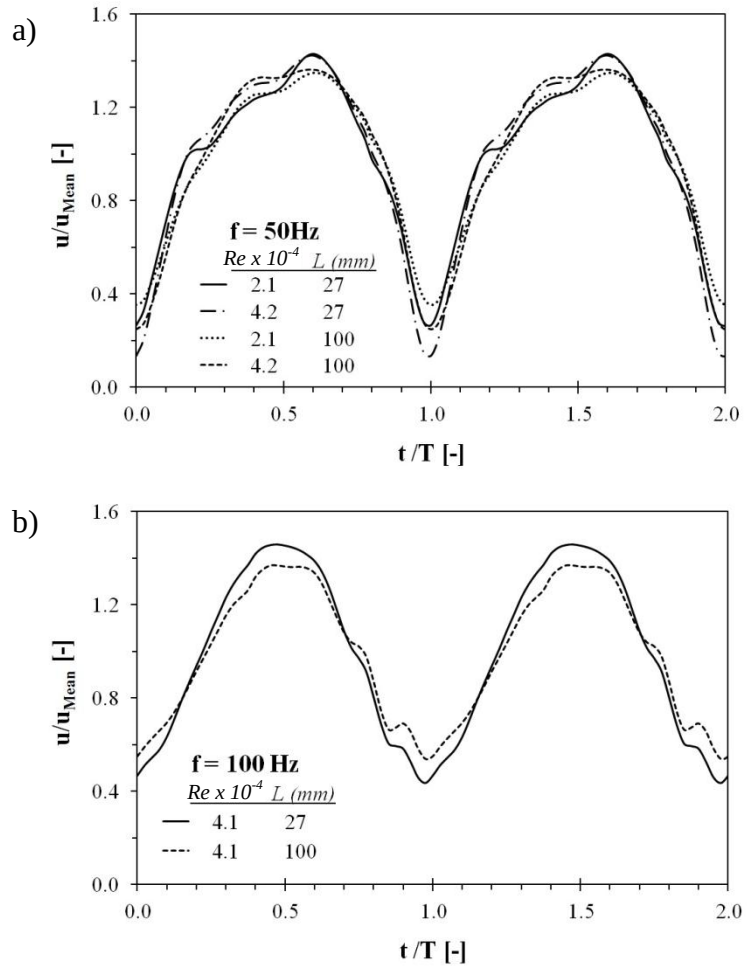

Figure 3.7: Inlet pulse shapes observed at centre of the nozzle exit for (a) 50 Hz and (b) 100 Hz, t is the time, T pulse period, u phase-averaged velocity, u_{Mean} cycle-averaged velocity

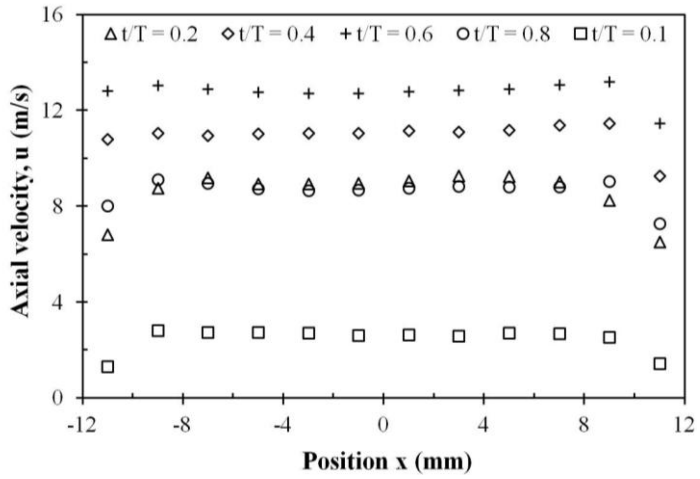

Figure 3.8: Phase-averaged velocity profiles across centre of the nozzle exit (f = 50 Hz, Re = 2.1 x 104, L = 27 mm)

3.3.1 Flow field for J = 6.8 (Case 3).

Figure 3.9 shows the normalised velocity and vorticity fields for J=6.8 with the 27 mm monolith. The corresponding fields for 100 mm were similar in many respects as included in Appendix F and so are not reported here. Figure 3.7 shows deceleration occurs from t/T=0.6 to 1.0. At the time of maximum inlet velocity, t/T=0.6, the flow field is similar to that for steady flow. The inlet inertia at this time is sufficient to cause separation near the inlet. The resulting jet traverses the diffuser, rapidly spreading near the front of the monolith and either entering the channels or recirculating within the diffuser. High vorticity is generated in the shear layer at the edges of the jet which is subsequently mixed within the separation bubble. The central region of the jet has low vorticity corresponding to its potential core. As the flow decelerates the vortex pair is able to "squeeze" the jet core; this is especially noticeable near the inlet at t/T=1.0. During deceleration vorticity generation at the inlet is reduced and is also dissipating within the dominant vortex structures. At t/T=0.8, the inlet velocity is approximately equal to the cycle-averaged value. Hence the flow field can be compared with that for steady flow as shown in Figure 3.10 where velocity contour maps are illustrated for 27 and 100 mm monoliths. The contours are similar in many respects. The larger resistance of the 100 mm monolith reduces the velocity in the central region and causes greater spreading of the jet for both steady and pulsating flow. The recirculating vortices for pulsating flow are evidently too transient in nature to produce the saddle shapes featured with steady flow within the main body of the diffuser.

The flow accelerates from t/T =0.1 to 0.5. Figure 3.9 shows the recirculation regions from the previous cycle still residing in the diffuser at t/T=0.1. From t/T=0.1- 0.2, the low inlet inertia allows the flow to stay attached for some distance along the wall. As the flow expands it transports the residual vortex structures from the previous cycle through the diffuser. At t/T=0.2, the inlet velocity is again approximately equal to the cycle-averaged value but the flow field is quite different from that at t/T=0.8. From t/T=0.3-0.5, as inlet inertia increases, the flow detaches forming separation bubbles illustrated by the growing region of vorticity. The flow is able to reattach behind the bubbles resulting in relatively uniform flow at the monolith as the residual vortex has now been pushed out of the diffuser. The net effect is that the

time-averaged flow distribution at the front face of the monolith is improved compared with that for steady flow. From t/T=0.5 the flow again begins to resemble that for steady flow as the accelerating inlet jet approaches the monolith.

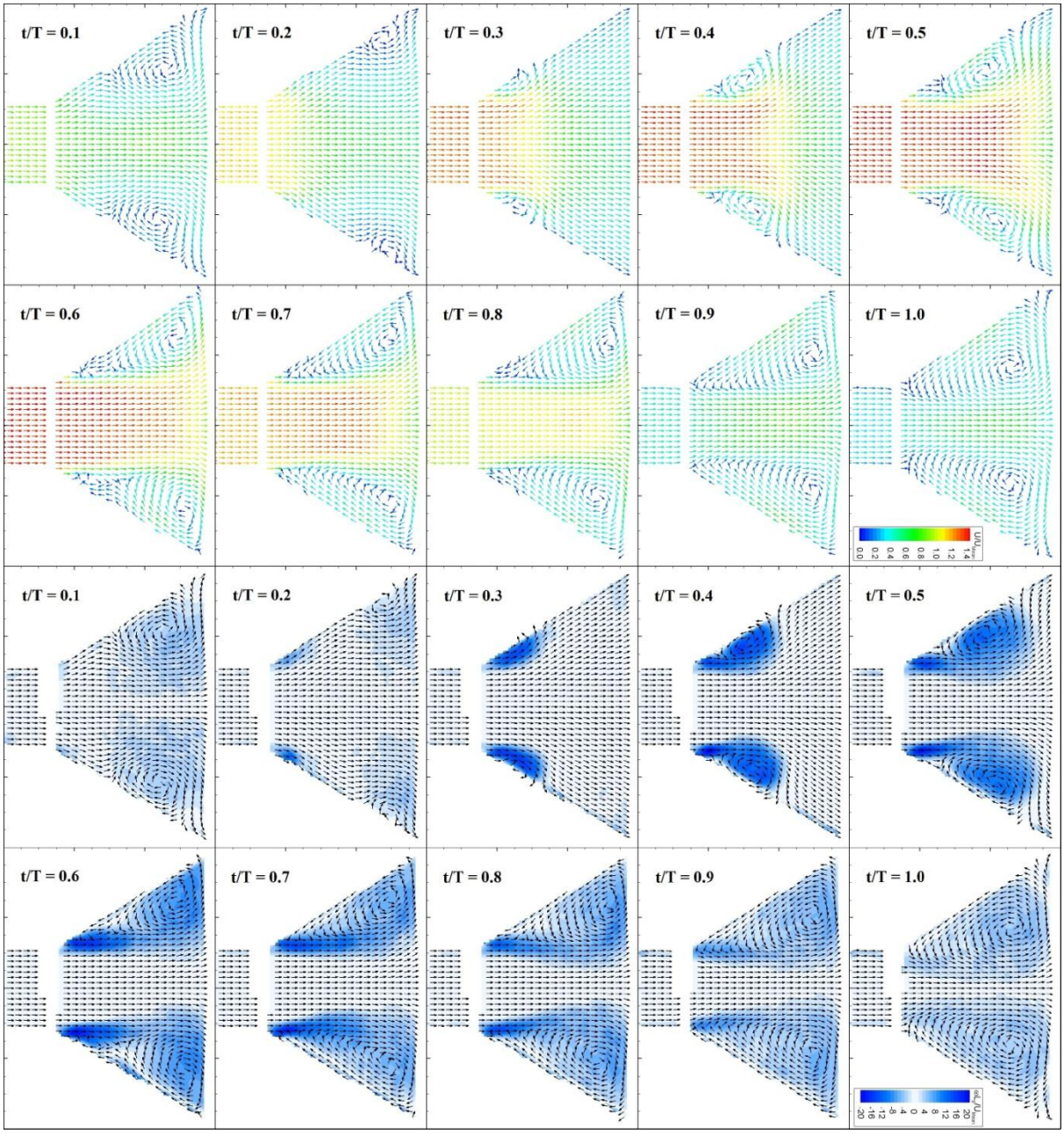

Figure 3.9: Normalised phase-averaged velocity vector and vorticity fields for Case 3 at J = 6.8 (Re = 4.2x104, f =50 Hz, L = 27mm). Fields are normalised by the cycle-averaged mean inlet velocity

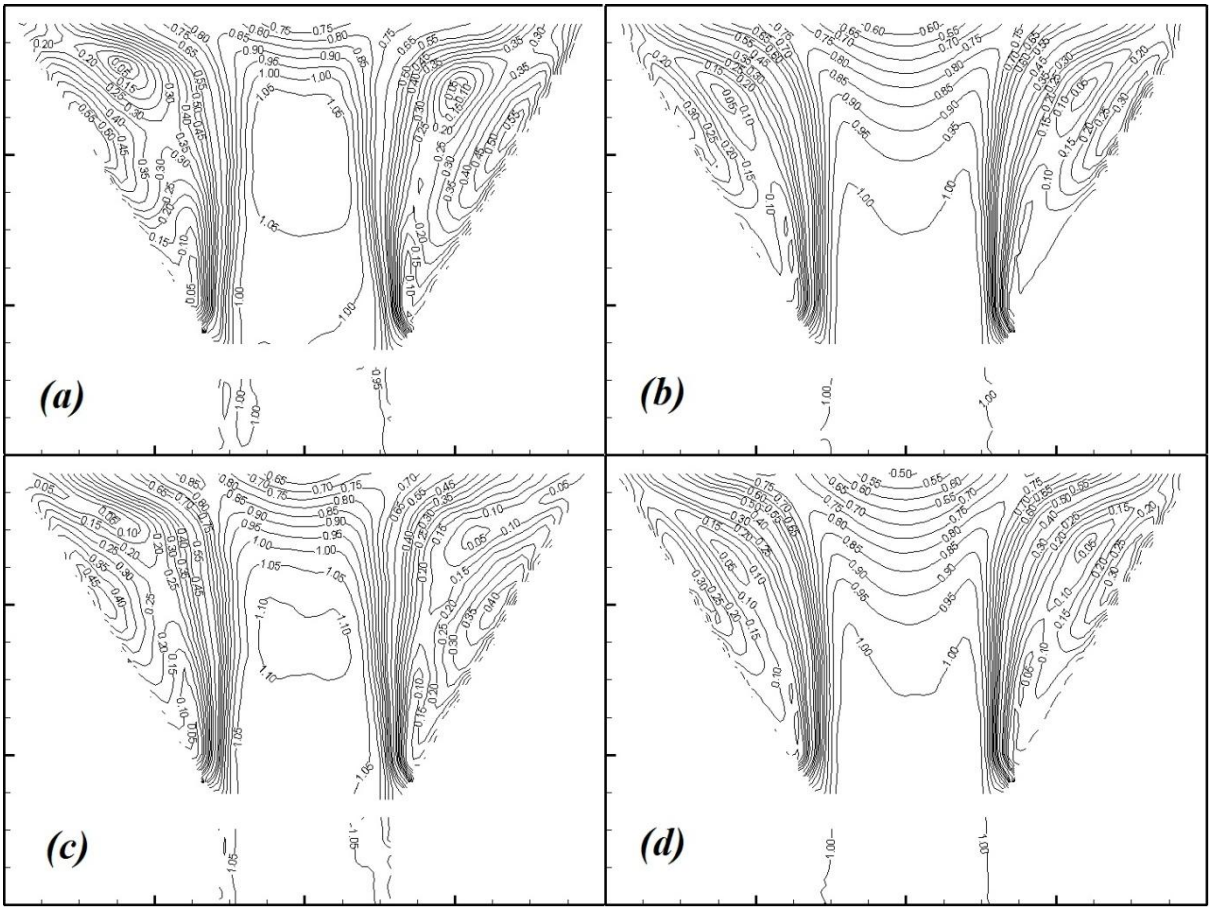

Figure 3.10: Normalised velocity contours at Re ~ 4.2 x 104 (a) t/T = 0.8, Case (3), f = 50 Hz, L = 27 mm (b) Steady flow, L = 27 mm (c) t/T = 0.8, Case (4), f = 50 Hz, L = 100 mm (d) Steady flow, L = 100 mm. In (a) and (c) phase-averaged velocities are normalised by the cycle-averaged mean inlet velocity

3.2.2 Flow field comparison at 50 Hz with varying J (Cases 1 and 3).

Figure 3.11 compares side-by-side the normalised velocity vector and vorticity fields at 50Hz for Re= $2.2x10^4$ and $4.2x10^4$, corresponding to J=3.6 and 6.8 respectively. The flow field for J=3.6 exhibits features similar to those discussed earlier for J=6.8. During acceleration, the flow initially remains attached pushing the residual vortex from the previous cycle out of the diffuser. Separation occurs at t/T=0.4 and the inlet jet and its associated vortex structure begin to develop within the diffuser. During deceleration the recirculating zone increases in size effectively squeezing the jet as it loses momentum (t/T=0.8). However significant differences are observed at the lower Re. The reduced inlet inertia during acceleration is less effective at removing the residual vortices; at t/T =0.3, for example, they have already been eliminated at the higher Re. Flow separation occurs later and so there is a reduction in size of the separation bubbles at equivalent times. As a consequence, during deceleration (t/T=0.6, 0.7), the flow is able to reattach downstream of the bubbles resulting in a flatter distribution at the monolith at the lower J value.

3.2.3 Flow field comparison at Re 4.2 $x10^4$ with varying J (Cases 3 and 5).

Figure 3.12 compares side-by-side normalised velocity vector and vorticity fields at 100Hz and 50 Hz for Re = $4.2x10^4$, corresponding to J= 3.4 and 6.8 respectively. Flow development at the higher frequency is very similar to that observed for similar J in Figure 3.11 i.e. longer retention of residual vorticity from the previous cycle, later separation during acceleration and smaller recirculation bubbles. It would appear that at the higher frequency the flow does not have sufficient time to establish the inertia dominated flow regimes associated with lower frequencies and/or higher Re.

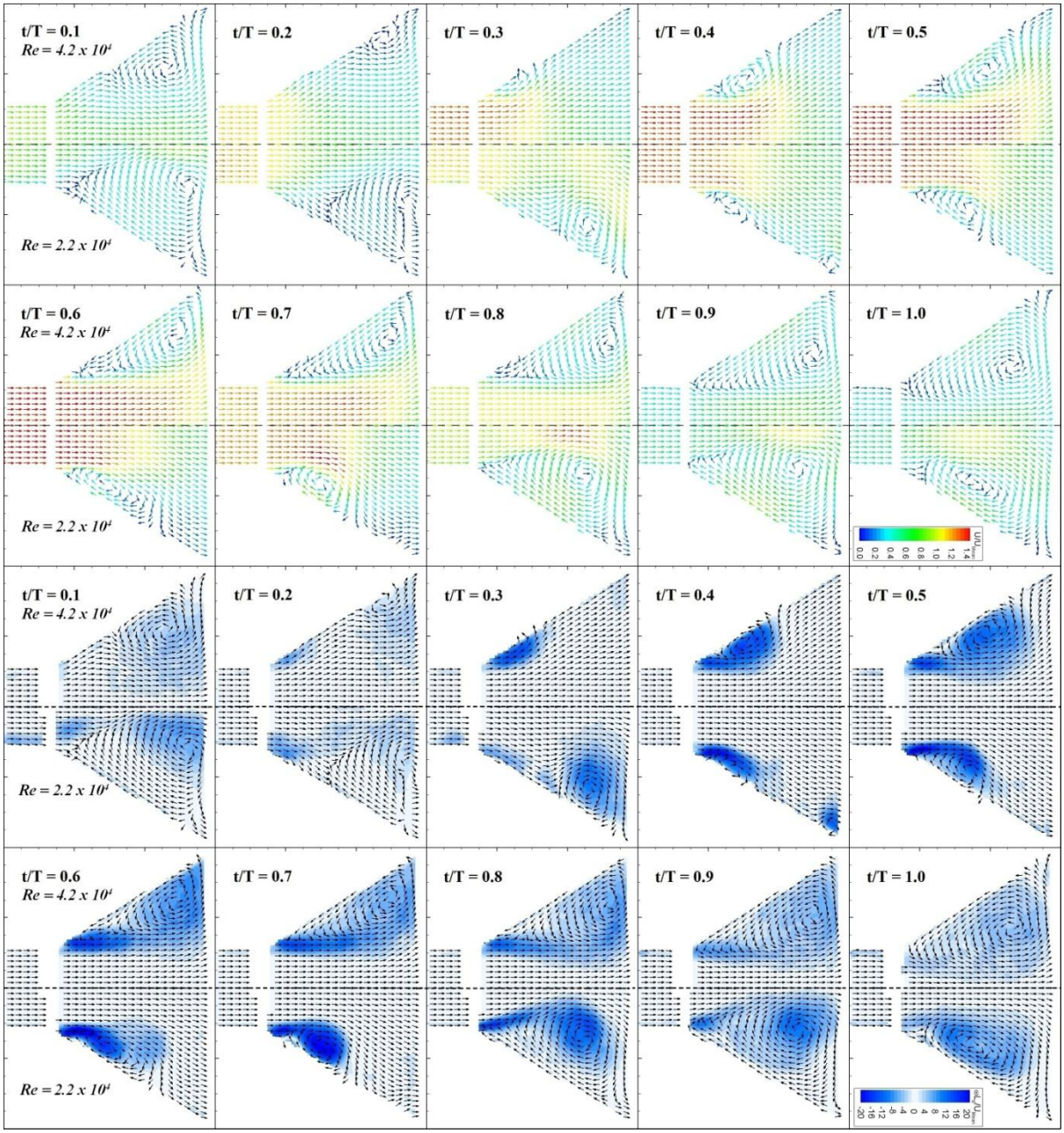

Figure 3.11: Normalised phased averaged velocity and vorticity fields for Case 1 (J = 3.6, Re = 2.2 x 10^4, 50 Hz) and Case 3 (J = 6.8, Re = 4.2 x 10^4, 50 Hz) for L = 27 mm. Fields are normalised by the cycle-averaged mean inlet velocity

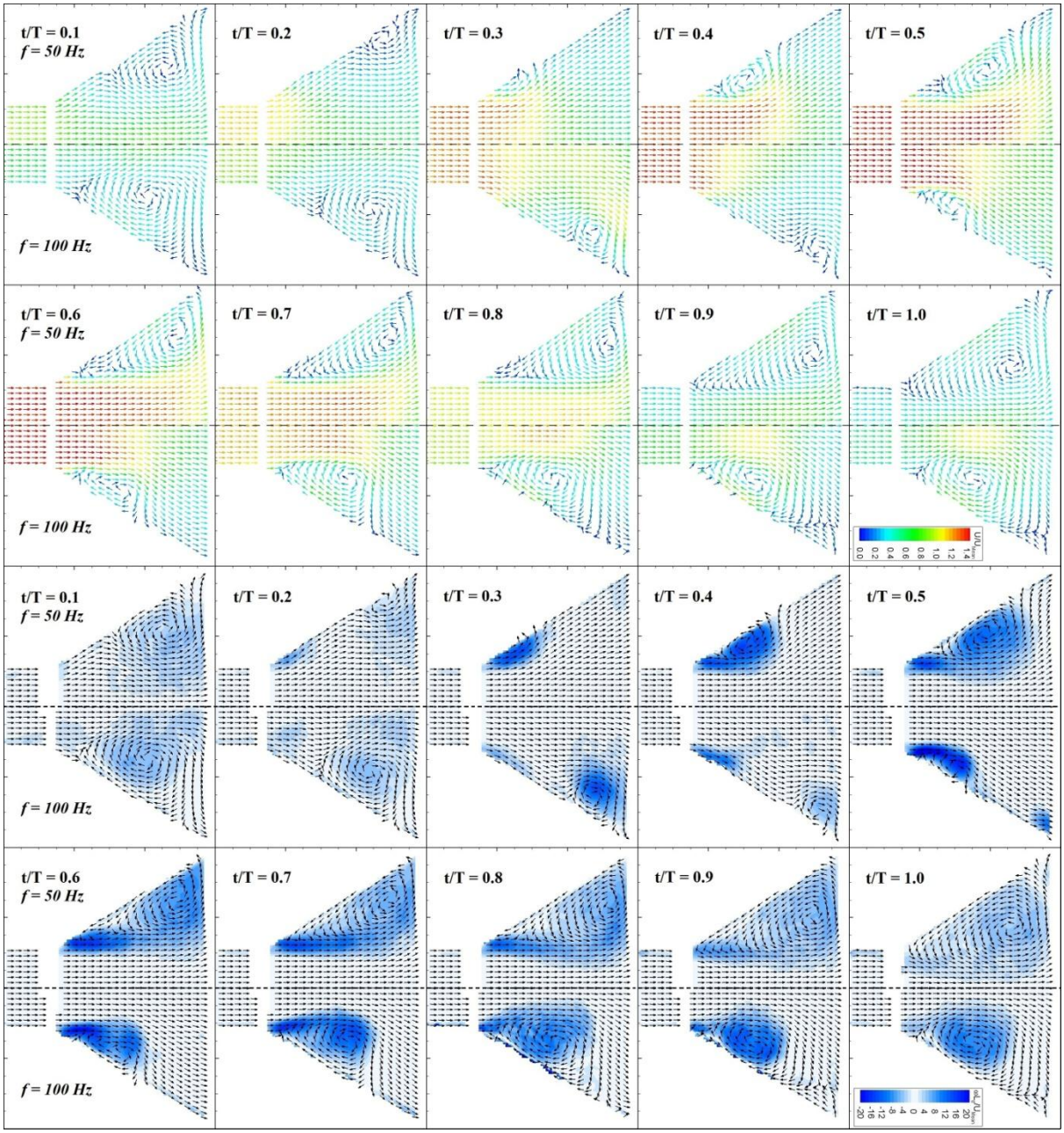

Figure 3.12: Normalised phase-averaged velocity and vorticity fields for Case 3 (J = 6.8, Re = 4.2 x 10^4, 50 Hz) and Case 5 (J = 3.4, Re = 4.2 x 10^4, 100 Hz) for L = 27 mm. Fields are normalised by the cycle-averaged mean inlet velocity

3.4 Flow maldistribution in the monolith

Figure 3.13 compares the cycle-averaged pulsating flow distributions downstream of the 27 and 100 mm monoliths with those for steady flow. Such a comparison is useful for assessing the adequacy of deducing flow maldistribution in engine flows based on a steady flow analysis. For the given monolith profiles for J ~ 3.5 are very similar whereas the flow maldistribution is greater with J=6.8; findings which are consistent with the flow fields obtained upstream in the diffuser. For a given Re the flow maldistribution is highest with steady flow (J infinite), the differences being more pronounced for the shorter monolith. For the longer monolith the distributions are flatter for all cases as a consequence of the greater downstream resistance. Hence with higher resistance the effect of pulsations will have a reduced impact on the mean flow maldistribution.

In section 3.2, flow restructuring at the front face of the monolith was discussed for the case of steady flow. It is anticipated that similar restructuring will occur for the case of pulsating flow. This is clear from Figure 3.14 which compares the PIV cycle-averaged velocity profiles just upstream of both monoliths to those observed downstream for J=6.8. As for the case of steady flow it is clear that considerable flow restructuring occurs within 2.5 mm of the front face of the monolith.

The effect of pulsations on the flow distribution across automotive catalysts can therefore be significant. Clearly much will depend on engine type and exhaust after-treatment geometry. For situations with high flow, low engine speed and after-treatment systems with short monoliths (e.g. close-coupled systems) flow maldistribution will be increased.

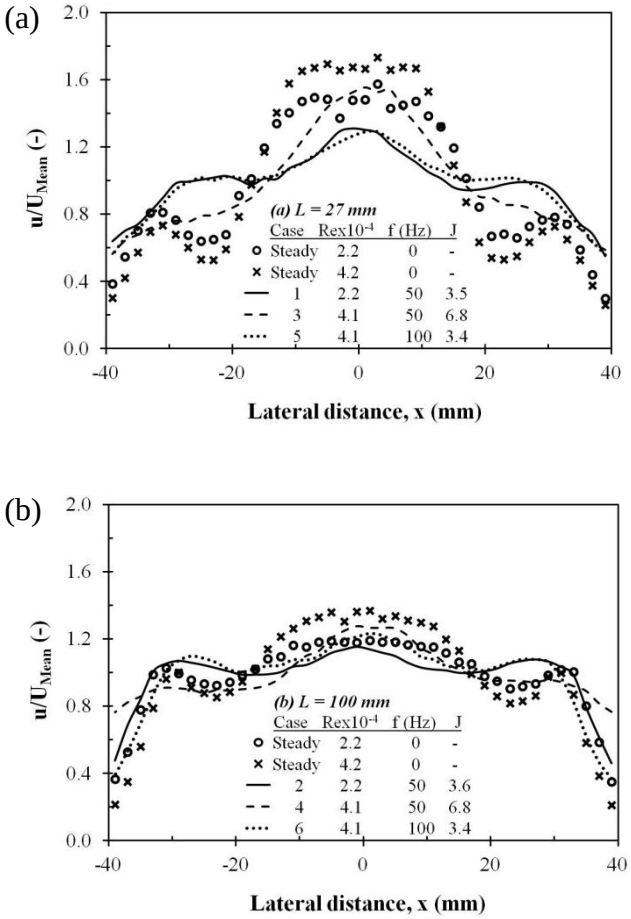

Figure 3.13: Steady flow and cycle-averaged velocity profiles at the monolith exit, L[mm] = (a) 27, (b) 100. Velocities are normalised by the cycle-averaged mean velocity downstream of the monolith

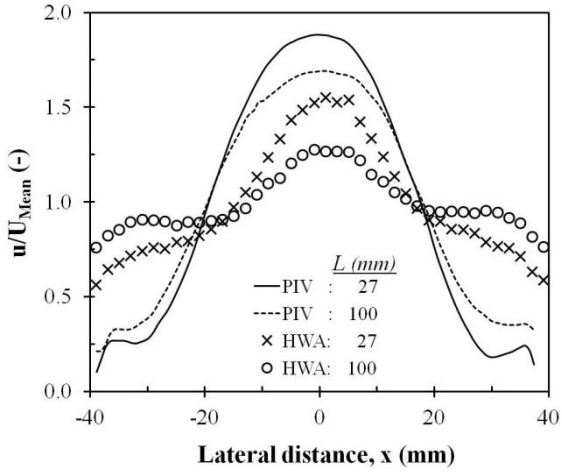

Figure 3.14: Cycle-averaged velocity profiles measured 2.5 mm upstream (PIV) and 40 mm downstream (HWA) for Re ~ 4.2 x 104, f = 50 Hz, J = 6.8 for L = 27 mm and 100 mm (Cases 3 and 4). Velocities are normalised by the cycle-averaged mean velocity downstream of the monolith

3.5 Summary

PIV studies have been performed in a planar wide-angled diffuser placed upstream of automotive exhaust monoliths. Studies were undertaken at frequencies of 50 and 100 Hz for Re = $2.2x10^4$ and $4.2x10^4$ and compared to steady flow measurements. The spatial and temporal velocity distribution at the exit of the monoliths was also recorded using hot wire anemometry (HWA). The ratio of pulse period to residence time within the diffuser (J factor) was used to characterise the flow. Measurements were obtained for J~3.5 and 6.8.

With steady flow, separation occurred at the inlet to the diffuser for both Re resulting in a planar jet that traversed the diffuser. On approaching the monolith it spread rapidly, part entering the monolith channels, part reversing to feed the two large recirculating vortices. Significant flow restructuring occurs in the diffuser just upstream of the monolith as the flow enters the monolith channels.

With pulsations the flow field varied throughout the cycle. Initially, as the flow accelerated, it remained attached to the diffuser walls for some distance. Separation bubbles then formed near the diffuser inlet resulting in the development, later in the cycle, of two large recirculating vortices. These vortices occupied the diffuser volume at the end of the pulse before being transported out during the subsequent cycle. Flow separation occurred earlier for J= 6.8 with larger vortex structures dominating the diffuser. The flow field at the beginning of the deceleration phase resembled that under steady flow conditions. Two cases with J~3.5 resulted in very similar flow fields. In each, the flow was able to reattach downstream of the separation bubbles during part of the cycle thus presenting more uniform flow to the monolith. Low Re and high frequency pulses (low J) do not permit the flow to establish sufficient inertia to provide the fully separated flow regimes observed under steady flow conditions and so result in flatter profiles within the monolith. Increasing J from ~3.5 to 6.8 resulted in greater flow maldistribution in the monolith; steady flow produced the highest maldistribution at the same Re. Increasing monolith resistance flattens the flow field just upstream and within the monolith for both steady and pulsating flows.

CHAPTER 4: OBLIQUE ENTRY PRESSURE LOSSES

4.1 Introduction

The previous chapter shows flow redistribution just upstream of the monolith for steady and pulsating cases as the losses associated with the flow entering the channels effectively alter the lateral pressure gradient. CFD simulations presented in Chapter 6 incorporate these losses in order to improve the prediction of flow distribution within the monolith. A methodology has been derived by Quadri et al. (2009b) to quantify the oblique entry pressure losses for flow entering the monolith channels using a one-dimensional isothermal oblique angle rig. They found that the losses increased with α and Re. In the present study, the flow rig was redesigned as described in the section 2.4 to investigate α_c and the Re effect at high mass flow rates. Measurements were performed using different lengths of monolith (17 and 27 mm) and compared with other theoretical expressions.

4.2 HWA profiles downstream of the oblique angled duct

Figure 2.16 shows the schematic of the flow rig where a cylindrical duct was placed at an angle of α upstream of the monolith where the flow approaching the channels is assumed to be spatially uniform as described in the section 2.4. The cross-sectional area downstream of the duct is an elliptical profile with no change in the minor axis as α increases. However the major axis increases with respect to α and thus the flow has to travel further along the duct on one side resulting in developing boundary layers. To investigate the viscous effect on the flow uniformity downstream of the duct for the worst case, velocity profiles along the major axis were obtained from HWA downstream of the monoliths.

Figure 4.1, Figure 4.2 and Figure 4.3 show the hot-wire profiles for 17 and 27 mm monolith lengths. Profiles were approximately uniform for $\alpha = 27^o$ and 70^o at a lower flow rate, i.e. $Re_a = 2240$ (see Figure 4.1 and Figure 4.2), a similar characteristic has been reported by Quadri et. al. (2009b). Re_a is formulated based on the mean approach velocity, U_1 across the duct and the hydraulic diameter of the monolith

channel. At higher flow rate, i.e. Re_a = 4060, the profiles were considered uniform for $\alpha = 27^o$, but were not uniform for $\alpha = 70^o$ and so there is some uncertainty with regards to the flow field upstream of the monolith. However the skewness only affects a relatively small section of the profile and so was considered acceptable for the evaluation of oblique losses.

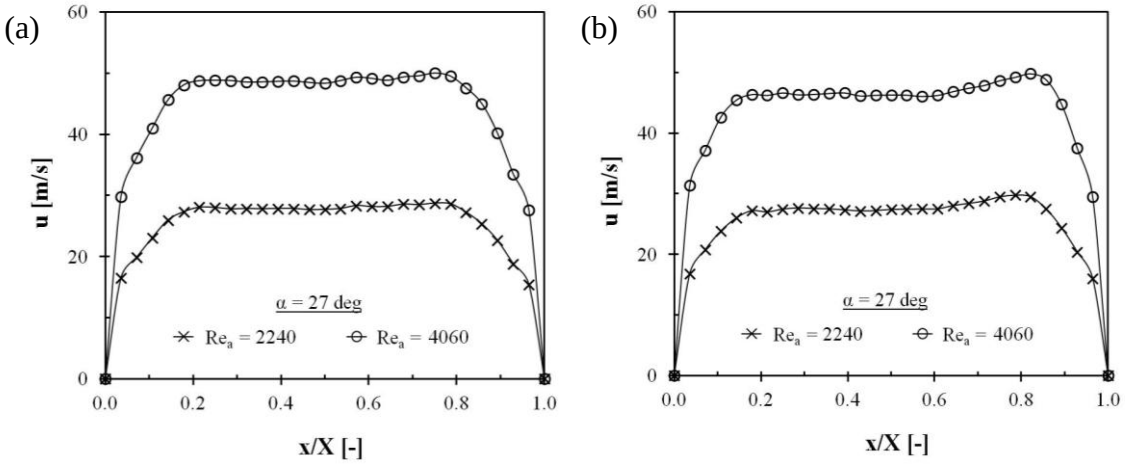

Figure 4.1: Velocity profiles at $\alpha = 27^o$ for (a) L = 17 mm and (b) L = 27 mm

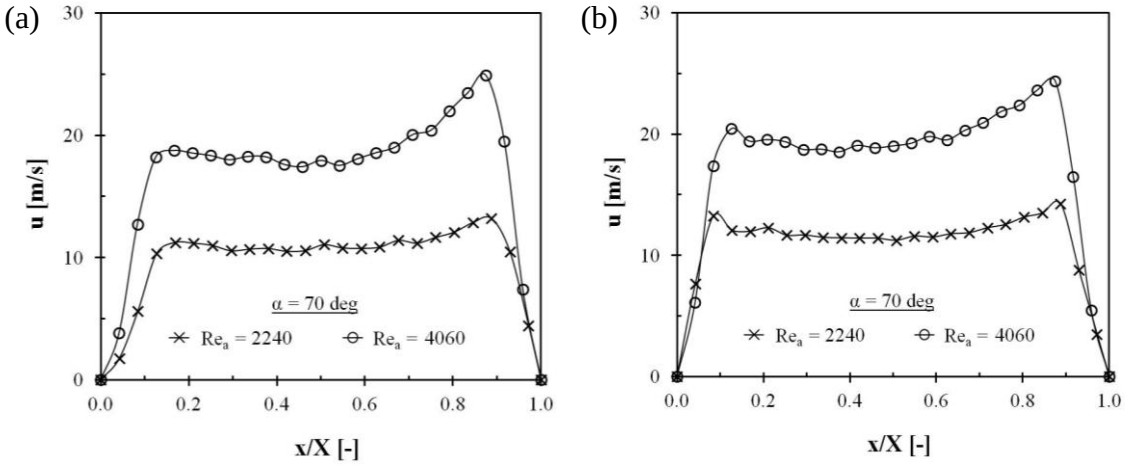

Figure 4.2: Velocity profiles at $\alpha = 70^o$ for (a) L = 17 mm and (b) L = 27 mm

Figure 4.3 shows a significant skewness in the profiles with more flow entering the monolith on one side at $\alpha = 81^o$ and 83^o. This might be due to the fact that the flow separation occurred and restricted the flow entering the monolith. Thus

measurements at $\alpha \geq 81^{o}$, although originally planned, were not possible due to the unexpected limitation of the test rig.

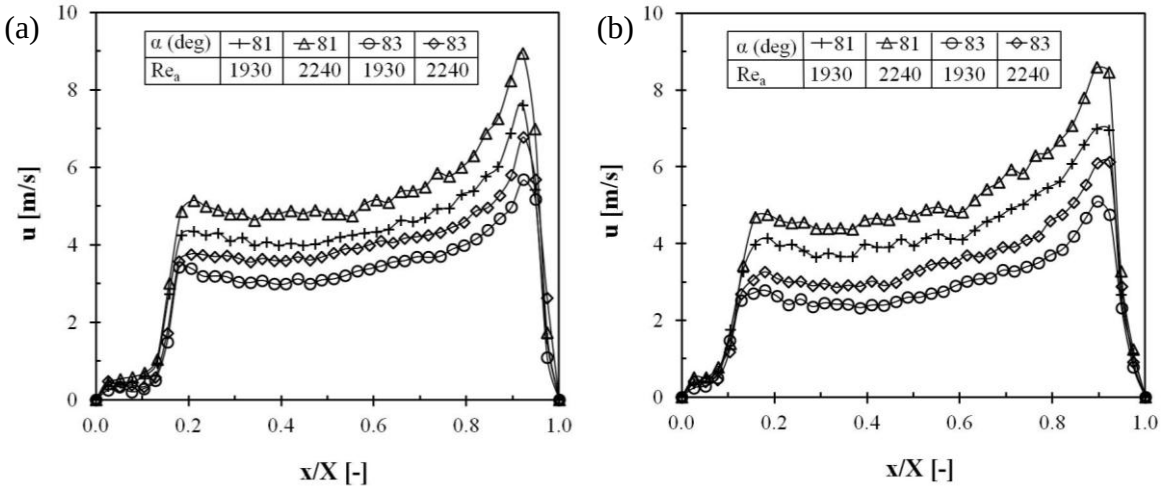

Figure 4.3: Velocity profiles at high α for (a) L = 17 mm and (b) L = 27 mm

4.3 Monolith pressure drop, P_L

The monolith pressure drop, P_L was obtained from the measurements at zero incidences for a range of Re_a to provide the basis of the calculation of K_{Obl} in equation (2.11). The results were plotted as P_L/L against the downstream velocity, U_2 where second order polynomial equations were used to fit the data as shown in Figure 4.4. The pressure-drop per unit length is given as:

$$P_L/L = P_i U_1^{\,2} + P_v U_1 \qquad (4.1)$$

The squared term on the right-hand side of the equation is attributed to turbulent flow due to the contraction and expansion losses at the entry and exit of the monolith channel as well as the developing boundary layer. The pressure drop caused by the fully developed laminar flow resulting from the viscous shear at the channel walls is described by the linear term on the right-hand side of the equation. Observation on the graph shows that the short monolith produced higher loss per unit length as the flow is still developing when it exits the monolith channels.

Single channel studies were then undertaken to compare the non-dimensional data with theoretical expressions often used when performing CFD simulations, i.e. Hagen Poiseuille (H-P) formulation and Shah's correlation which are defined by equations (1.2) and (1.3), respectively in Table 1.2. The H-P formulation assumes the flow is laminar and fully developed, i.e. the pressure drop is proportional to the fluid velocity; while Shah's formulation takes into account the developing flow in a duct.

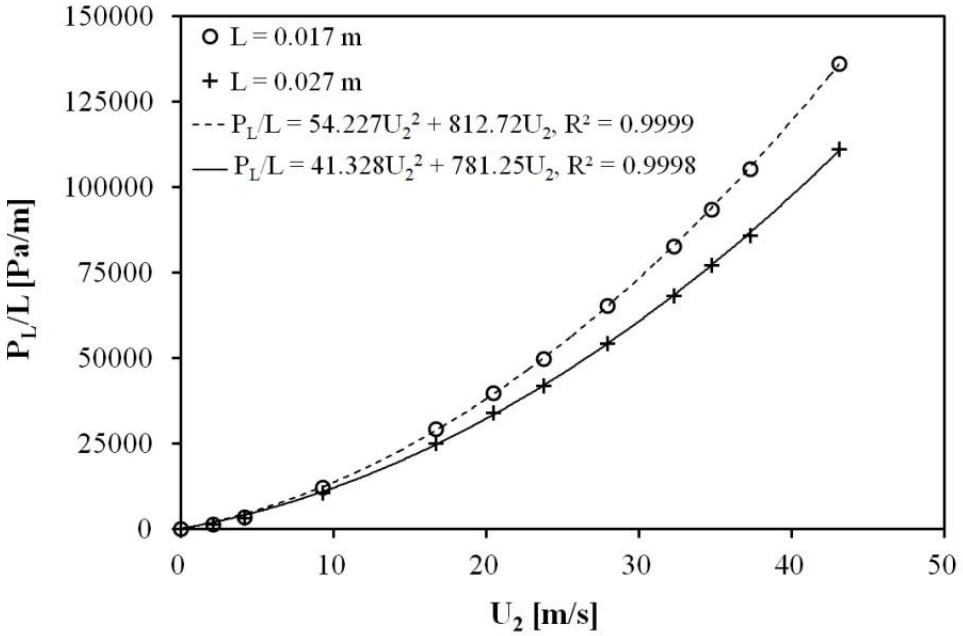

Figure 4.4: P_L for 17 and 27 mm monoliths.

Figure 4.5 shows the dependence of P_L on Re_c and X^+, the latter being defined as L/d_hRe_c. Thus X^+ values are high when the flow traverses the channels at low Re and vice versa. The H-P equation loses validity even at low velocities suggesting the flow is still developing when it exits the channels. The additional pressure drop caused by the developing boundary layer is included in Shah's correlation and thus the prediction corresponds well with the data for $X^+ > 0.02$ as suggested by Benjamin et. al. (1996). At small values of X^+ predictions using Shah's correlation are poorer as the flow may not remain laminar at the higher flow rates, i.e. $Re_c > 1500$.

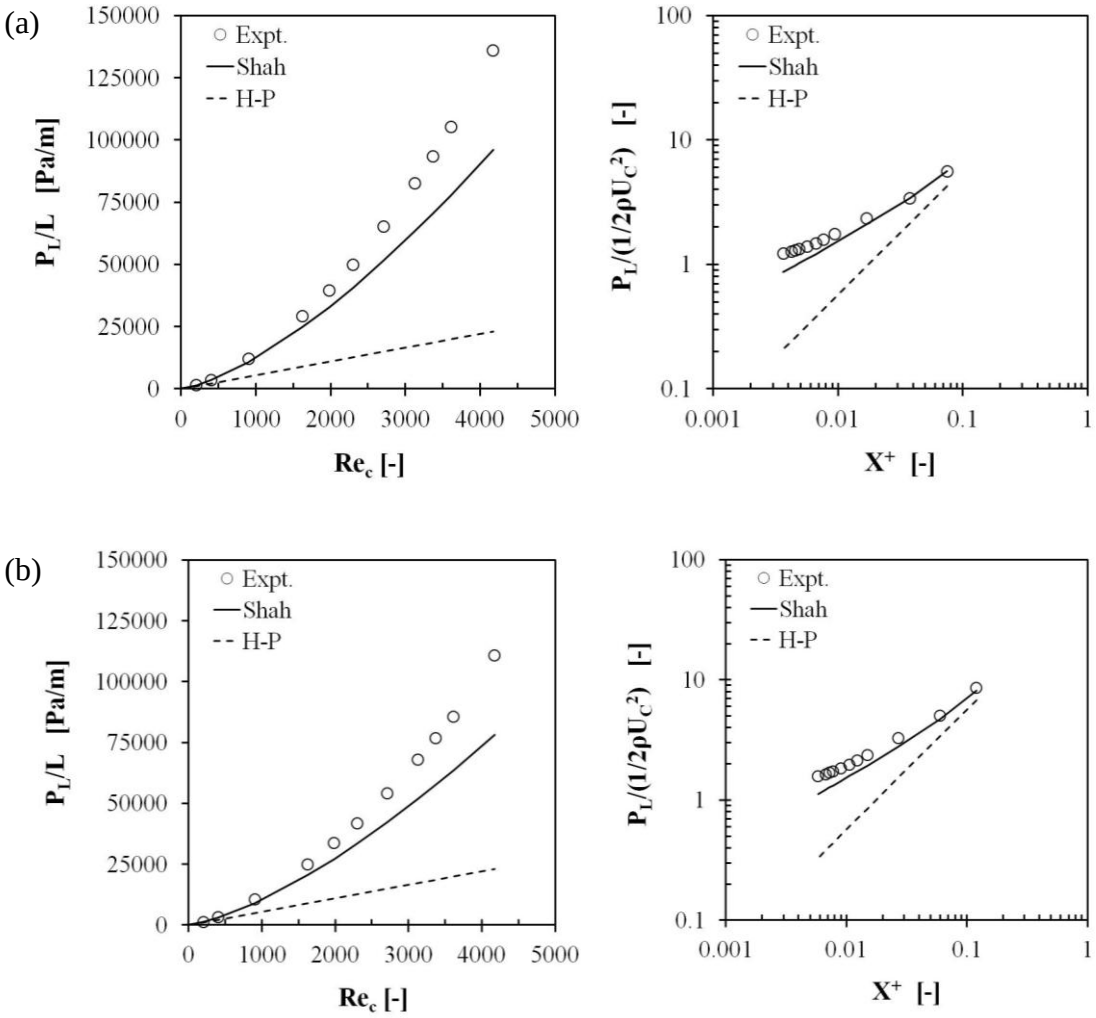

Figure 4.5: Non-dimensional monolith pressure compared with H-P expression and Shah's equation; L [mm] = (a) 17 (b) 27

4.4 Non-dimensional oblique entry pressure loss coefficient, K_{Obl}

The measurements were undertaken at $\alpha = 27^o$, 41^o, 51^o, 61^o and 70^o for a range of Re ($200 \leq Re_a \leq 4090$). Measurements at a relatively low range of Re, i.e. $200 \leq Re_a \leq 2200$, have been presented by Quadri et al. (2009b). With reference to Figure 2.16, the flow spreads over a larger cross-sectional area of the monolith when it approaches the channels at an incidence which reduces the magnitude of U_2. The corresponding P_L in equation (2.11) was determined from the polynomial equations presented on Figure 4.4. At low α, K_{Obl} is obtained from the difference of two relatively large numbers (P_{s1}–P_{s2}) and P_L as seen in equation (2.11) resulting in high uncertainties (Quadri et al. (2009b)). Since the magnitude of P_L is smaller at high α,

the uncertainties were reduced to around ±5% for $\alpha = 70^o$ at $Re_a = 4060$ for all monoliths. Thus the data were excluded when the uncertainty is negative or >100%, which was mainly applicable for cases with low Re and/or low α. A sample of the uncertainty analysis is included in Appendix G.

Figure 4.6(a) shows that measurements correspond well with the equations (1.9) in Table 1.3. The Re effect on K_{Obl} is presented in Figure 4.7 with an error bar of 95% error margin for each marker. It shows that the losses increase with respect to α as predicted by the Quadri et al. (2009b) correlation. In particular the losses increase with Re at low mass flow rates but are independent of Re at high flow rates whereas the correlation derived by Quadri et al. (2009b) suggests there is still a Re effect.

In Figure 4.6(b) the measurements were compared with theoretical expressions of K-W, M-T and Persoons et al. (2008), defined by equations (1.6), (1.7) and (1.8) respectively in Table 1.3. The K-W expression shows poor predictions while M-T underestimated the losses at low angles of incidence. Comparison with Persoons et al. (2008) is not applicable as the correlation was deduced at relatively low α where the uncertainties are high.

The sensitivity of the transverse dynamic pressure losses were shown in Figure 4.6(c) and (d). Better predictions were found if the losses are 20% higher than the transverse dynamic pressure. Figure 4.8 compares the measurements with $K_{Obl} = 1.2\sin^2\alpha$. The expression over predicts the losses at low Re but corresponds well with the data at high mass flow rates.

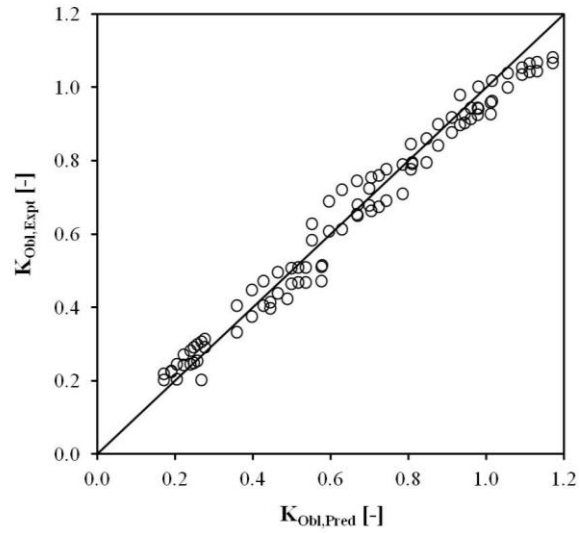

(a)

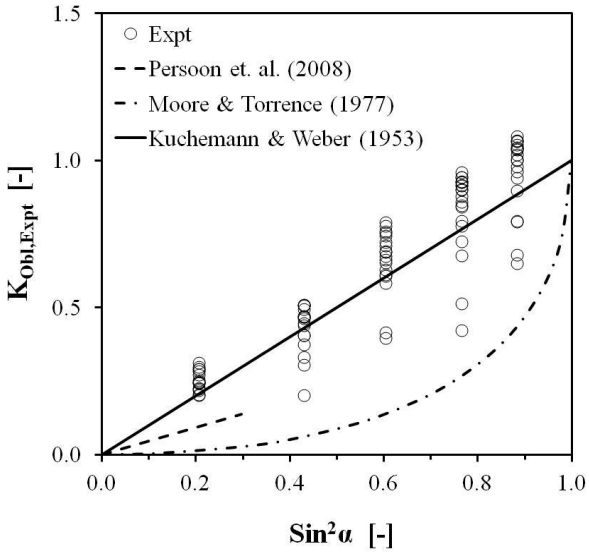

(b)

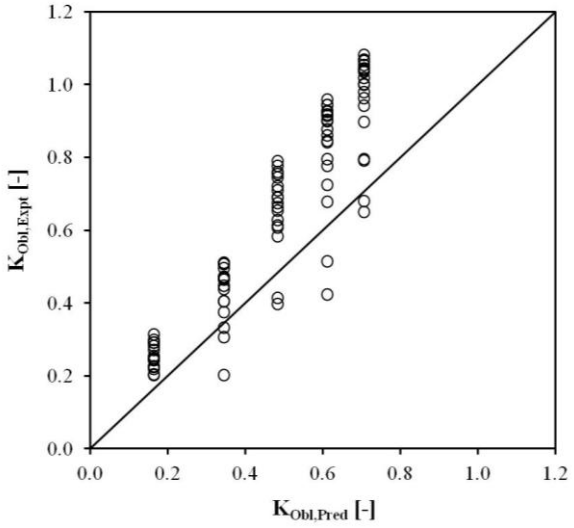

(c)

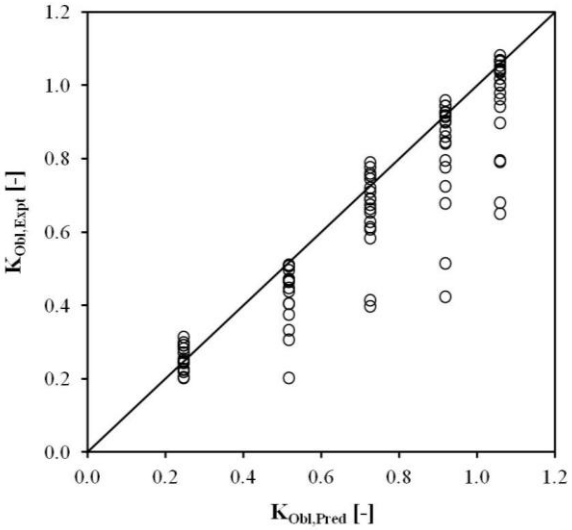

(d)

Figure 4.6: Comparison of K_{Obl} against: (a) Quadri et al. (2009b) correlation, (b) the theoretical assumption of $\sin^2\alpha$, (c) $K_{Obl,Pred} = 0.8\sin^2\alpha$,and (d) $K_{Obl.Pred} = 1.2\sin^2\alpha$

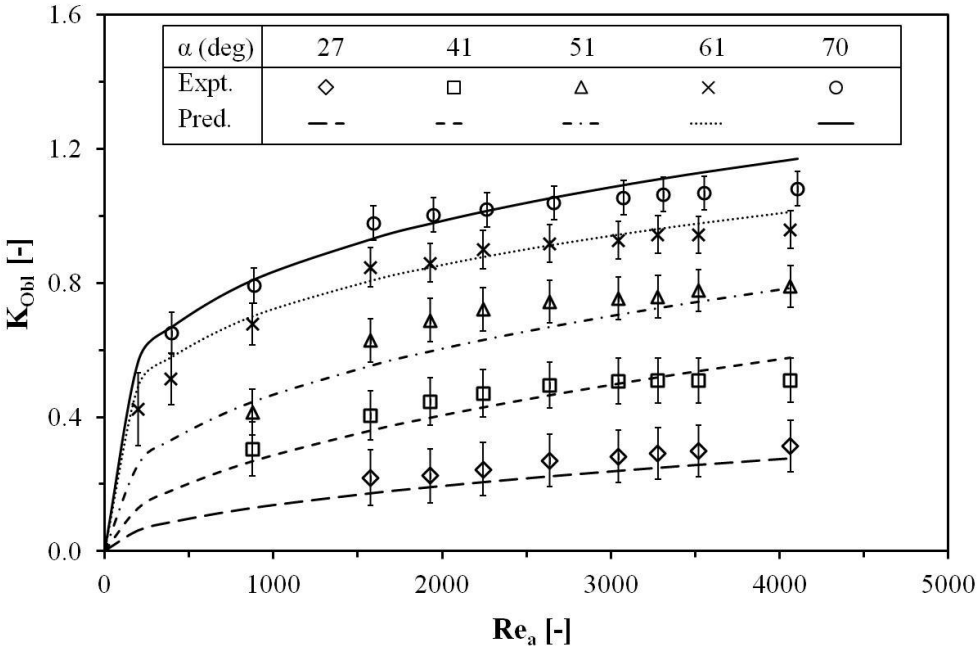

(a) L = 17 mm

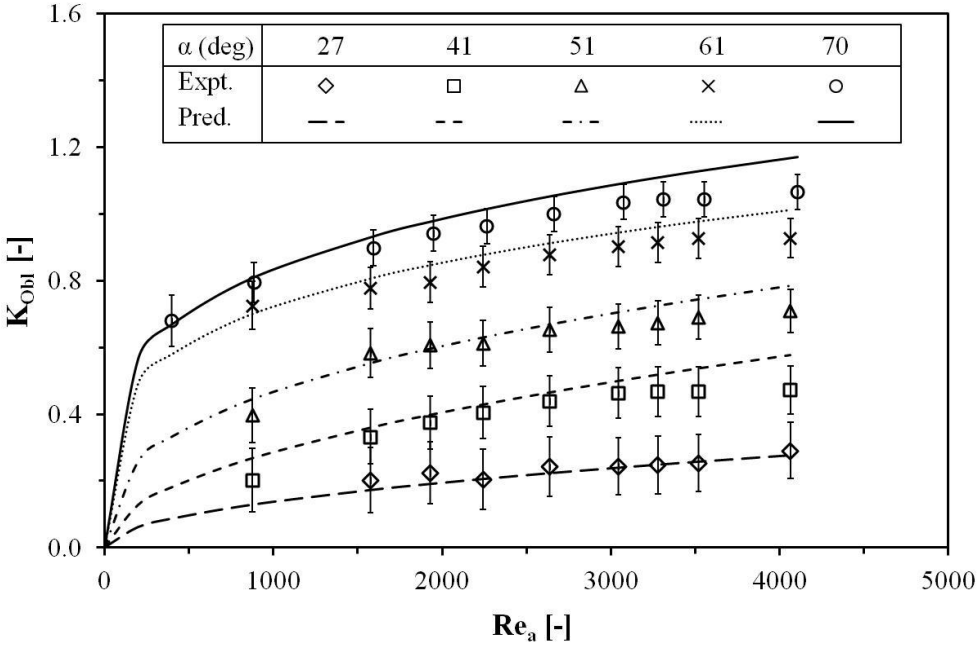

(b) L = 27 mm

Figure 4.7: K_{Obl} dependence on Re_a and comparison with Quadri's et. al. (2008) correlation; L [mm] = (a) 17 (b) 27

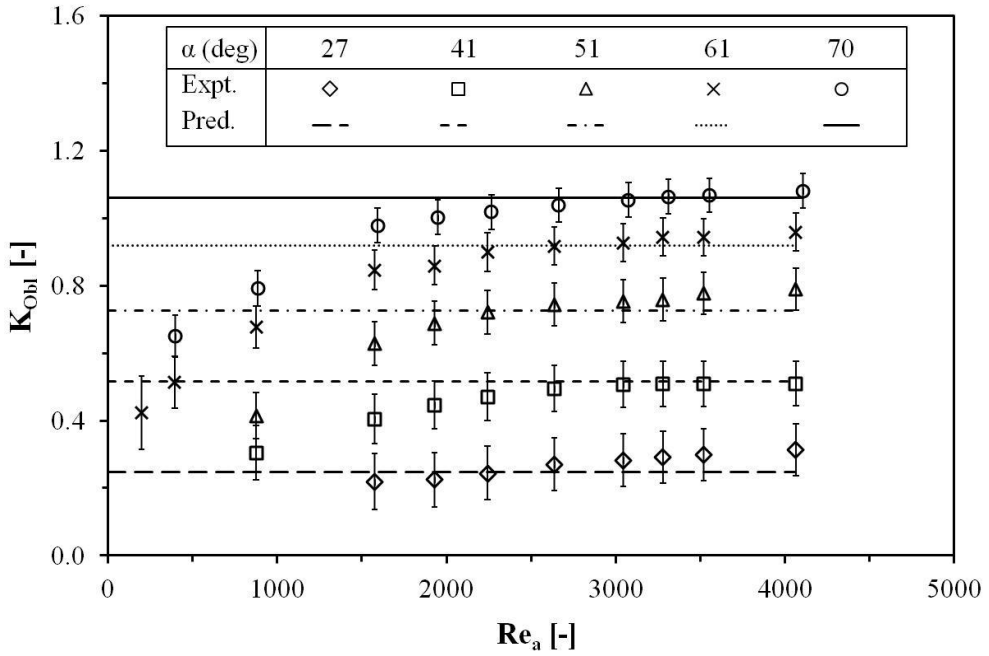

(a) L = 17 mm

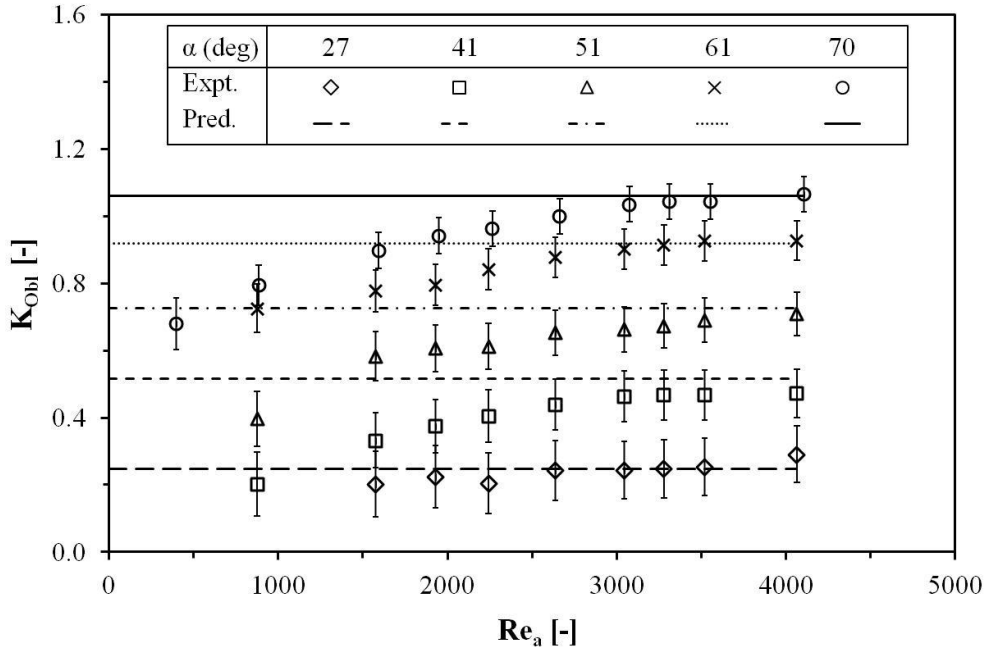

(b) L = 27 mm

Figure 4.8: K_{Obl} dependence on Re_a; L [mm] = (a) 17 (b) 27; $K_{Obl,Pred} = 1.2\sin^2\alpha$

4.5 Summary

An experimental study has been performed to measure the oblique entry loss for flow entering catalyst monolith channels using a methodology derived by Quadri et al. (2009b). The one-dimensional isothermal oblique angle flow rig was redesigned to investigate α_c and the Re effect at high mass flow rates. The former, although originally planned, was not possible due to the unexpected limitation of the test rig. Measurements were performed using different lengths of monolith (17 and 27 mm) over a range of Re ($200 \leq Re_a \leq 4090$) and angles of incidence ($0 - 70^o$). Such measurements have been reported by Quadri et al. (2009b) for a relatively low range of Re ($200 \leq Re_a \leq 2200$).

The results show that the losses increase with α and Re at low mass flow rates but are independent of Re at high flow rates whereas the correlation derived by Quadri et al. (2009b) suggests there is still a Re effect. The K-W expression shows poor predictions while M-T underestimated the losses at low angles of incidence. Comparison with Persoons et al. (2008) is not applicable as the correlation was deduced at relatively low α where the uncertainties are high. Better predictions were found if the losses are 20% higher than the transverse dynamic pressure. This expression over predicts the losses at low Re but corresponds well with the data at high mass flow rates.

CHAPTER 5: FLOW STUDIES OF AXISYMMETRIC CERAMIC AND PERFORATED MONOLITH CATALYSTS

5.1 Introduction

This chapter presents the measurements of flow maldistribution across axisymmetric ceramic and perforated monolith catalysts at two different mass flow rates. Measurements were used to validate the CFD predictions in Chapter 6 which incorporated the oblique flow loss discussed in the Chapter 4. Pressure drop measurements were also made across the monolith when presented with uniform flow at its front face. This provides the axial resistance for the monoliths that were modelled as a porous region in Chapter 6. For the perforated monolith, the measurements of radial flow profiles were obtained downstream of the monolith when presented with non-uniform flow at its front face. In Chapter 6, the profiles were best matched to CFD predictions to deduce the transverse resistance.

5.2 Pressure drop

The results from pressure drop measurements are presented first. Pressure drop was obtained across ceramic and perforated monoliths of 400/6 and 600/1.5 respectively. Measurements were also conducted for a washcoated ceramic monolith, 600/3.5 to compare the pressure drop characteristics between the monoliths. The resistance was measured using two different configurations of air flow rigs as shown in Figure 2.18. For the perforated monolith, the mean velocity was reduced to 20~25 m/s because the inlet flow was evenly distributed over a larger front face of the structure and therefore the pressure drop measurements for the ceramic were limited within this velocity range. With reference to Figure 4.4 and Figure 4.5, the flow within the channels of the ceramic monolith, 400 cpsi was no longer laminar as the channel Reynolds number ~2500 when the mean velocity ~24 m/s. Hence the theoretical expressions such as H-P and Shah (1978) described in Chapter 1 cannot be used to prescribe the pressure drop of the monoliths in the CFD simulations presented in Chapter 6.

Figure 5.1 shows the second order-polynomial curves fitted through the data points. Equation (4.1) was adapted to empirically calculate the pressure loss coefficients derived from the axial flow using the method of least squares. The polynomial equations are presented in Figure 5.1 and the coefficients were included in the CFD predictions to represent the axial pressure loss. A comparison between ceramic structures shows that the high density monolith is roughly 50% more restrictive and produced the higher pressure loss by virtue of its smaller hydraulic diameter. The pressure loss coefficients of the 400 cpsi monolith were much smaller than those used for oblique entry pressure losses in Chapter 4 as shown in Figure 4.4 because the developing boundary layer length is a small fraction of the total length of the monolith and hence the pressure drop per unit length is smaller.

The hydraulic diameter of the perforated monoliths is larger than the ceramic 600 cpsi since the structure is made of thin foils with approximately half the thickness of the cordierite walls. However the measurements showed that the pressure drop difference between the 600/3.5 and the 600/1.5 is small due to the perforation effectively causing the boundary layer to continuously reform along the length of the monolith.

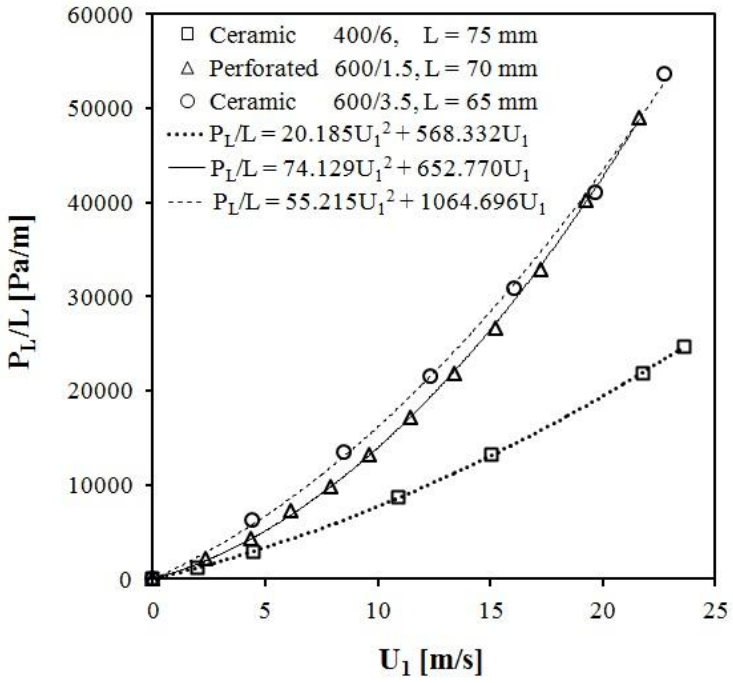

Figure 5.1: Pressure drop normalised against monolith length versus superficial velocity across the monoliths

5.3 Hot-wire velocity profiles

This section presents the hot-wire velocity profiles downstream of three different flow assemblies as shown schematically in Figure 2.21, i.e. Assemblies 1, 2 and 3. For Assembly 1, the ceramic and perforated monoliths, of 400/6 and 600/1.5 respectively, were placed downstream of a conical diffuser of 60^o total angle and the other geometrical data can be found in Table 2.3. The configurations of Assemblies 2 and 3 were designed to obtain the radial flow profiles of the perforated monolith. To provide the validation data for CFD predictions in Chapter 6, the measurements were undertaken at two different Reynolds numbers, i.e. 1.0×10^5 and 1.7×10^5, the latter being limited by the maximum downstream velocity of 20~25 m/s such that the monolith losses can be simulated using the coefficients presented in Figure 5.1.

5.3.1 Flow maldistribution across Assembly 1

Figure 5.2 shows the flow maldistribution across two different monoliths at different mass flow rates. Profiles are acceptably smooth and axially symmetrical along the x (horizontal) and y (vertical) axes. In particular, secondary velocity peaks are observed near the walls of the diffuser upstream of the ceramic monolith. Similar patterns have been observed for the two-dimensional system shown in Figure 3.3. In Chapter 3 the occurrence of the peaks has been explained by the velocity flow fields in the planar diffuser upstream of the monolith. In a similar way, the jet-like flow traverses the diffuser as a result of flow separation at the throat and the flow spreading is significant just upstream of the channel due to the lateral pressure gradient. This radial flow decelerates when it reaches the diffuser walls, hence creating a locally higher pressure which causes the secondary peak to occur.

(a)

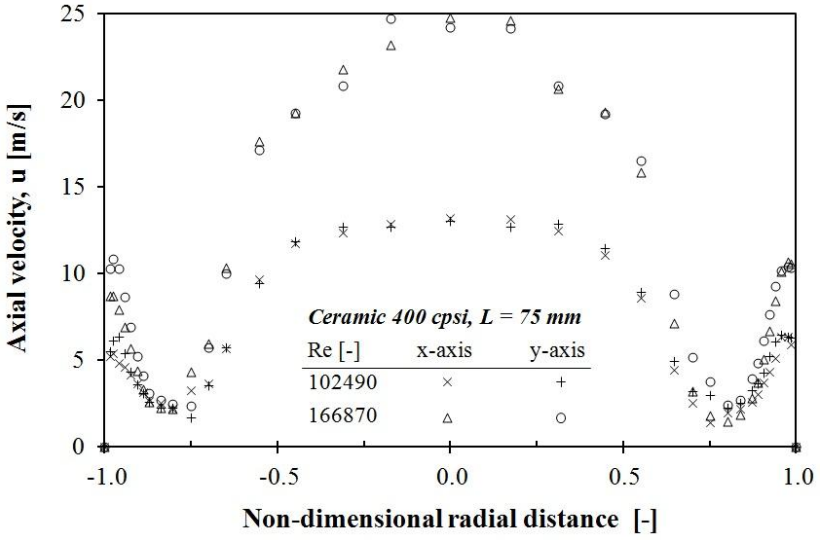

(b)

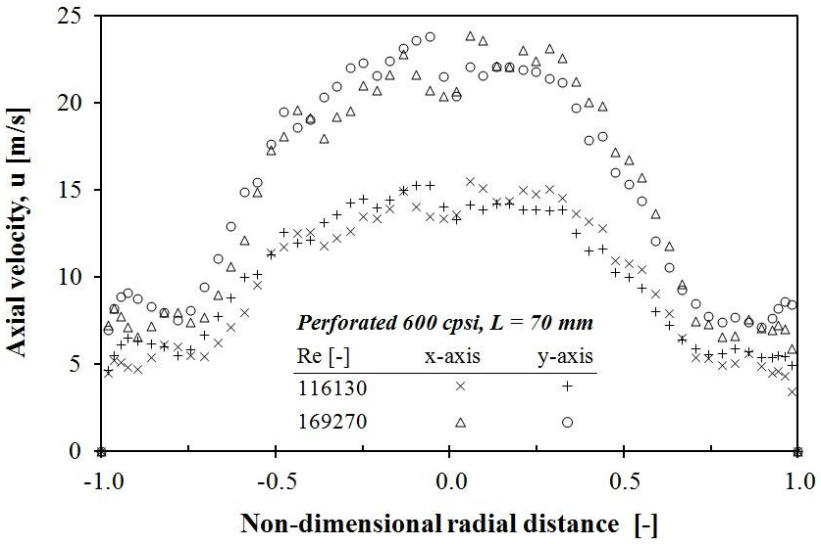

Figure 5.2: Axial flow distribution; (a) Ceramic 400 cpsi, (b) Perforated 600 cpsi; velocity normalized by the mean velocity at the exit of the monolith.

To investigate the Re effect, the profiles have been normalised by the mean outlet velocity, U_2 as shown in Figure 5.3. Flow maldistribution increases with Re for both monoliths, especially for the low density monolith. The maximum velocities in the central region of the ceramic monolith are a factor of two or more greater than the mean. In contrast, the central velocity peak for the perforated monolith is less than that factor. For the perforated monolith with high cell densitiy, the velocity profiles flatten as a result of higher lateral pressure gradients at the front face of the channels and the radial flow from one channel to another due to the pressure differences. The

latter causes the magnitude of minimum velocities to be higher compared to the ceramic monolith and thus eliminates local maxima near the periphery. This pattern has never been reported before and the finding verified the perforation effect within the monolith.

(a)

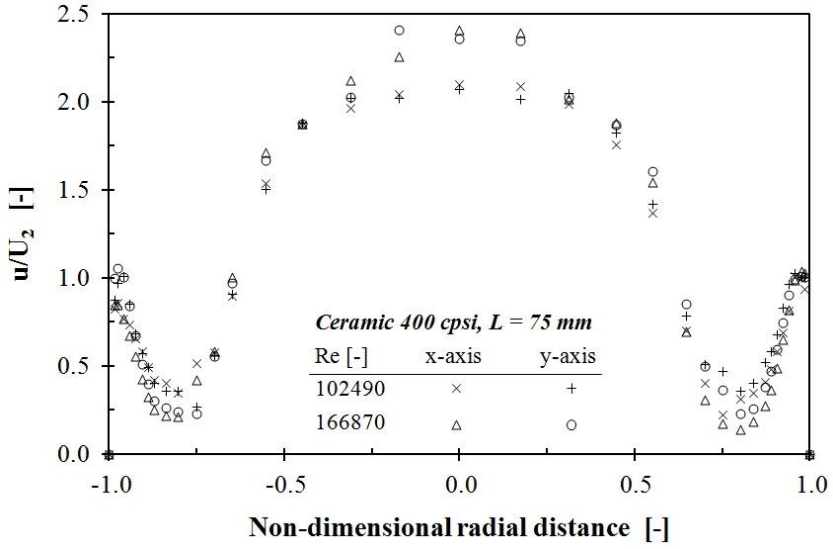

(b)

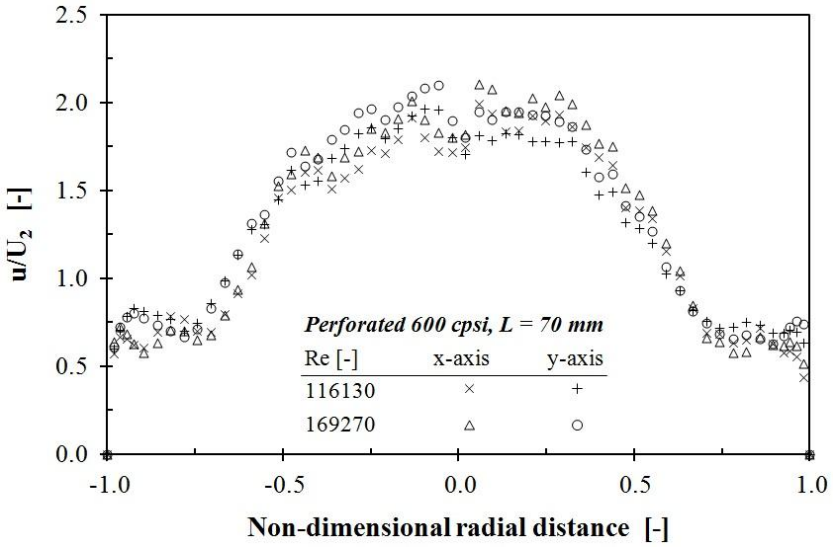

Figure 5.3: Non-dimensional axial flow distribution; (a) Ceramic 400 cpsi, (b) Perforated 600 cpsi; velocity normalized by the mean velocity at the exit of the monolith.

5.3.2 Radial flow profiles downstream of Assemblies 2 and 3

Figure 5.4 shows the radial flow profiles downstream of two different geometries, i.e. Assemblies 2 and 3, overlaid with the inlet velocity profiles at different mass flow rates. It can be seen that the downstream flow was spread over a larger area due to the radial flow within the perforated monolith. In particular, profiles are acceptably smooth and axially symmetrical along the x (horizontal) and y (vertical) axes. With the rear of the monolith partially covered, more flow diffuses laterally within the monolith and thus lower maximum velocities were observed.

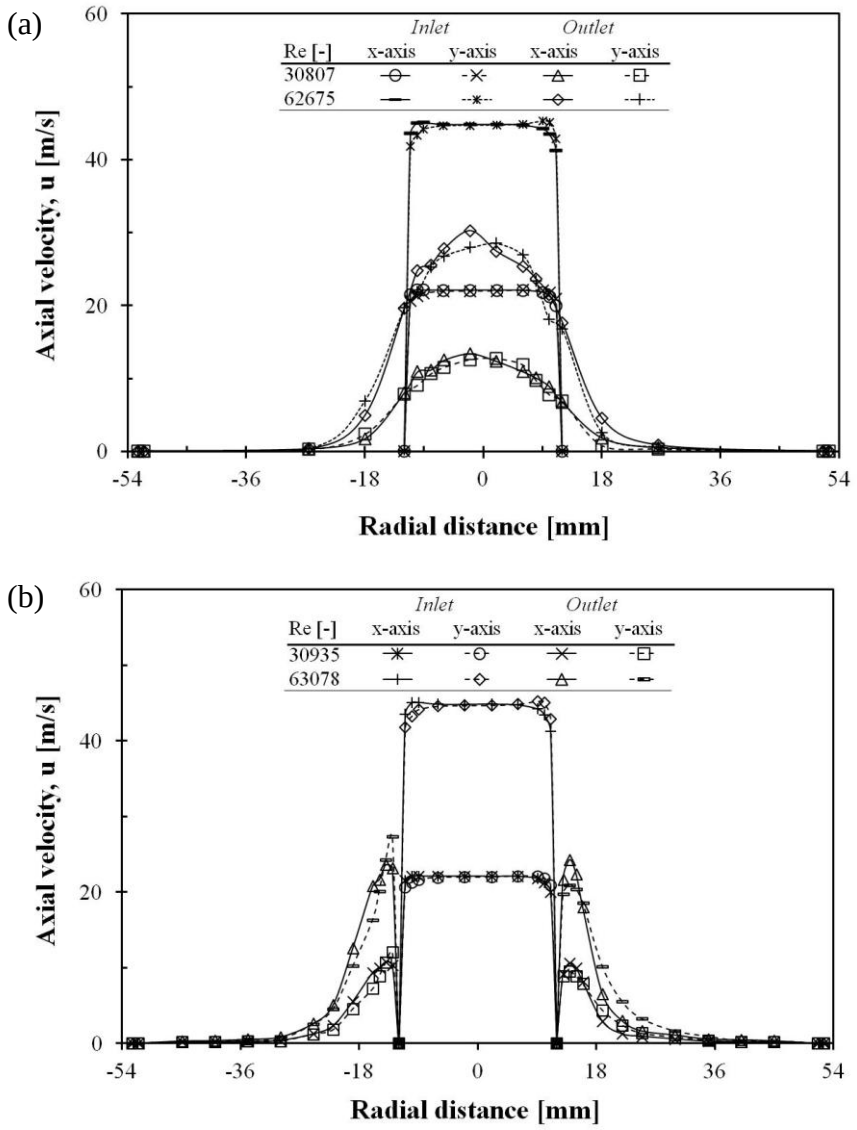

Figure 5.4: Radial flow profiles; (a) Assembly 2, (b) Assembly 3

The profiles were normalised against the mean inlet velocity to investigate the effect of Re as shown in Figure 5.5. Profiles show that the flow is independent of Reynolds number over the range tested. This may indicate that the perforation within the monolith is uniform, i.e. the radial flow within the structures is characterised by a constant transverse resistance coefficient over the range of Re. For Assembly 3, more radial flow occurred which reduces the maximum velocities at the monolith exit. In Chapter 6, the CFD predictions were best matched to these profiles to deduce the transverse resistance to simulate the radial flow within the perforated monolith.

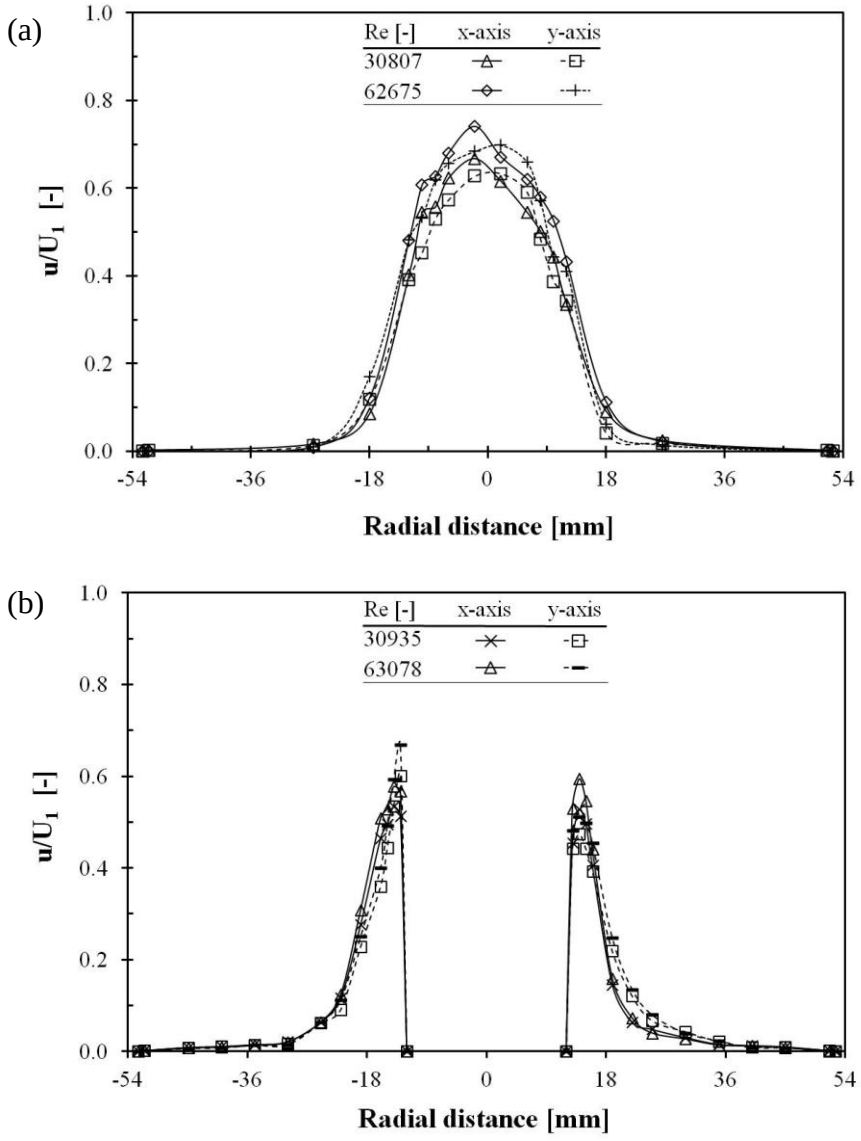

Figure 5.5: Normalised radial flow profiles; (a) Assembly 2, (b) Assembly 3

5.4 Summary

Measurements of the pressure drop and velocity profiles across the ceramic and perforated monoliths have been successfully measured using different axisymmetric geometries. Pressure drop measurements were obtained across ceramic and perforated monoliths by presenting uniform flow to its front face. Second order-polynomial curves were fitted through the data points to deduce the axial resistance coefficients of the monoliths that were modelled as a porous region in Chapter 6. In particular, the 400/6 monolith produced the lowest pressure loss by virtue of its larger hydraulic diameter. Although the perforated monolith was made of thinner walls, a comparison with the 600/3.5 shows that this did not reduce pressure loss significantly. The reason for this is the perforation may effectively cause the boundary layer to continuously reform along the length of the monolith.

Hot-wire velocity profiles were obtained downstream of three different flow assemblies, i.e. Assemblies 1, 2 and 3, at two different Reynolds numbers, i.e. 1.0×10^5 and 1.7×10^5. For Assembly 1, ceramic and perforated monoliths, of 400/6 and 600/1.5 respectively, were placed downstream of a conical diffuser. Flow maldistribution increases with Re for both monoliths, especially for the 400/6 monolith. For the perforated monolith with high cell densities, the velocity profiles flatten as a result of higher lateral pressure gradients at the front face of the channels and the radial flow from one channel to another due to the perforation. The latter causes the magnitude of minimum velocities to be higher compared to the ceramic monolith and thus eliminates local maxima near the periphery. This pattern has never been reported before and the finding verified the benefit of the perforation effect within the monolith.

For the perforated monolith, the measurements of radial flow profiles were obtained downstream of Assemblies 2 and 3. Profiles are independent of Reynolds number over the range tested which may indicate that the perforation within the monolith is uniform. For Assembly 3, more radial flow occurred which reduces the maximum velocities at the monolith exit. In Chapter 6, the CFD predictions were best matched to these profiles to deduce the transverse resistance to simulate the radial flow within the perforated monolith.

CHAPTER 6: CFD MODELLING OF AXISYMMETRIC CERAMIC AND PERFORATED MONOLITH CATALYSTS

6.1 Introduction

CFD predictions of the flow distribution across axisymmetric ceramic and perforated catalyst assemblies up to Re = 1.7 x 10^5 have been performed with the entrance effect discussed in Chapter 4; similar studies have been conducted by Quadri et al. (2009b) for ceramic catalysts up to Re = 8.0 x 10^4. The measurement data for CFD modelling and validation has been presented in the previous chapter. The CFD simulations for both models have been performed using STAR-CCM+ Version 7.02.008, supplied by CD-Adapco Inc. The CFD code is capable of solving flow problems (of fluids or solids), heat transfer and stress based on the finite volume method. With client-server architecture, the simulations are created and solved on the server, while the workspace views these simulations through the client. The client was run on a Windows laptop while the server was run on a Linux cluster.

6.2 Porous medium approach

An automotive monolith consists of thousands of channels and can be modelled as porous medium with a distributed resistance to reduce computational demands. In STAR-CCM+, the resistance is prescribed by a source term, f_p that is added to the momentum equation given by:

$$f_p = -P \,.\, v \tag{6.1}$$

where *v* is the superficial velocity and *P* is the porous resistance through the medium in three-mutually perpendicular directions; the latter is defined as:

$$P = P_i|v| + P_v \tag{6.2}$$

Equation (6.2) can be rewritten as the pressure drop per unit length as:

$$\Delta P/_L = -(P_i|v| + P_v)v \tag{6.3}$$

where P_i (kg/m^4) and P_v (kg/m^{3}s) are the inertial (quadratic) and the viscous (linear) resistance tensors, respectively which can be determined experimentally or derived using various empirical relationships. This equation is identical to the second order polynomial described in section 4.3. An additional pressure loss due to the entrance effect as the flow obliquely enters the channels can be incorporated as follows:

$$\frac{\Delta p}{L} = -\left(P_i|v| + \left[P_v + \frac{(\frac{1}{2}\rho {u_1}^2)K_{Obl}}{Lv} \right] \right) v \qquad (6.4)$$

During simulation, a set of field functions was defined to calculate the linear term on the right-hand side of equation (6.4) based on the approach velocity, u_1 in each cell along the first layer of fluid region upstream of the porous medium. The total viscous resistance was extracted to the table(x,y,z) using a macro to spatially apply to the porous region. Examples of the macro and field functions used in this study are shown in Appendix H and Appendix I respectively.

6.3 Numerical model

The flow is steady, incompressible, axisymmetric and turbulent. The governing equations are the Navier Stokes equations which are transformed into time averaged equations using RANS approach to reduce the computational effort. The constant density model was selected for incompressible flow, i.e. the density is invariant throughout the continuum.

Axisymmetric models for geometrically different flow assemblies are illustrated in Figure 6.1 with the flow direction along the x-axis. The computational domains were developed identical to the experimental geometries described in section 2.5.2. Assembly 1 consists of four sections; 1) inlet pipe, 2) conical diffuser, 3) cylindrical monolith and 4) outlet sleeve. The diffuser was not in place for other assemblies and a cylindrical rod was situated downstream of the monolith in Assembly 3. The two-dimensional grids were converted from one-cell-thick three-dimensional meshes constructed on the x-y plane and oriented such that the axis of rotation located at y = 0 in global coordinate space with no part of the meshes below y = 0.

The V2F model was used to simulate turbulence upstream and downstream of the monoliths. The upstream flow simulations are particularly challenging due to the adverse pressure gradient created by the decelerating flow resulting in flow separation with a large recirculation bubble. The velocity flow fields for steady and pulsating cases have been presented in Chapter 3 for planar geometries. The V2F model is known to accurately predict the flow separation by resolving the viscous sublayer provided the mesh is sufficiently fine, i.e. y^+ to be approximately 1 or less, hence wall laws are not needed. The y^+ value is a non-dimensional point spacing from the wall given by:-

$$y^+ = \frac{yu^*}{\nu} \tag{6.5}$$

where y is the normal distance from the wall to the wall-cell centroid, u^* is a reference velocity and *v* is the kinematic viscosity. The reference velocity is derived from a turbulence quantity specific to the particular turbulence model even though it is often related to the wall shear stress ($u^* = \sqrt{\tau_w/\rho}$).

Grid dependency studies were performed on three different grid levels, i.e. fine, medium and coarse grids as shown in Figures 6.2 to 6.5. Grids were generated using trimmer volume mesh with the prism layer next to wall boundaries. The trimmer meshing model provides predominantly hexahedral mesh with capability to control the desired cell size away from the surface, that is, in the core. Prism layers are 15 cells in the cross-stream direction with a stretch factor of 1.3 so that the cell density is gradually denser closer to the wall. The stretch factor is defined as the ratio of the thickness of one cell layer to the thickness of the cell layer beneath it. The cell size in the core and the thickness of the prism layers were also adjusted to ensure a smooth cell transition from the core to the prism layer and each grid had an initial grid point spacing of $y^+ = 1.0$ as listed in Table 6.1.

Table 6.1: Main parameters for using trimmer volume mesh with prism layer

Grid	Fine	Medium	Coarse
Cell size [mm]	0.5	1	2
Prism layer thickness [mm]	2	4	8

There are four edges bounding the solution domain namely; the inlet boundary, the wall boundary, the outlet boundary and the axis boundary. An axisymmetric model is defined when the boundary edge that lies along the axis was set as type axis. The inlet was defined as a velocity inlet where the experimental data was used to specify the profiles of velocity and turbulent intensity with the length scale prescribed as 1/10 of the diameter of the inlet pipe. At the outlet, the boundary was assigned as a pressure outlet. No-slip boundary conditions were applied along the solid walls.

In this study, the monolith permeability was specified as orthotropic, i.e. different resistance values in each of two mutually-orthogonal directions. For the ceramic monolith, the fluid in the porous region cannot flow in any direction other than the bulk flow (x-) direction and therefore P_i and P_v values in the cross-flow (y-) direction are set to very large values to suppress the flow in those directions, i.e.

$$P_i = \begin{bmatrix} 20.185 & 0 \\ 0 & 1x10^6 \end{bmatrix} kg/m^4 \text{ and } P_v = \begin{bmatrix} 568.332 & 0 \\ 0 & 1x10^6 \end{bmatrix} kg/m^3s$$

For the perforated monolith $P_{v,y}$ was assumed as a very small value, i.e. 0.0001 whilst $P_{i,y}$ was determined by matching the CFD predictions to the velocity measurements.

$$P_i = \begin{bmatrix} 74.129 & 0 \\ 0 & P_{i,y} \end{bmatrix} kg/m^4 \text{ and } P_v = \begin{bmatrix} 652.770 & 0 \\ 0 & 0.0001 \end{bmatrix} kg/m^3s$$

The coefficients for axial resistance were obtained from measurement as presented in Figure 5.1. For grid independency studies, $P_{i,y}$ was assumed as 15000 kg/m^4. The turbulence parameters in the porous region were specified as intensity and length scale. The turbulence intensity and length scale were approximated as 0.01% and 1/10 of the monolith channel diameter respectively.

A second-order upwind discretization scheme was used for the convective terms in momentum equation and turbulent quantities to ensure satisfactory accuracy, stability and convergence. With the segregated flow solver, the continuity and the momentum equations were solved sequentially according to the SIMPLE (Semi-Implicit Method for Pressure-Linked Equations) algorithm. The solutions reach convergence typically after 3000 iterations. The stopping criterion consisted of

monitoring variation in pressure drop, conservation of mass within the diffuser and reduction of several orders of magnitude in the residual error.

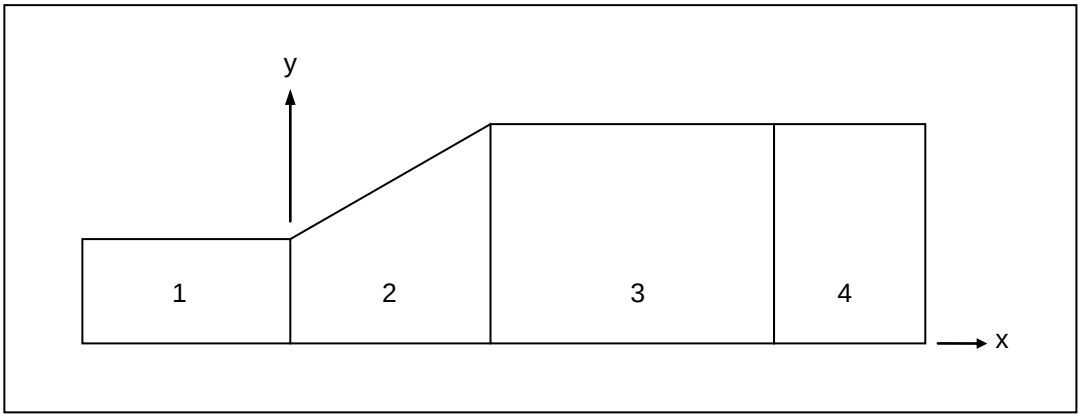

(a) Assembly 1

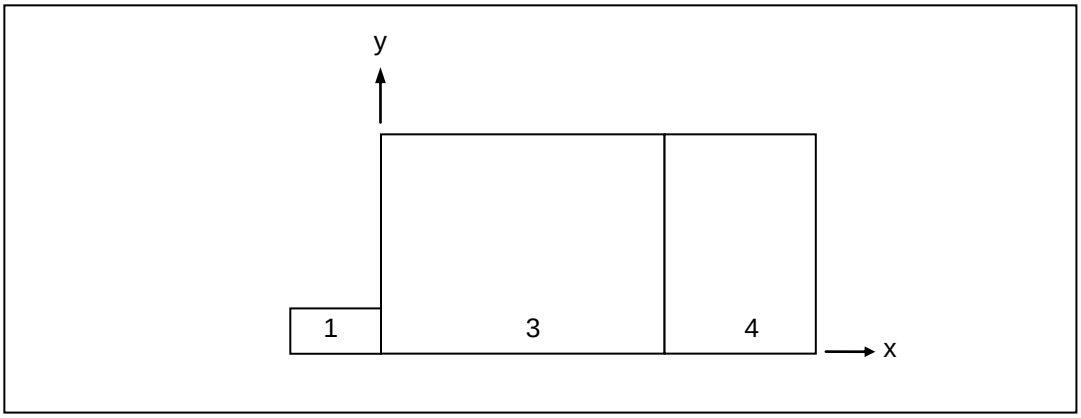

(b) Assembly 2

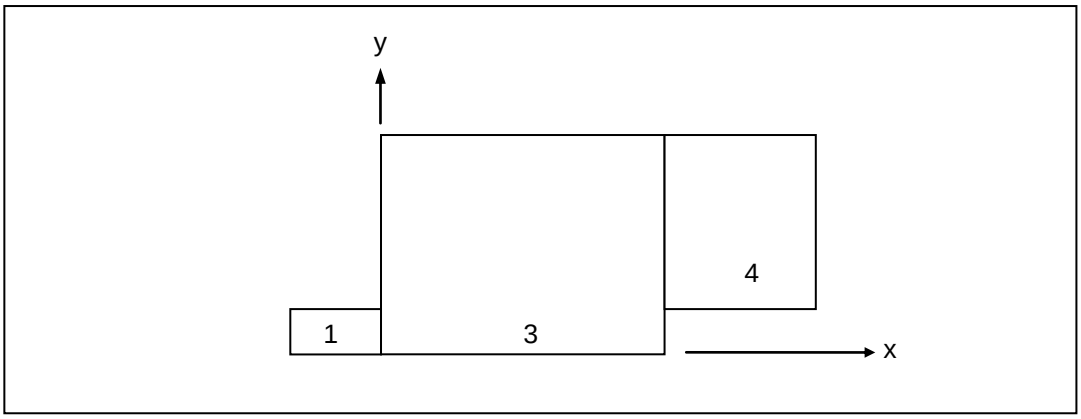

(c) Assembly 3

Figure 6.1: Computational domain for geometrically different flow assemblies

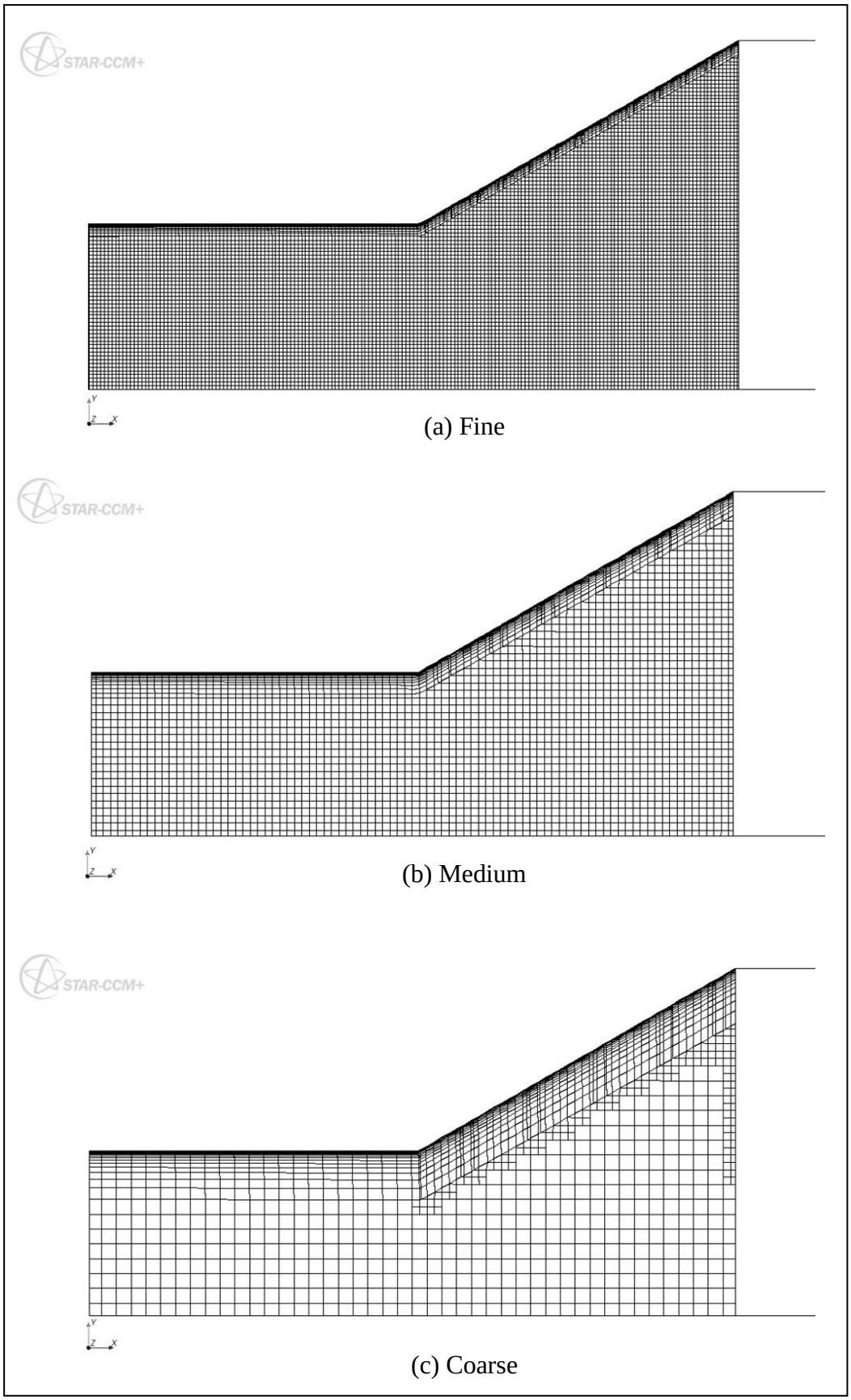

Figure 6.2: Computational grid of the inlet duct and the diffuser upstream of the ceramic monolith catalyst

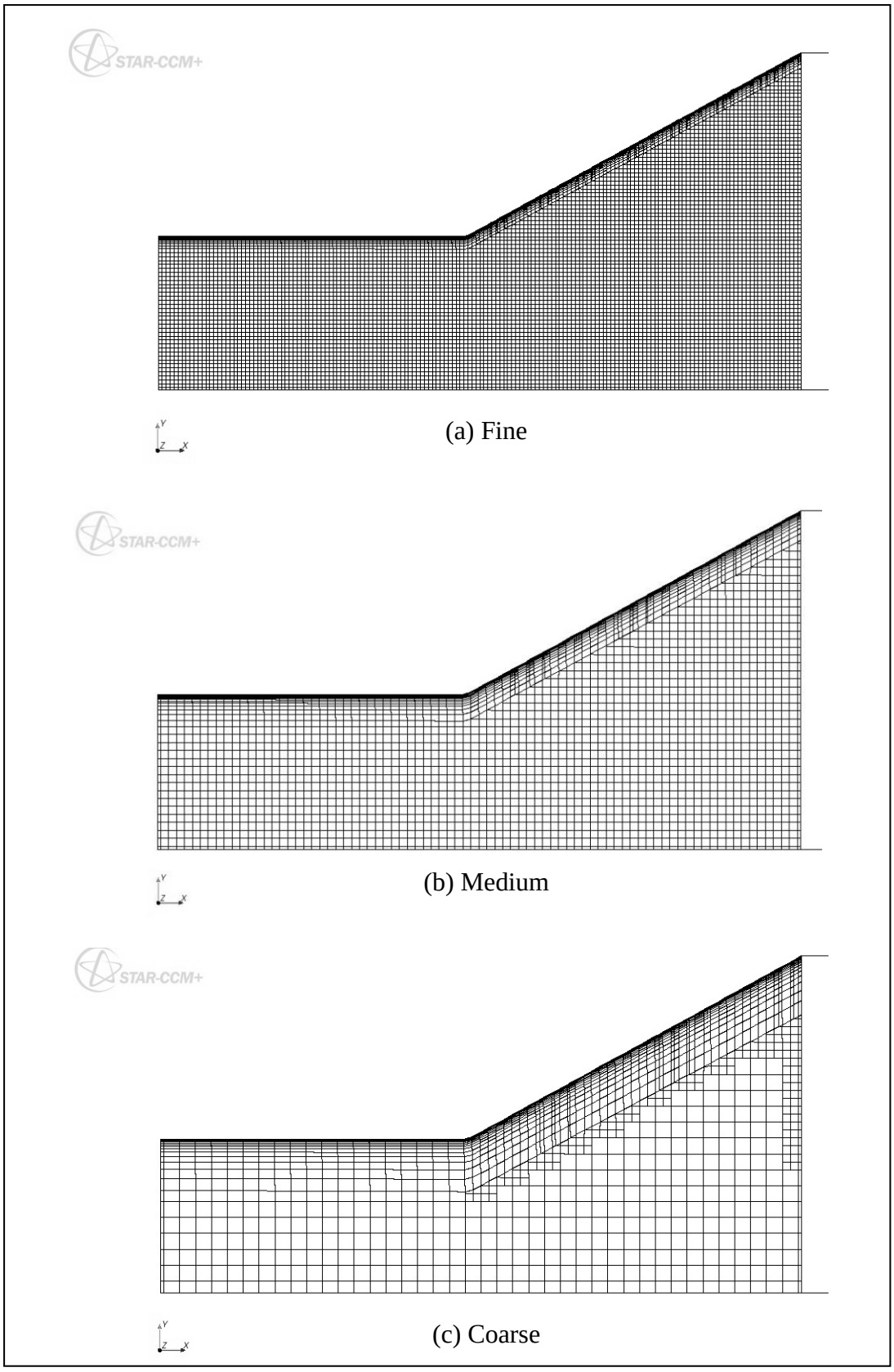

Figure 6.3: Computational grid of the inlet duct and the diffuser upstream of the perforated monolith catalyst

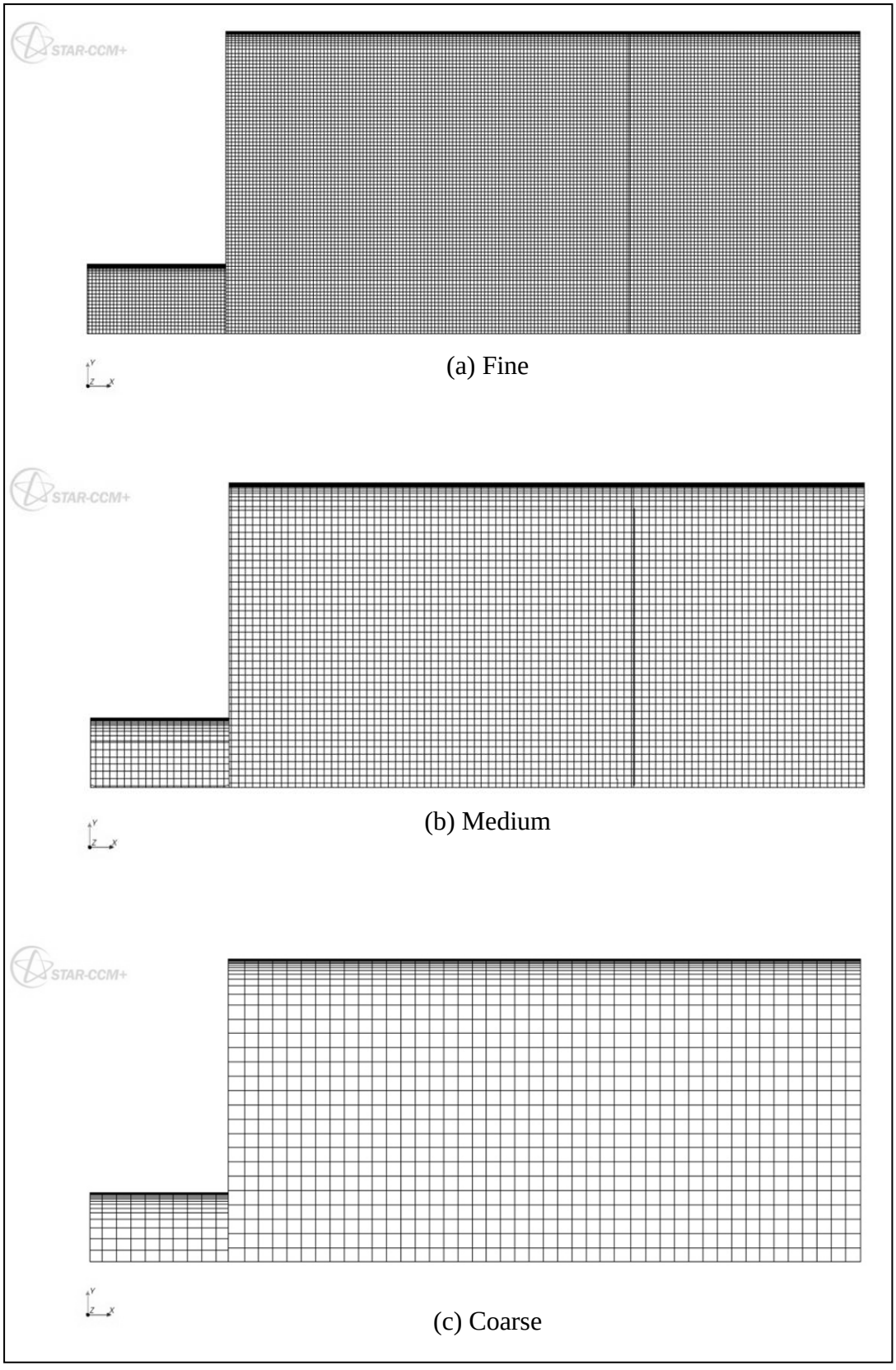

Figure 6.4: Computational grid for the Assembly 2

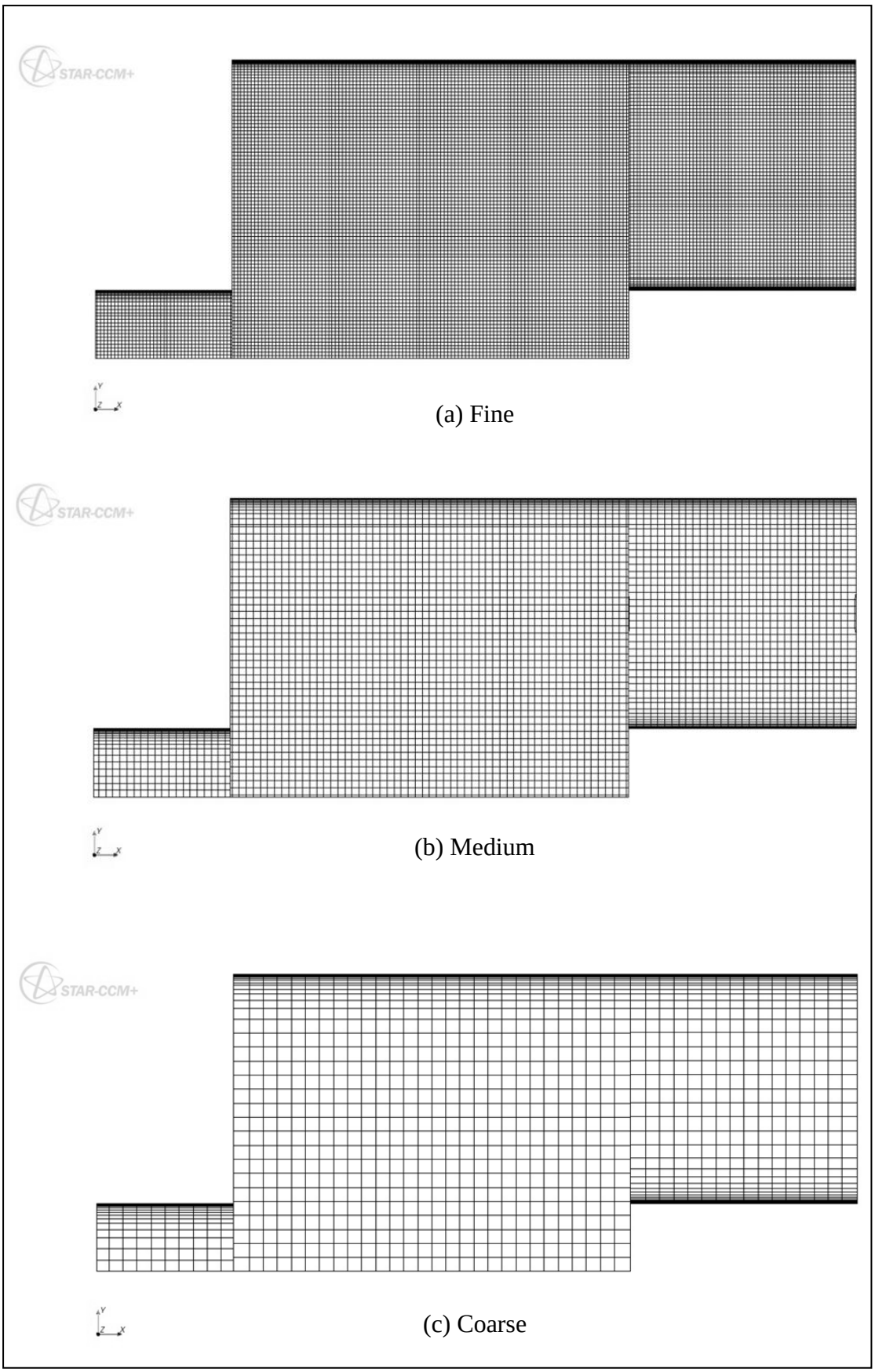

Figure 6.5: Computational grid for the Assembly 3

6.4 Results and discussions

6.4.1 Grid dependency study

A grid dependency study was conducted for all assemblies with different grid resolutions as shown in Tables 6.2 to 6.5. The y^+ next to the wall was approximately 1 or less. The medium and fine grid show much smaller variation in pressure drop prediction than the coarse grid. Thus the medium configuration was chosen as it was considered to have consistency across varying cell sizes.

Table 6.2: Grid dependency data at Re =102490 for Assembly 1 (Ceramic)

Grid	Fine	Medium	Coarse
No. of cells	32152	9370	3374
Total pressure drop [Pa]	142.2	142.5	143.2

Table 6.3: Grid dependency data at Re = 116130 for Assembly 1 (Perforated)

Grid	Fine	Medium	Coarse
No. of cells	27955	8273	3055
Total pressure drop [Pa]	327.6	327.5	328.9

Table 6.4: Grid dependency data at Re = 30810 for Assembly 2

Grid	Fine	Medium	Coarse
No. of cells	18700	5490	1622
Total pressure drop [Pa]	1279.8	1280.5	1557.6

Table 6.5: Grid dependency data at Re = 30940 for Assembly 3

Grid	Fine	Medium	Coarse
No. of cells	18238	5414	1734
Total pressure drop [Pa]	1522.2	1522.7	1909.0

6.4.2 CFD predictions of transverse resistances

The axial resistance of the perforated monolith has been measured by presenting uniform flow to its front face as presented in Figure 5.1. The transverse resistance can be deduced by best matching CFD predictions to the measurements of the radial profiles obtained downstream of the monolith when presented with non-uniform flow at its front face. Measurements were undertaken for geometrically different flow assemblies and various flow rates to establish the generality of the method for obtaining the resistance coefficient. Figure 6.1 shows the inlet configurations in Assemblies 2 and 3 to diffuse the radial flow within the catalyst, in the latter assembly a cylindrical rod was placed at the rear of the catalyst to produce a pure radial flow. With a fair degree of trial and error and the transverse viscous inertial, $P_{v,y}$ was assumed to be a very small value, i.e. 0.0001, the best value was found when $P_{i,y} = 125000$ kg/m^4.

Figure 6.6 and Figure 6.7 show the velocity distribution downstream of the perforated catalyst at two different Re obtained from the measurements and CFD predictions. Axisymmetric simulations at different mass flow rates in Assembly 2 acceptably correspond to the experimental data. Similar features can be observed for Assembly 3. The independency of the transverse coefficient might be due to the uniform perforation within the catalyst resulting in well distributed radial resistance. CFD modelling using axisymmetric approach has successfully deduced the transverse coefficient of the catalyst. This method offers a lot of advantages for both measurement and prediction study. The former requires fewer measurements to characterise the radial flow within the catalyst. While the computational effort to simulate the two-dimensional cases is less demanding.

Section 6.4.3 presents the predictions of the flow maldistribution across the perforated and ceramic catalysts placed downstream of a wide-angled diffuser. Simulations were performed with and without the oblique flow loss to assess the effect of the flow entering the catalyst channels at incidence.

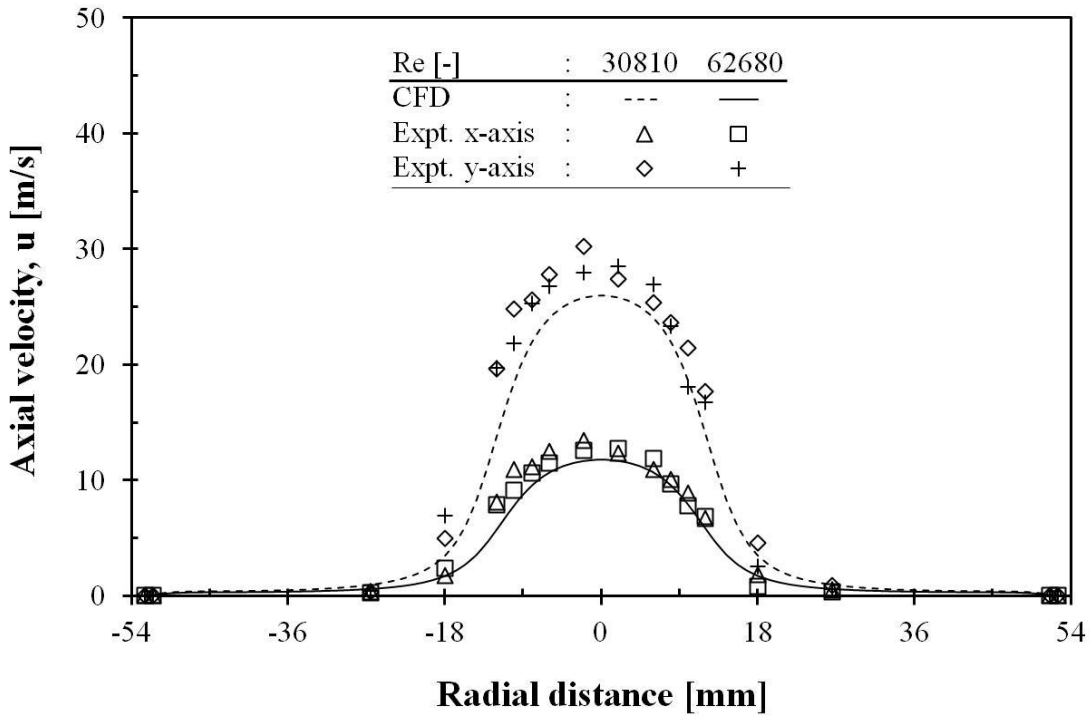

Figure 6.6: Velocity distribution across the perforated catalyst for Assembly 2

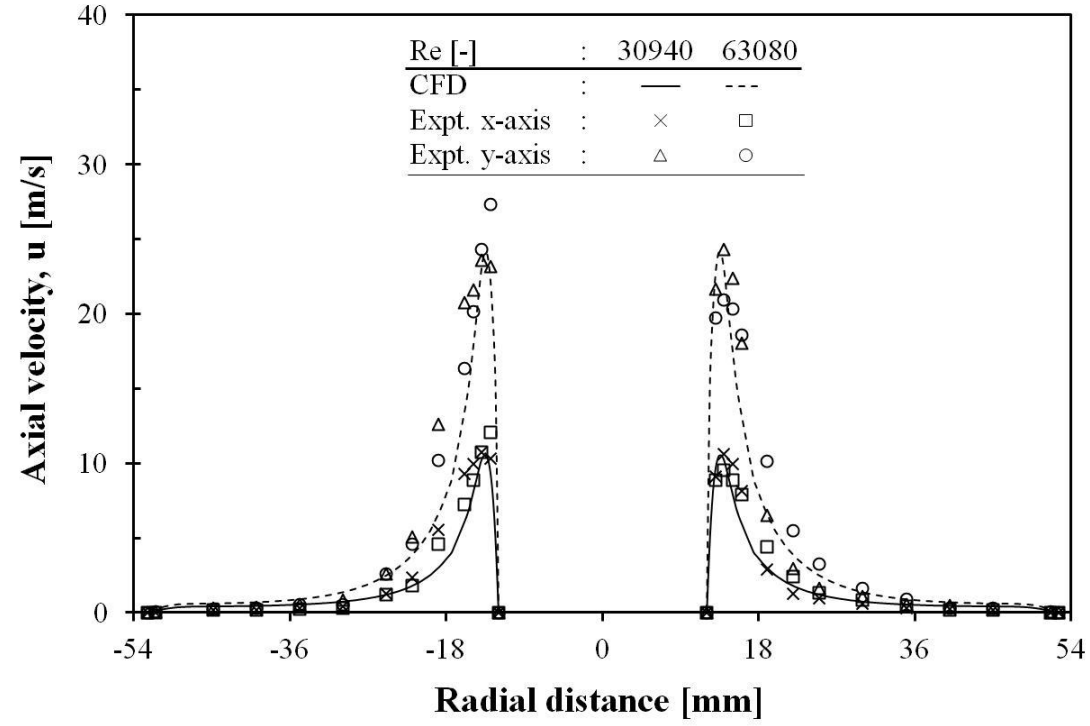

Figure 6.7: Velocity distribution across the perforated catalyst for Assembly 3

6.4.3 CFD predictions of flow maldistribution

CFD simulations were performed on axisymmetric models to predict the flow maldistribution within the monoliths located downstream of a conical diffuser. Simulations with and without the entrance effect were performed across different monoliths, i.e. ceramic 400 cpsi and perforated 600 cpsi, for two flow rates and compared with the experimental data presented in the section 5.2. Similar CFD validation studies have been performed by Quadri et al. (2009b) for ceramic 400 cpsi up to Re = 8.0 x 10^4 using the H-P expression to simulate the monolith pressure drop. In the present study, the simulations were performed up to Re = 1.7 x 10^5 and thus the theoretical expression in not applicable as described in the section 5.3. The critical angle approach was also included in the simulations to improve the prediction of the minimum velocities near the walls as suggested by Quadri et al. (2009b).

Figure 6.8 to Figure 6.11 show the CFD predictions of flow maldistribution across the monoliths superimposed with the experimental data. It can be seen that CFD predictions without the entrance effect under predicts the flow maldistribution. The central velocities have been under predicted to the same degree for both monoliths. With the entrance effect, the velocities in the centre of monolith were improved but the predictions were too low in the region of ~15 mm from the wall. The oblique entry loss in this region is very high relative to monolith resistance prescribed by the polynomial equations as the flow enters the channels at high incidence. Therefore the flow is forced towards the wall resulting in over predicted velocities near the wall region.

Quadri et al. (2009b) have attempted to improve the prediction of minimum velocities by restricting oblique entry pressure losses in this region, i.e. such losses were assumed as constant above a critical angle of incidence, α_c. They found much better agreement with experimental data when $\alpha_c = 81^o$. This approach was justified by assuming the channel height restricts the size of separation bubble at the entrance and thus prevents the over-predicted oblique entry pressure losses.

With $\alpha_c = 81^o$, a good agreement was achieved for the perforated catalyst (see Figure 6.10 and Figure 6.11) while the minimum velocities were over predicted for the ceramic monolith (see Figure 6.8 and Figure 6.9). However the minimum velocities

were improved when $\alpha_c = 85^o$ for the ceramic catalyst. This might be because the separation bubble at the monolith entrance is restricted by the different size of the channel, i.e. the smaller hydraulic diameter of perforated monolith limits the oblique entry loss to a lower incidence angle. Observations on the velocities in the centre region show a small sensitivity with respect to the critical angles.

CFD predictions were also incorporated with K-W expression and $K_{Obl} = 1.2 \sin^2\alpha$. In Chapter 4, the K-W expression shows a poor prediction of the entrance effect and yet better predictions at high Re if the losses are 20% higher than the transverse dynamic pressure. Applying these to the CFD predictions provided good agreement with the experimental data. It can be seen that all the correlations predict similar values of oblique pressure losses for this velocity range. Similar features have been reported by Quadri et al. (2009b).

Figure 6.12 compares the flow maldistribution between the ceramic and perforated monoliths using the CFD data. The Quadri et al. (2009b) correlation was used to simulate the entrance effect with critical angles of 85^o and 81^o for ceramic and perforated catalysts, respectively. It can be seen that the maximum velocities within the ceramic monolith is a factor of two greater than the mean, whilst the flow distribution within the perforated monolith is more uniform due to the radial flow caused by the perforation within the monolith. As a result, the minimum velocities near the walls are higher than the ceramic monolith. Such data from CFD models is useful to optimise the performance of the catalysts.

The entrance effect for these CFD predictions is clearly needed to prevent the under-predicted flow maldistribution within the monolith. Investigations to restrict the oblique entry pressure losses have improved the predictions of the minimum velocities. However it is based on an implicit assumption that the flow within the diffuser located upstream of the monoliths is correct.

(a)

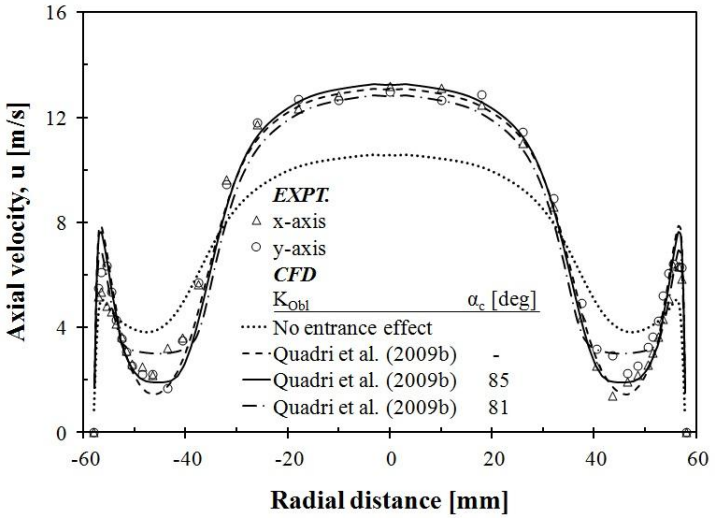

(b)

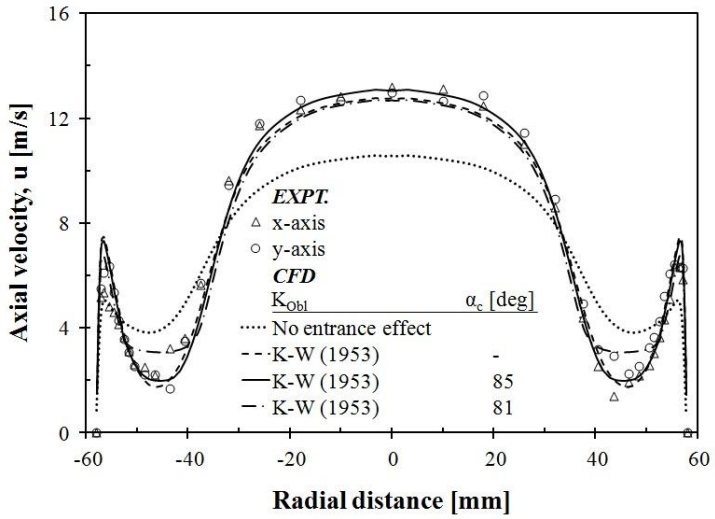

(c)

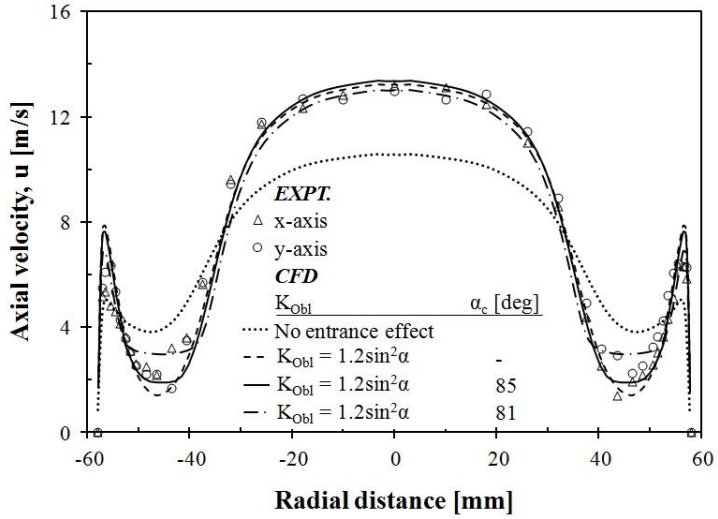

Figure 6.8: Comparison between experimental data (symbols) and CFD predictions (line curves) for the ceramic monolith 400 cpsi at Re = 102490.

(a)

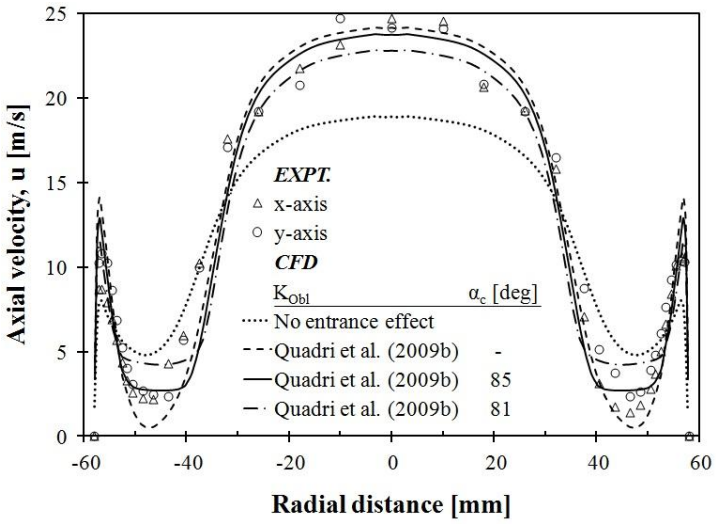

(b)

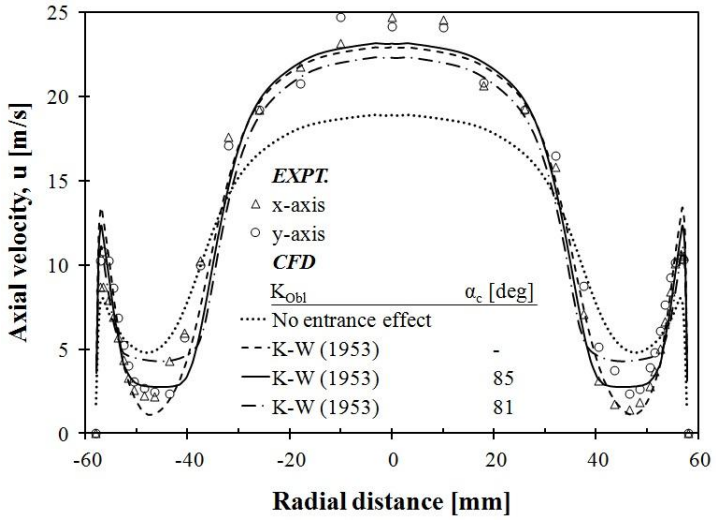

(c)

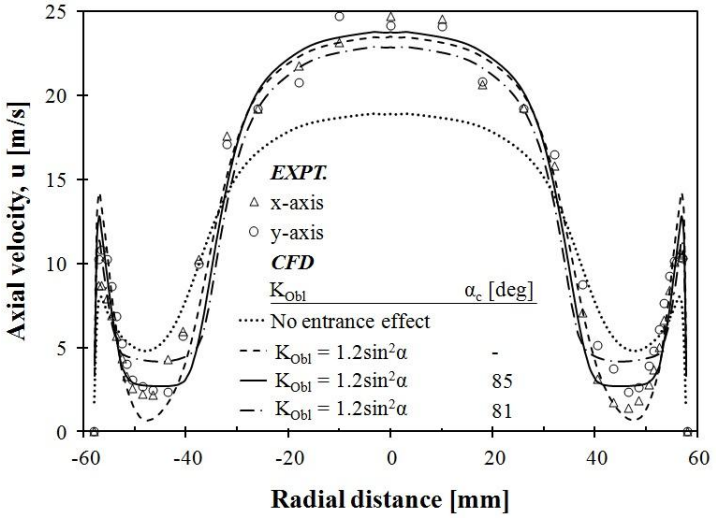

Figure 6.9: Comparison between experimental data (symbols) and CFD predictions (line curves) for the ceramic monolith 400 cpsi at Re = 166870.

(a)

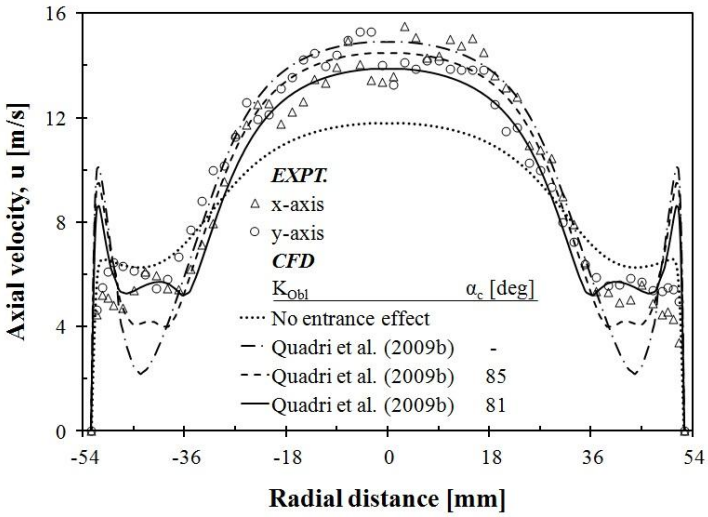

(b)

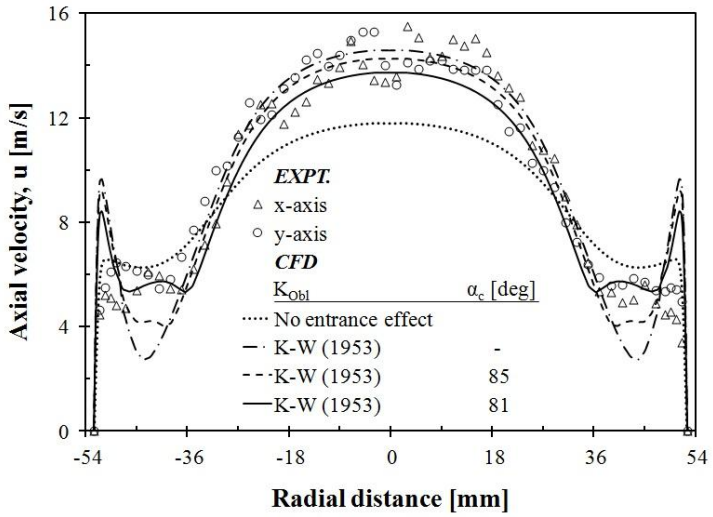

(c)

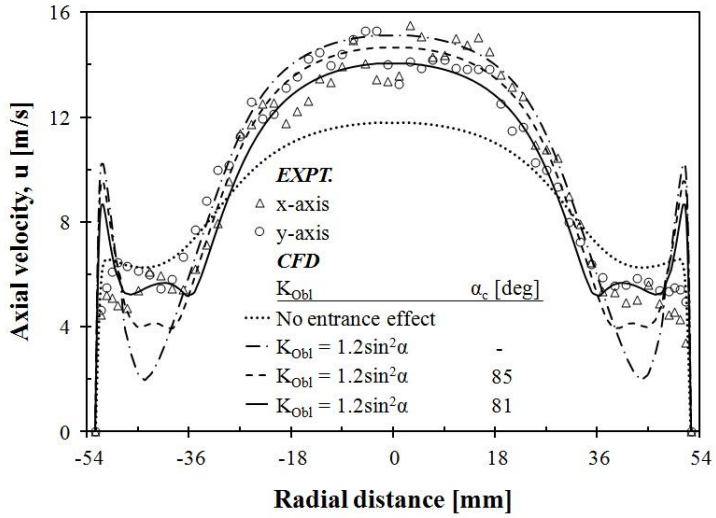

Figure 6.10: Comparison between experimental data (symbols) and CFD predictions (line curves) for the perforated monolith 600 cpsi at Re = 116130.

(a)

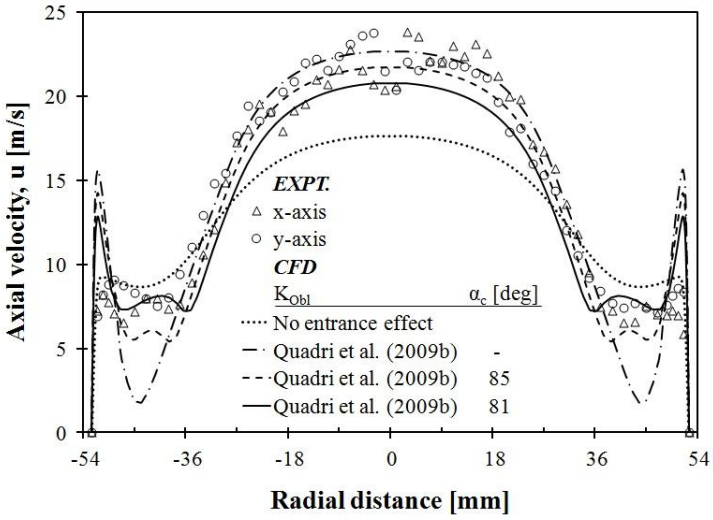

(b)

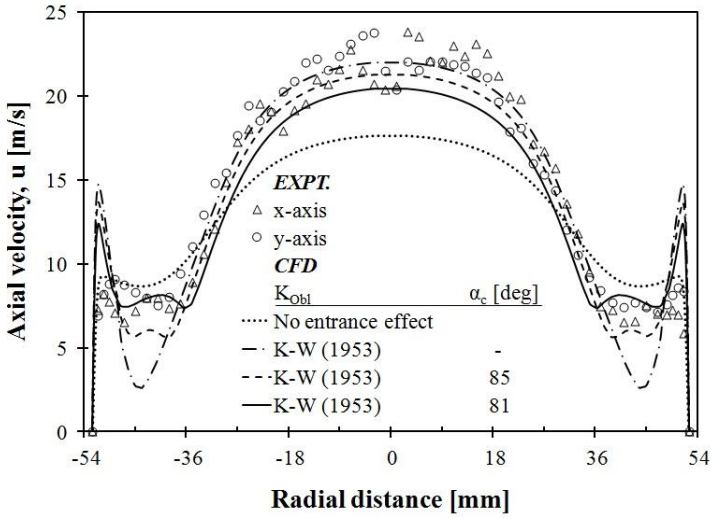

(c)

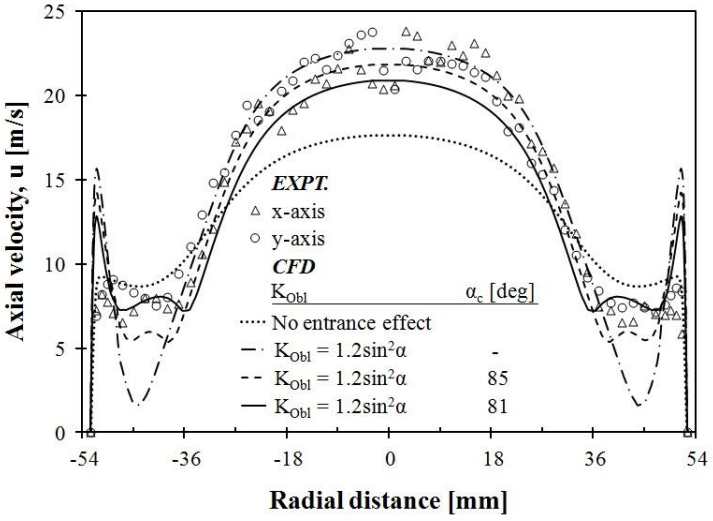

Figure 6.11: Comparison between experimental data (symbols) and CFD predictions (line curves) for the perforated monolith 600 cpsi at Re = 169270.

(a)

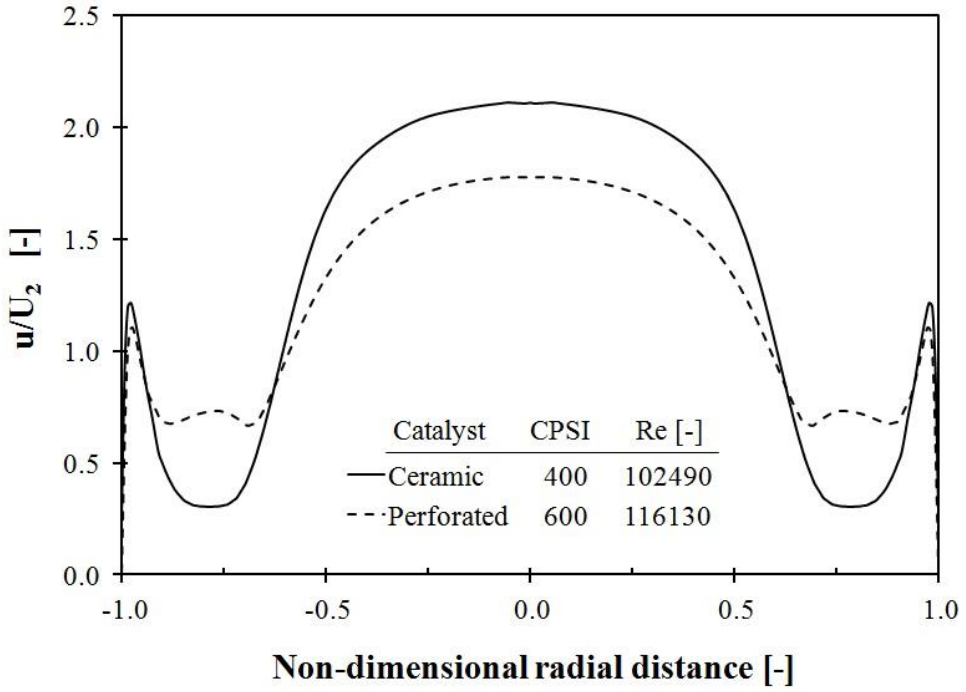

(b)

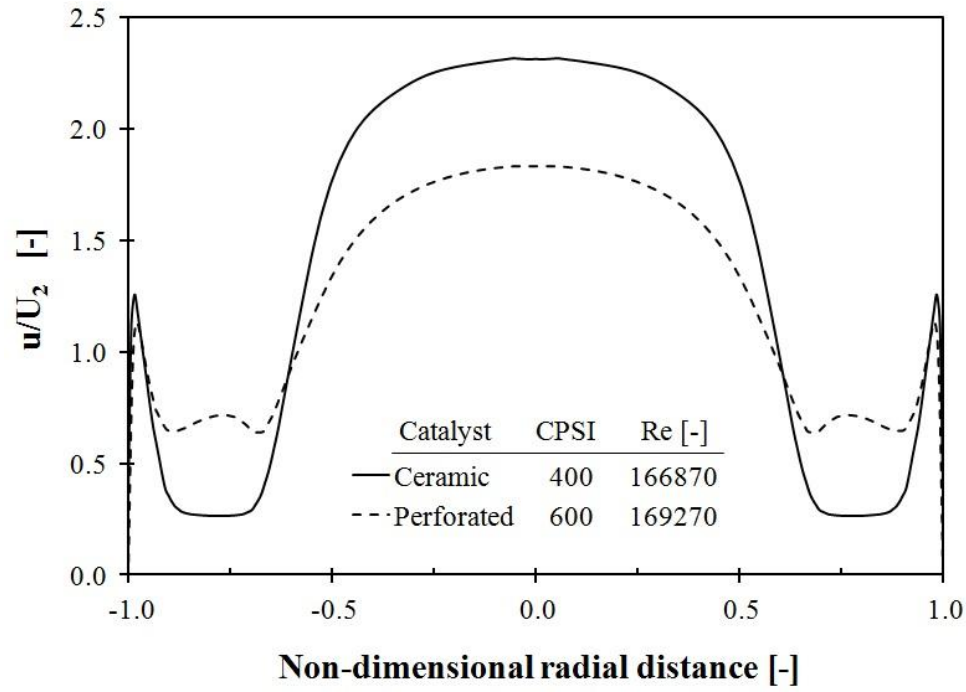

Figure 6.12: CFD predictions of the non-dimensional axial flow distribution across the ceramic and perforated catalysts.

6.5 Summary

Flow maldistribution within the axisymmetric ceramic and perforated catalysts was investigated numerically using the commercial CFD code STAR-CCM+ 7.02.008 under steady, incompressible, axisymmetric and turbulent. Modelling the flow distribution for both structures using the porous medium approach requires knowledge of axial resistance as well as transverse resistance for the perforated monolith. The former was measured by presenting uniform flow to the front face of the monoliths.

The transverse resistance was deduced by best matching CFD predictions to the measurements of the radial profiles obtained downstream of the monolith when presented with non-uniform flow at its front face. Investigations were undertaken for two axially-symmetric geometries and two different flow rates to establish the generality of the method for obtaining the resistance coefficient. Based on trial and error CFD predictions acceptably corresponded to the experimental data at $P_{i,y}$ = 125000 kg/m^4 regardless of flow rates and geometries. It shows that the perforation within the metallic monolith is uniform resulting in well distributed radial resistance. With the axisymmetric approach, fewer measurements are required to characterise the radial flow within the catalyst, whilst the computational effort to simulate the two-dimensional cases are less demanding.

CFD predictions of the flow maldistibution within the monoliths situated downstream of a conical diffuser require additional pressure losses due to the entrance effect. The losses improved the velocities in the central core region but the predictions were to low in the region of 15 mm from the wall. With the critical angle approach, the entrance effect was limited such that the losses were assumed constant above the fixed critical angle, α_c to better predict the minimum velocities. This has been verified for ceramic and perforated monoliths. The former requires the entrance effect to be restricted above $\alpha_c = 85^o$ to best predict the experimental data, whilst the losses were assumed constant above $\alpha_c = 81^o$ for the latter. This might be because the separation bubble at the monolith entrance is restricted by the different size of the channel, i.e. the smaller hydraulic diameter of perforated monolith limits the oblique entry loss to a lower incidence angle.

CHAPTER 7: CONCLUSIONS & FUTURE WORK

7.1 Introduction

The objectives of this work are to investigate the development of the pulsating flow field within a planar diffuser upstream of automotive catalysts and to validate the CFD predictions of steady-state flow maldistribution at high Reynolds numbers. The former used PIV to provide the full mapping of velocity fields inside the diffuser. The predictive study used the porous medium approach to represent the multi channel structures by a distributed resistance. Measurements were conducted to provide the simulations with validation data, pressure loss due to monolith resistance and a correction for the oblique entrance effect. In this final chapter, the conclusions from the work are presented and some suggestions for future work programme are described.

7.2 Pulsating flow studies in a planar diffuser upstream of the monoliths

Particle image velocimetry (PIV) measurements were made in the diffuser for pulsation frequencies of 50 and 100 Hz for Re ~ 2.2×10^4 and 4.2×10^4 and compared with steady flow measurements. The spatial and temporal velocity distribution at the exit of the monoliths was also recorded using hot wire anemometry (HWA). The ratio of pulse period to residence time within the diffuser (J factor) was used to characterise the flow with experiments performed for J ~ 3.5 and 6.8 and for two lengths of monolith. With steady flow, separation occurred at the inlet to the diffuser for both Re resulting in a planar jet that traversed the diffuser. On approaching the monolith it spread rapidly, part entering the monolith channels, part reversing to feed two large recirculating vortices. Significant flow restructuring occurs as the flow enters the monolith channels.

With pulsations the flow field varied throughout the cycle. Initially, as the flow accelerated, it remained attached to the diffuser walls for some distance. Separation bubbles then formed near the diffuser inlet resulting in the development of two large recirculating vortices later in the cycle. These vortices occupied the diffuser volume

at the end of the pulse before being transported out during the subsequent cycle. Flow separation occurred earlier for J = 6.8 with larger vortex structures dominating the diffuser, the flow field resembling that under steady flow conditions at the time of deceleration. Two cases with J ~ 3.5 resulted in very similar flow fields. In each, the flow was able to reattach downstream of the separation bubbles thus presenting more uniform flow to the monolith. Low Re and high frequency pulses (low J) do not permit the flow to establish sufficient inertia to provide the more dominant separated flow structures observed at high J and with steady flow. Increasing J from 3.5 to 6.8 resulted in greater flow maldistribution in the monolith; steady flow produced the highest maldistribution in all cases at the same Re. Increasing monolith resistance flattened the flow field just upstream and within the monolith for both steady and pulsating flows.

7.3 Oblique flow pressure loss

The oblique entry pressure loss was measured using a one-dimensional steady flow rig over a range of Reynolds number ($200 \leq Re_a \leq 4090$) and angles of incidence ($0^o \leq \alpha \leq 70^o$); measurements at $\alpha \geq 81^o$, although originally planned, were not possible due to limitations of the test rig (which caused skewness in the velocity profiles). The results show that the losses increased with α and Re at low mass flow rates but were independent of Re at high flow rates whereas the correlation derived by Quadri et al. (2009b) suggests there is still a Re effect. Quadri et al. (2009b) derived the correlation based on the measurements at a relatively low range of Re, i.e. $200 \leq Re_a \leq 2200$. The K-W expression shows poor predictions while M-T underestimated the losses at low angles of incidence. Comparison with Persoons et al. (2008) is not applicable as the correlation was deduced at relatively low α where the uncertainties are high. Better predictions were found if the losses are 20% higher than the transverse dynamic pressure. This expression over predicts the losses at low Re but corresponds well with the data at high mass flow rates.

7.4 Flow studies of axisymmetric ceramic and perforated catalysts

An experimental study has been performed using different axisymmetric geometries to measure the pressure drop and velocity profiles across the ceramic and perforated monolith. Pressure drop measurements were obtained across ceramic and perforated monoliths of 400/6 and 600/1.5 respectively by presenting uniform flow to its front face. The 400/6 monolith produced the lower pressure loss by virtue of its larger hydraulic diameter. Although the perforated monolith was made of thinner walls, a comparison with the 600/3.5 shows a small difference as a result of the perforation effectively causing the boundary layer to continuously reform along the length of the monolith.

Hot-wire velocity profiles were obtained downstream of three different flow assemblies, i.e. Assemblies 1, 2 and 3, at two different Reynolds numbers, i.e. 1.0×10^5 and 1.7×10^5. For Assembly 1, the ceramic and perforated monoliths, of 400/6 and 600/1.5 respectively, were placed downstream of a conical diffuser. Flow maldistribution increases with Re for both monoliths, especially for the 400/6 monolith. For the perforated monolith with high cell densities, the velocity profiles flatten as a result of higher lateral pressure gradients at the front face of the channels and the radial flow from one channel to another due to the perforation. The latter causes the magnitude of minimum velocities to be higher compared to the ceramic monolith and thus eliminates local maxima near the periphery. This pattern has never been reported before and the finding verified the benefit of the perforation effect within the monolith.

For the perforated monolith, the measurements of radial flow profiles were obtained downstream of Assemblies 2 and 3. Profiles are independent of Reynolds number over the range tested which may indicate that the perforation within the monolith is uniform. For Assembly 3, more radial flow occurred which reduces the maximum velocities at the monolith exit.

7.5 CFD predictions of the flow maldistribution across axisymmetric ceramic and perforated catalysts

Modelling the flow distribution for ceramic and perforated monoliths using the porous medium approach requires knowledge of axial resistance as well as transverse resistance for the perforated monolith. The former were measured by presenting uniform flow to the front face of the monoliths. The transverse resistance was deduced by best matching CFD predictions to the measurements of the radial profiles obtained downstream of the monolith when presented with non-uniform flow at its front face. Investigations were undertaken for two different axisymmetric geometries and two different flow rates to establish the generality of the method for obtaining the resistance coefficient. CFD predictions of the flow maldistibution were performed by adding the oblique entry pressure loss to the axial resistance to simulate the monolith losses. The critical angle approach was used to improve the predictions. The perforated 600 cpsi monolith requires the entrance effect to be restricted above $\alpha_c = 81^o$ to best predict the experimental results. While the losses were assumed constant above $\alpha_c = 85^o$ for the ceramic 400 cpsi. This might be due to the separation bubble at the monolith entrance being restricted by the different size of the channel, i.e. the smaller hydraulic diameter of perforated monolith limits the oblique entry loss to the lower incidence angle.

7.6 Original contributions

The original contributions to knowledge obtained from this study are as follows:-

a. High quality velocity vector data of pulsating flow in a two-dimensional diffuser upstream of a monolith at two different J factors has been obtained from PIV

b. Oblique angle flow measurements showed that the losses increased with α and Re. However the losses at high flow rates have no Re effect and can be predicted as 20% higher than the transverse dynamic pressure.

c. The axisymmetric assemblies at two different Re with two different geometries have been used to deduce the transverse resistance of the perforated monolith by best matching CFD predictions to measurements of the radial flow profiles obtained downstream of the monolith when presented with non-uniform flow at its front face. The profiles were found consistent regardless of flow rates and for geometrically different assemblies. The flow distribution that was predicted corresponded well to the experimental data.

d. The critical angle approach was implemented in the axisymmetric simulations with different critical angles, i.e. 81^{o} for the perforated monolith 600 cpsi and 85^{o} for the ceramic monolith 400 cpsi. This might be due to the degree of separation at the monolith entrance being restricted by the smaller hydraulic diameter of the perforated monolith thus limiting the oblique entry loss at lower incidence angle.

Overall, the objectives outlined in section 1.3 have all been achieved. The future work is presented in the following section.

7.7 Recommendations for future work

The work undertaken in this study need to be further investigated in the following areas:

Pulsating flow studies

The PIV measurements were performed in a two-dimensional diffuser upstream of a monolith in the presence of the pulsating flow in order to avoid the optical distortion in axisymmetric systems. With a thin-wall configuration, the stereoscopic PIV technique should also be performed to investigate the effect of pulsating flow within conical diffusers which are often employed in after-treatment configurations.

Flow maldistribution

In this study, the velocity distribution within the axisymmetric systems of the perforated 600 cpsi and ceramic 400 cpsi has been investigated. Hence, the effect of the perforation on the flow maldistribution has not been investigated. Investigation on the similar cell density monoliths would clearly reveal the effect of the radially open structure.

Oblique flow losses

The flow maldistribution across axisymmetric monolith catalysts with two different cell densities has been successfully predicted by restricting the entrance effect at two different critical angles. Further investigations could be performed to correlate the critical angle to the size of monolith channels. In this study, measurements of oblique entry pressure losses at $\alpha \geq 81^{o}$, although originally planned, were not possible due to limitations of the test rig (which caused skewness in the velocity profiles). Therefore an experiment technique should be found to investigate the losses at the high angles of incidence.

CFD studies

CFD studies have been performed for axisymmetric systems in this work. With the high quality velocity vector data obtained from the PIV, further simulations could be performed for the planar geometry under steady and pulsating flow to validate the CFD predictions.

REFERENCES

Apsley, D. D. and Leschziner, M. A. (2000) Advanced turbulence modeling of separated flow in a diffuser, Flow, Turbulence Combustion, 63, pp. 81 -112

Benjamin, S.F., Clarkson, R.J., Haimad, N., Girgis, N.S., (1996) An experimental and predictive study of the flow in axisymmetric automotive exhaust catalyst systems. SAE Tran. J. Fuels Lubricants. 105, (4), 1008-1019.

Benjamin, S.F., Roberts, C.A., Wollin, J., (2001) A study of the effect of flow pulsations on the flow distribution within ceramic contoured catalyst substrates. SAE Tran. J. Fuels Lubricants. 110, (4), 1380-1387.

Benjamin, S.F., Roberts, C.A., Wollin, J., (2002) A study of pulsating flow in automotive catalyst systems. Exp in Fluids. 33, 629-639.

Benjamin, S. F., Zhao, H., and Arias-Garcia, A. (2003) Predicting the flow field inside a closed-coupled catalyst-the effect of entrance effect, Proc. Instn Mech. Engrs, Vol. 217, Part C: J. Mechanical Engineering Science.

Benjamin, S.F., Disdale, W., Liu, Z., Roberts, C.A., Zhao, H., (2006) Velocity predictions from a coupled 1D/3D CFD simulation compared with measurements in the catalyst system of a firing engine. Int. J. Engine Res. 7, (1) 29-40.

Bressler, H., Rammoser, D., Neumaier, H., Terres, F., (1996) Experimental and predictive investigation of a closed coupled catalytic converter with pulsating flow. SAE paper 960564. SP-1173. SAE International Warrendale,PA.

Clarkson, R. J. (1995) A theoretical and experimental study of automotive catalytic converters, PhD thesis, Coventry University.

Durbin, P. A. (1995) Separated flow computations with the k-ε-υ^2 model. AIAA Journal, 33 (4), pp.659-664

Finn, J. E. (2005) How to measure turbulence with hot-wire anemometers – A practical guide, Dantec Dynamics. Skovlunde, Denmark.

Haimad, N. (1997) A theoretical and experimental investigation of the flow performance of automotive catalytic converter, PhD thesis, Coventry University

Howitt, J.S. and Sekella, T.C., (1974) Flow effects in monolithic honeycomb catalytic converters. SAE Paper 740244

Hwang, K., Lee, K., Mueller, J., Stuecken, T., Schock, H.J., Lee, J-C., (1995) Dynamic flow study in a catalytic converter using laser doppler velocimetry and high speed flow visualisation. SAE paper 950786. SP-1094 Global Emission experiences:processes, measurements, and substrates. SAE International Warrendale, PA.169-186.

Iaccarino, G. (2001) Predictions of turbulent separated flow using commercial CFD codes, J. Fluids Eng, 123(4), pp. 819-828

Ilgner, F., Nau, M., Harndorf, H., Benninger, K., Schiessl, R., Maas, U., Dreizler, A., (2001) Analysis of flow patterns inside an autothermal gasoline reformer. SAE Paper 2001-01-1917.

Kaiser, R., Stadler, F., Pace, L., and Presti, M. (2007) Simulation model of the three-way catalysts with perforated foils. MTZ worldwide eMagazine, Volume 68, http://www.atzonline.com.

Kaltenbach, H. J., Fatica, M., Mittal, R. Lund, T. S. and Moin, P. (1999) Study of the flow in a planar asymmetric diffuser using large eddy simulations, J. Fluid Mech., 390, pp. 151-185

King, C.V., Smith, B.L., (2011) Oscillating flow in a 2D diffuser. Exp Fluids. 51, (6) 1577-1590.

Küchemann, D. and Weber, J. (1953) Aerodynamics of propulsion, Mc-Graw Hill, New York.

Liu, Z., Benjamin, S.F., Roberts, C.A., (2003) Pulsating flow maldistribution within an axisymmetric catalytic converter-flow rig experiment and transient CFD simulation. SAE 2003-01-3070, SP-1801 SAE International Warrendale, PA.

Lotti, C., Rossi, V., Poggio, L., Holzinger, M., Pace, L., and Presti, M. (2005) Backpressure optimized closed coupled PE catalyst- First application on a Maserati powertrain, SAE Paper 2005-01-1105.

Moore, F. K. and Torrence, K. E. (1977). Air flow in dry natural-drought cooling towers subject to wind. Cornell Energy multiple-tube systems, Cornell Energy report, Ithaca, New York.

Morel, T. (1975) Comprehensive design of axisymmetric wind tunnel contractions, Journal of fluids engineering, Trans. ASME, Series I, Vol. 97, pp. 225-233

Morel, T. (1977) Design of two-dimensional wind tunnel contractions, Journal of fluids engineering, Trans. ASME, pp. 371-378

Park, S-B., Kim, H-S., Cho, K-M., Kim, W-T., (1998) An experimental and computational study of characteristics in exhaust manifold and CCC (closed coupled catalyst). SAE paper 980128.

Persoons, T., Van den Bulk, E., Fausto, S. (2003) Study of pulsating flow in a close-coupled catalyst manifold using phase-locked hot-wire anemometry. Exp Fluids. 36, (2) 217-232.

Persoons, T., Vanierschot, M, Van den Bulck, E., (2008) Oblique inlet pressure loss for swirling flow entering catalyst substrate. Exp. Therm. Fluid Sci. 32, 1223-1231.

Quadri, S.S., Benjamin, S.F., Roberts, C.A., (2009a) Flow measurements across an automotive catalyst monolith situated downstream of a planar wide-angled diffuser. Proc IMechE Vol. 224, Part C, J. Mechanical Engineering Science. 321-328.

Quadri, S.S., Benjamin, S.F., Roberts, C., (2009b) An experimental investigation of oblique entry pressure losses in automotive catalytic converters . Proc IMechE. 223, (11), Part C, J. Mechanical Engineering Science,2561-2569.

Rafell, M., Willert, C, Kompenhaus, J., (1998) Particle image velocimetry, Springer, Berlin

Schetz, J. A. and Fuhs, A. E. (1999) Fundamental of fluid mechanics, John Wiley and Sons, pp. 519-523.

Shah, R. K. (1978) A correlation for laminar hydrodynamic entry length solutions for circular and non-circular ducts, Trans. ASME, J. Fluids Eng., pp. 177-179

Shuai, S-J., Wang, J-X., Dong, Q-L., Zhang, R-J., (2001) PIV measurement and numerical simulation of flows in automotive catalytic converters. SAE paper 2001-01-3494.

Smith, B.L. & King, C.V., (2007) Time-resolved PIV and pressure measurements of oscillating and pulsating in a rapid expansion, Paper no.FEDSM2007-37257, pp. 1223-1232, Proceeding of FEDSM2007 5th Joint ASME/JSME Fluids Engineering Conference San Diego, USA.

Stratford, B. S. (1959) The prediction of separation of the turbulent boundary layer, Journal of Fluid Mechanics, Vol. 5, pp. 1-16

STAR-CCM+ user guide, version 7.02.008, (2012) CD-Adapco

Turner, C., Thornhill, D, McCullough, G., (2011) Comparison of experimental PIV data and CFD simulations for flow in a Diesel particulate filter inlet diffuser. SAE paper 2011-01-1241.

TSI Instruction Manual: Model 9306 Six-Atomizer. (2000)

Weltens, H., Bressler, H., Terres, F., Neumaier, H., Rammoser, D., (1993). Optimisation of catalytic converter gas flow distribution by CFD predictions, SAE paper 930780.

Zhao, F-Q., Bai, L., Liu, Y., Chue T-H, and Lai, M-C. (1997) Transient flow characteristics inside the catalytic converter of a firing gasoline engine. SAE paper 971014. Reprinted from SP-1248: Issues in Emissions Control Technology, SAE International, Warrendale, PA, 175 –188.

Zygourakis, K., (1989) Transient operation of monolith catalytic converters: a two-dimensional reactor and the effects of radially non-uniform flow distributions, Chem. Engng. Sci. 44 (9) 2075-2086.

APPENDICES

Appendix A: Experimental conditions

a. Pulsating flow measurements

			PIV		HWA	
Case	f [Hz]	L [mm]	Re x 10^{-4}	J [-]	Re x 10^{-4}	J [-]
1	50	27	2.24	3.6	2.18	3.5
2	50	100	2.25	3.6	2.19	3.6
3	50	27	4.19	6.8	4.1	6.8
4	50	100	4.19	6.8	4.12	6.8
5	100	27	4.16	3.4	4.09	3.4
6	100	100	4.21	3.4	4.12	3.4
7	0	27	2.24	-	2.19	-
8	0	100	2.24	-	2.19	-
9	0	27	4.29	-	4.16	-
10	0	100	4.29	-	4.18	-
11	0	27	6.10	-	6.05	-
12	0	100	6.10	-	6.05	-

b. Oblique flow loss measurements; L [mm] = 17 and 27

α [deg]	Re_a										
0	200	390	890	1580	1930	2240	2640	3050	3280	3520	4090
27											
41											
51											
61											
70											

c. Flow studies of axisymmetric systems

i) Pressure drop

	Re_c
Ceramic 400 cpsi	190, 430, 1040, 1440, 2080 and 2260
Perforated 600 cpsi	140, 250, 360, 450, 550, 660, 770, 880, 990, 1110 and 1250
Ceramic 600 cpsi	380, 740, 1070, 1400, 1710 and 1980

ii) Flow distribution

Case	Assembly	Monolith	L [mm]	Re x 10^{-4}	
1	1	Ceramic 400 cpsi	75	10.25	11.61
2	1	Perforated 600 cpsi	70	16.69	16.93
3	2	Perforated 600 cpsi	70	3.08	6.27
4	3	Perforated 600 cpsi	70	3.09	6.31

Appendix B: Design of 2-D nozzle using Morel's method (1977)

Figure B-1: Wall contour made of two cubic arcs (Morel 1977)

The design steps involved were as follows:

Step 1 : Selecting CR (2 ≤ CR ≤4)

$$CR = \frac{A_1}{A_2} = \frac{H_1.b}{H_2.b} = \frac{H_1}{H_2} \qquad (B1)$$

CR = 4, H_2 = 24 mm, hence H_1 = 24 x 4 = 96 mm

Step 2 : Selecting C_{pi} and C_{pe}

Separation will occur at the wide end of the nozzle when (Stratford (1959)):

$$C_{pi} = 0.7\left(\frac{x_0 + 0.9x_i}{s}\right)^{-1/3} (10^{-6}\,Re)^{1/15} \qquad (B2)$$

$x_0 / H_1 = 0.3$, $x_i / H_1 = 0.25$, $s / H_1 = 0.09$, $Re = 1.0x10^6$ (Re is based on H_1)

$$\text{Hence,} \quad C_{pi} = 0.7\left(\frac{0.525}{0.09}\right)^{-1/3} (10^{-6} * 1.0x10^6)^{1/15} = 0.44$$

Practically, flow non-uniformity, $\tilde{u}_2 \leq 2\%$ at the narrow end and for cubic nozzles, $C_{pe} = 5.3\tilde{u}_2$

$$\text{Considering } \tilde{u}_2 = 1\%, \text{ Hence } C_{pe} = 0.01x5.3 = 0.053$$

Step 3 : Reading off values of F_e and G_i

From Figure B-2: When C_{pe} = 0.053, F_e = 0.202When C_{pi} = 0.44, G_i = 1.978

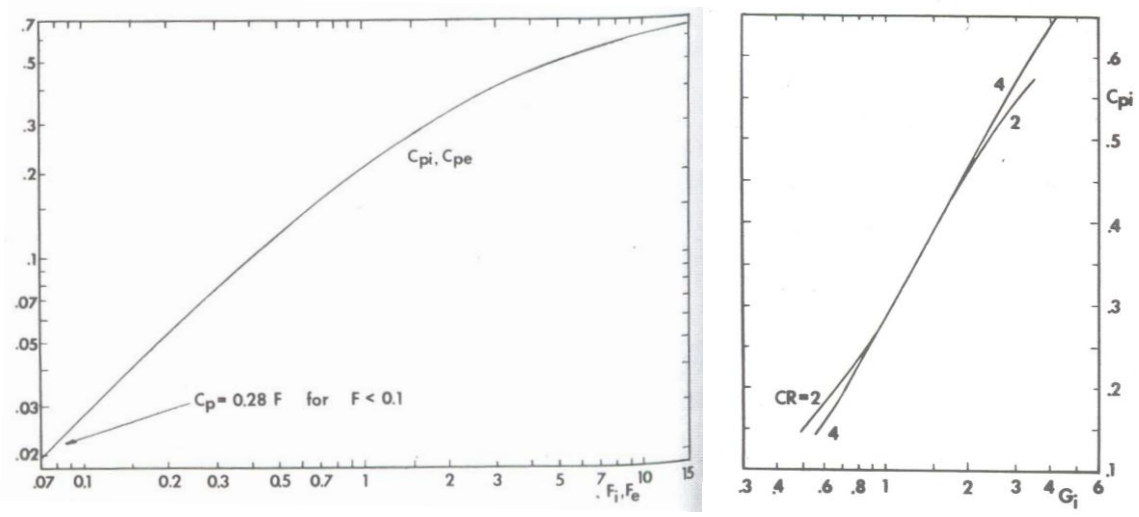

Figure B-2: Dependence of Cpi, Cpe and C_{pi} on F_i and F_e and G_i

Step 4 : Solving for X (0.2 ≤ X ≤ 0.8)

$m = H_1 / H_2 = 96/24 = 4$

$$X^{1/2}(1-X)^{-2/3} = F_e^{1/3} G_i^{-1/2} m^{1/2}(m-1)^{1/6} \qquad \text{(B3)}$$

$$X^{1/2}(1-X)^{-2/3} = 0.202^{1/3} 1.978^{-1/2} 4^{1/2}(4-1)^{1/6} = 1.002$$

From Figure B-3: When $X^{1/2}(1-X)^{-2/3}$ = 1.002, X = 0.451

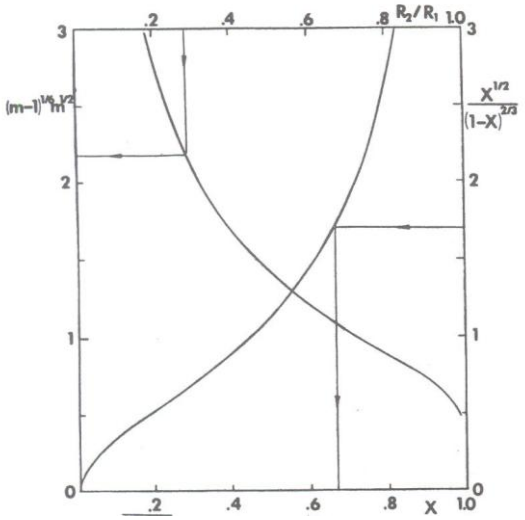

Figure B-3: Graphical aid for evaluation of X

Step 5 : Calculating L ($0.85 \leq L/H_1 \leq 1.5$)

$$F_e = (m-1)m^{-3}(1-X)^{-2}(L/H_1)^{-3} \quad \text{(B4)}$$

$$0.202 = (4-1)4^{-3}(1-0.451)^{-2}(L/H_1)^{-3}$$

$$L/H_1 = 0.88, \quad L = \underline{84.281 \text{ mm}}$$

Step 6 : Calculating the total length, Lt

$$L_t = L + a_1 D_1 + a_2 D_2 \quad \text{(B5)}$$

$$a_1 = 0.5,\ a_2 = 0.5,\ L_t = 84.281 + 0.5*96 + 0.5*24 = \underline{96.281 \text{ mm}}$$

Step 7 : Obtaining the contour coordinates

$$\frac{H-H_2}{H_1-H_2} = 1 - \frac{1}{X^2}\left(\frac{x}{L}\right)^3,\ x/L \leq X \text{ and } \frac{H-H_2}{H_1-H_2} = \frac{1}{(1-X)^2}\left(1-\frac{x}{L}\right)^3,\ x/L > X$$

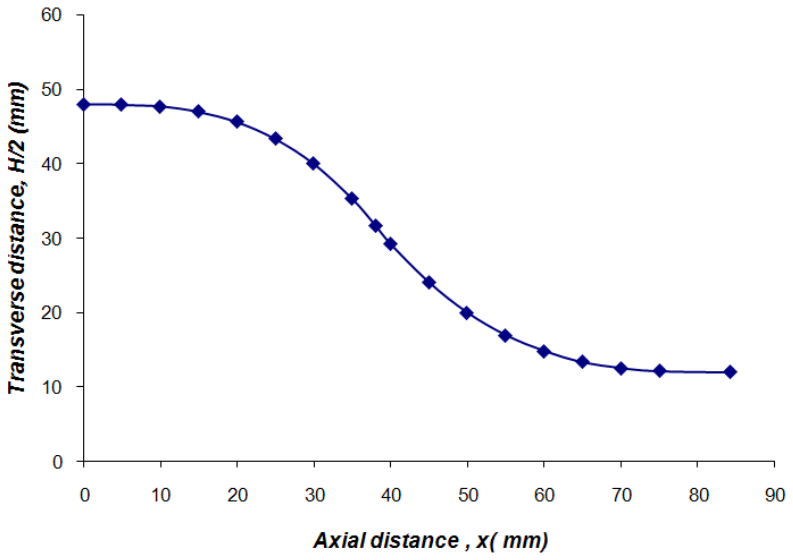

Figure B-5: Wall shape contour of the two-dimensional nozzle

Appendix C: Velocity inlet comparison between PIV and HWA

a)

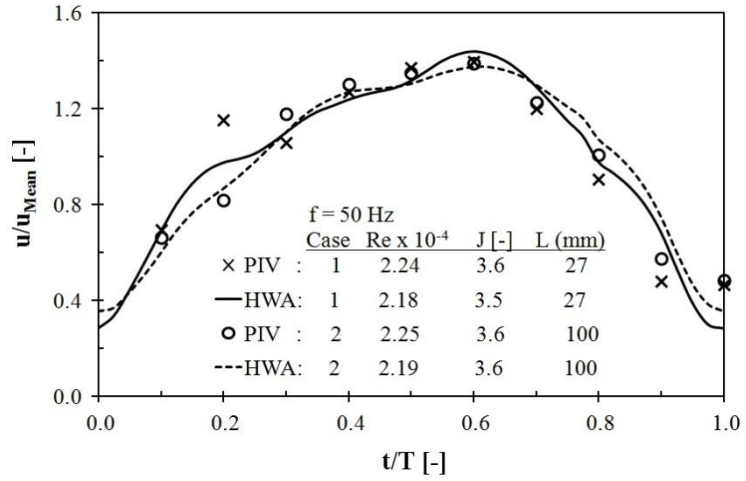

b)

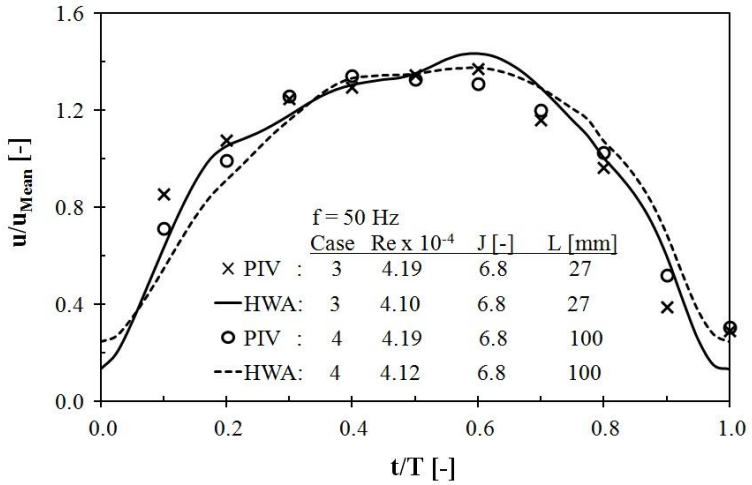

c)

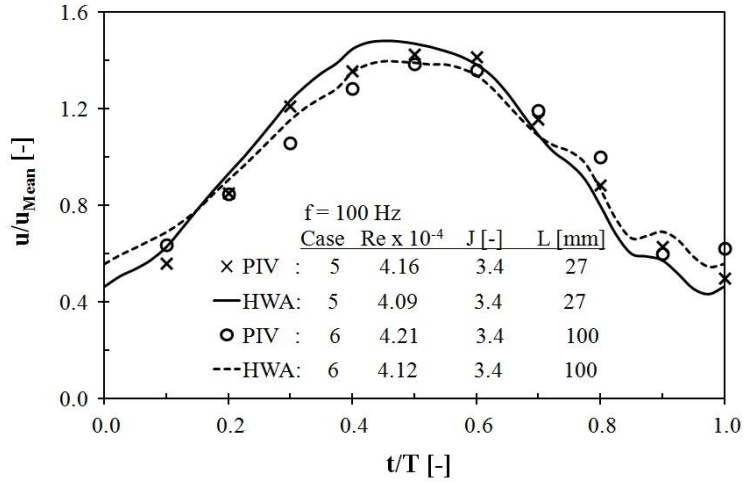

Figure C-1: PIV and HWA inlet pulse shapes observed at centre of the nozzle exit

Appendix D: Effect of sample size on the flow fields

In this study, PIV has been used to obtain mean flow fields by collecting a large number of instantaneous vector maps and ensemble averaged them. The effect of sample size, N was investigated for steady and pulsating flow based on total sample size of 100, the latter case at t/T = 0.8, f = 100 Hz as it has a strong unsteady behaviour. The examinations are conducted for a monolith length of 27 mm and a Reynolds number of ~ 4 x 10^4 based on the inlet velocity and the hydraulic diameter of the inlet duct.

Figures D-1 and D-2 compare the instantaneous and the mean flow fields under steady and pulsating flow respectively. For both cases the instantaneous results reveal a strong unsteady behaviour of the recirculating vortices due to the flow separation at the diffuser inlet and the reverse flow that feeds the recirculation just upstream of the monolith. Meanwhile the mean flow fields remove the unsteadiness and only show the steady shape of the recirculation which aids data interpretation.

The convergence of the average PIV data was checked by examining the velocity contours with different number of samples, i.e. N = 25, 50, 75 and 100. A large change in the flow contours was expected for low N values and a smooth contour can be observed when the flow fields have been completely resolved. Figure D-3 shows the convergence plots presented for time-averaged and phase-averaged velocity fields.

The results show that a sample size of 25 is adequate to resolve the flow fields for both steady and pulsating flow. It was concluded that a converged measurement was obtained after the number of samples reaches 75 and 100 as the true-mean flow. Nevertheless the sample size of 100 was used throughout this study to achieve a high quality data.

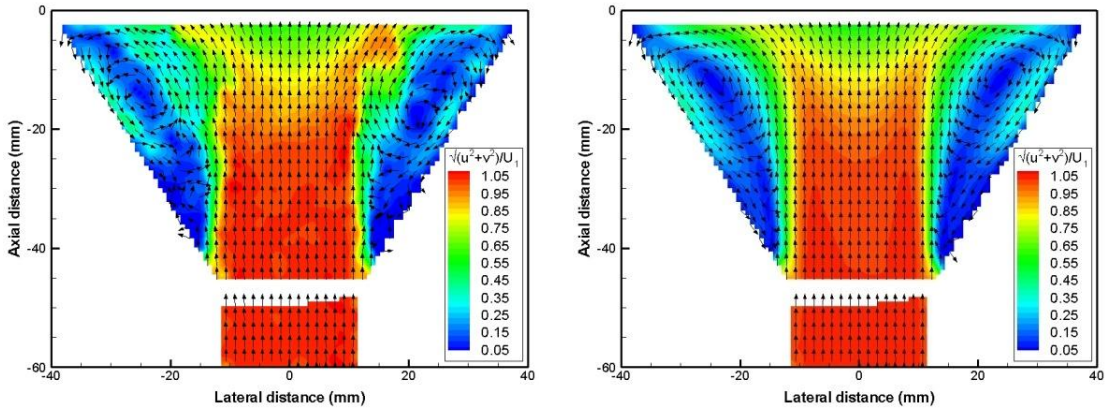

Figure D-1: Steady flow normalised vector fields a) N = 1 and b) N = 100

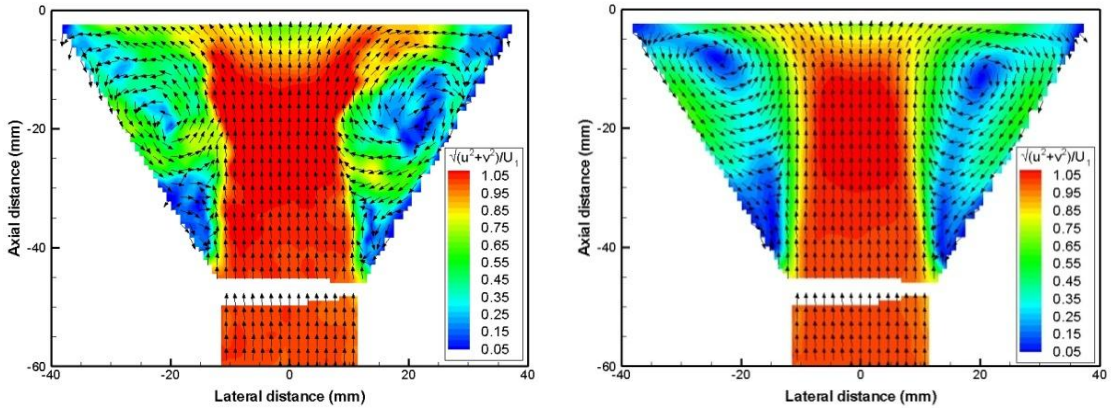

Figure D-2: Pulsating flow normalised vector fields at f = 100 Hz, t/T = 0.8; a) N = 1 and b) N = 100

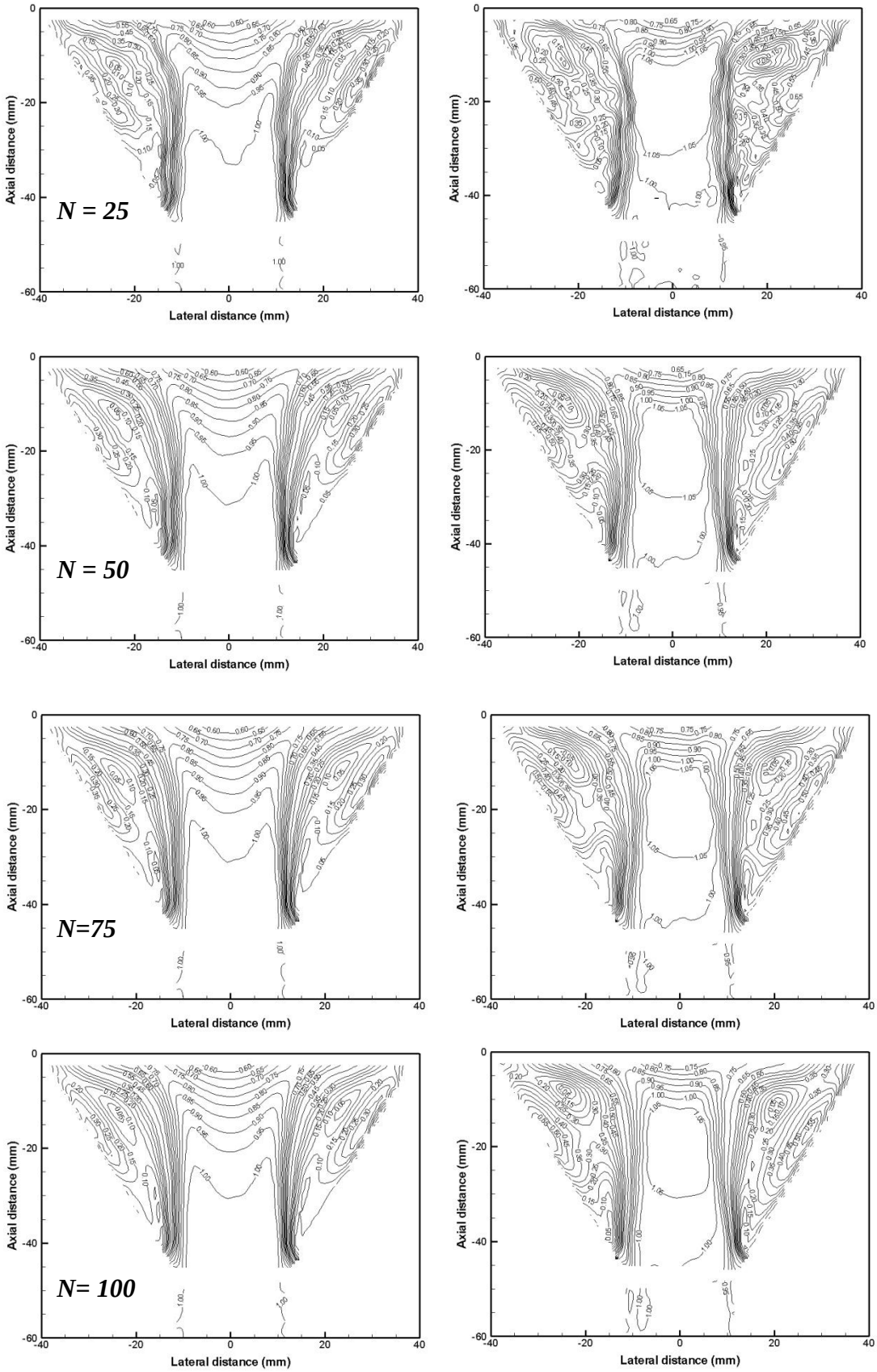

a) Steady flow b) Pulsating flow

Figure D-3: Velocity contours at various N; a) Steady flow, b) Pulsating flow

Appendix E: Design of an axisymmetric nozzle using Morel's method (1975)

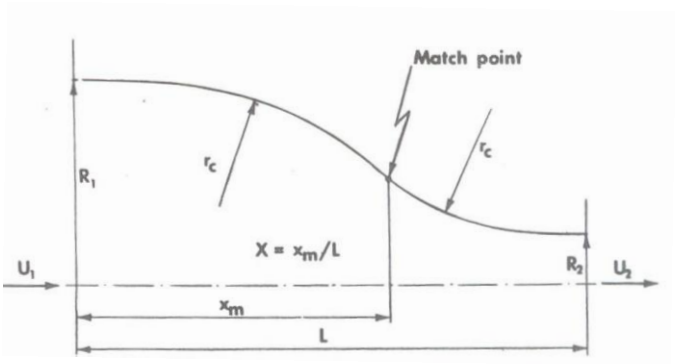

Figure E-1: Wall contour constructed of two matched cubic arcs

The design steps involved were as follows:

Step 1 : Selecting CR (2 ≤ CD ≤ 25)

$$CR = \frac{\pi D_1^{\,2}/4}{\pi D_2^{\,2}/4} = \frac{D_1^{\,2}}{D_2^{\,2}} \qquad \text{(E1)}$$

Knowing $D_2 = 24$ mm and $D_1 = 115$ mm

Hence, $CR = \frac{24^2}{115^2} = 22.960 \approx 23$

Step 2 : Selecting C_{pi} and C_{pe} ($C_{pi} > 0.1$ and $C_{pe} < 0.1$)

Separation will occur at the wide end of the nozzle when (Stratford (1959)):

$$C_{pi} = 0.7\left(\frac{x_0 + 0.9x_i}{s}\right)^{-1/3}(10^{-6}\,Re)^{1/15} \qquad \text{(E2)}$$

$x_0/D_1 = 0.3$, $x_i/D_1 = 0.15$, $s/D_1 = 0.09$, $Re = 1.0 \times 10^6$ (Re is based on D_1)

Hence, $C_{pi} = 0.7\left(\frac{0.435}{0.09}\right)^{-1/3}(10^{-6} * 1.0x10^6)^{1/15} = \underline{0.41}$

Practically, flow non-uniformity, $\tilde{u}_2 \leq 2\%$ and for cubic nozzles, $\tilde{u}_2 \approx 0.35 C_{pe}$

Considering $\tilde{u}_2 = 2\%$, Hence $C_{pe} = 0.02/0.35 = \underline{0.06}$

Step 3 : Reading off values of F_e and G_i

From Figure E-2: When $C_{pe} = 0.06$, $C_{pi} = 0.41$ $F_e = 0.546$, $G_i = 2.229$

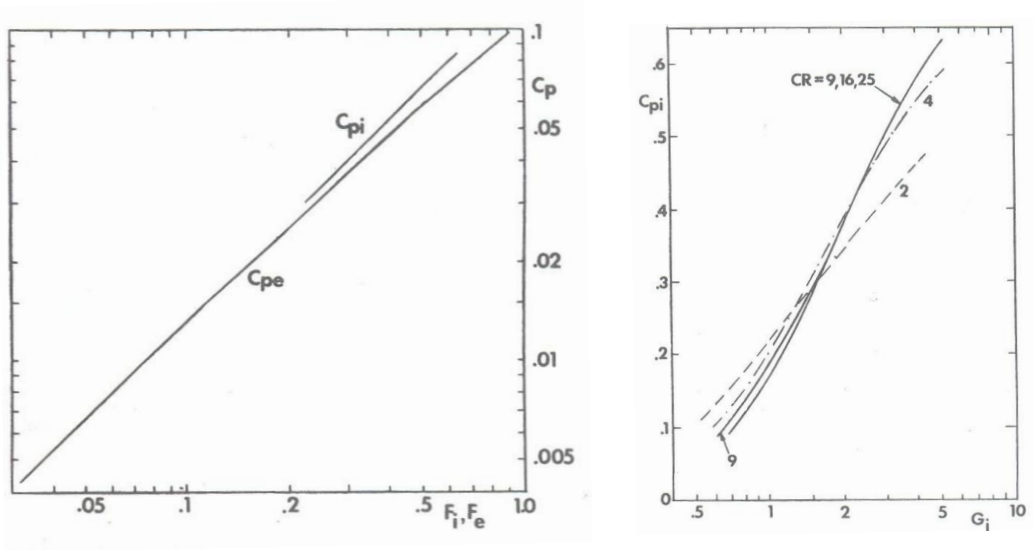

Figure E-2: Dependence of C_{pi} and C_{pe} on F_i and F_e and G_i

Step 4 : Solving for X ($0.2 \leq X \leq 0.8$)

$$m = D_1 / D_2 = 115/24 = 4.792$$

$$X^{1/2}(1-X)^{-2/3} = F_e^{1/3} G_i^{-1/2} m^{1/2} (m-1)^{1/6} \qquad \text{(E3)}$$

$$X^{1/2}(1-X)^{-2/3} = 0.546^{1/3}.2.229^{-1/2} 4.792^{1/2} (4.792-1)^{1/6} = 1.496$$

From Figure E-3: When $X^{1/2}(1-X)^{-2/3} = 1.496$, X = 0.619

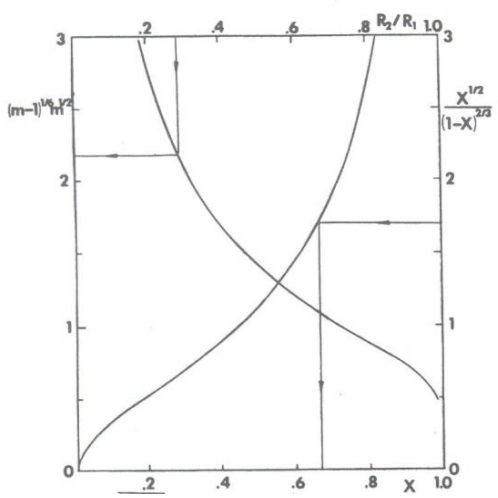

Figure E-3: Graphical aid for evaluation of X

Step 5 : Calculating L ($0.75 \leq L/D_1 \leq 1.25$)

$$G_i = (m-1)m^{-1}X^{-1}(L/D_1)^{-2} \qquad \text{(E4)}$$

$$2.229 = (4.792-1)*4.792^{-1}*0.619^{-1}(L/D_1)^{-2}$$

$$L/D_1 = 0.76, \qquad L = \underline{87.105}$$

Step 6 : Calculating the total length, L_t

$$L_t = L + a_1D_1 + a_2D_2 \qquad \text{(E5)}$$

$$a_1 = 0.2 \quad a_2 = 0.3$$

Hence, $L_t = 87.105 + 0.2*115 + 0.3*24 = \underline{94.305 \text{ mm}}$

Step 7 : Obtaining the contour coordinates

$$\frac{D-D_2}{D_1-D_2} = 1 - \frac{1}{X^2}\left(\frac{x}{L}\right)^3 \quad , \; x/L \leq X \qquad \text{(E6)}$$

$$\frac{D-D_2}{D_1-D_2} = \frac{1}{(1-X)^2}\left(1-\frac{x}{L}\right)^3 , \; x/L > X \qquad \text{(E7)}$$

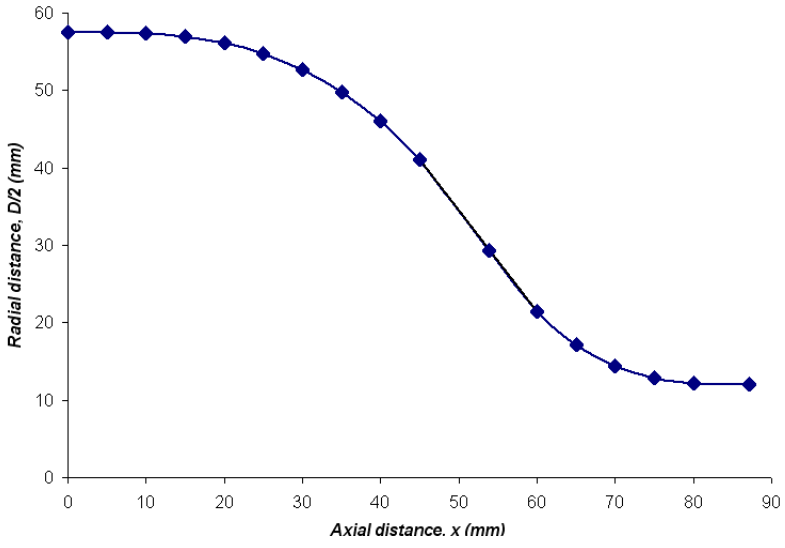

Figure E-4: Wall shape contour of the axisymmetric nozzle

Appendix F: PIV results

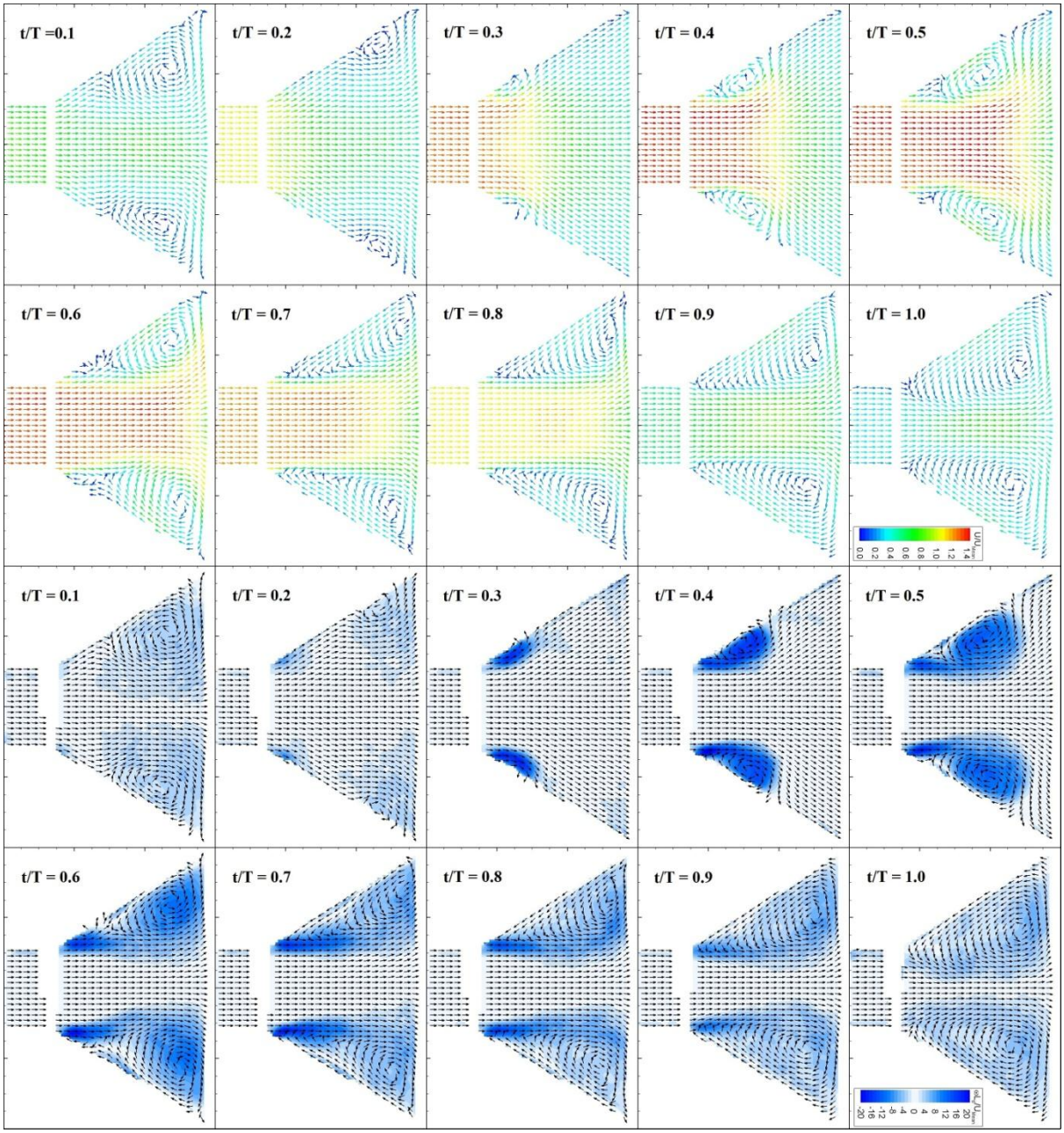

Figure F-1: Normalised phase-averaged velocity vector and vorticity fields for Case 4 at J = 6.8 (Re = 4.2 x 10^4, f =50 Hz, L = 100 mm). Fields are normalised by the cycle-averaged mean inlet velocity

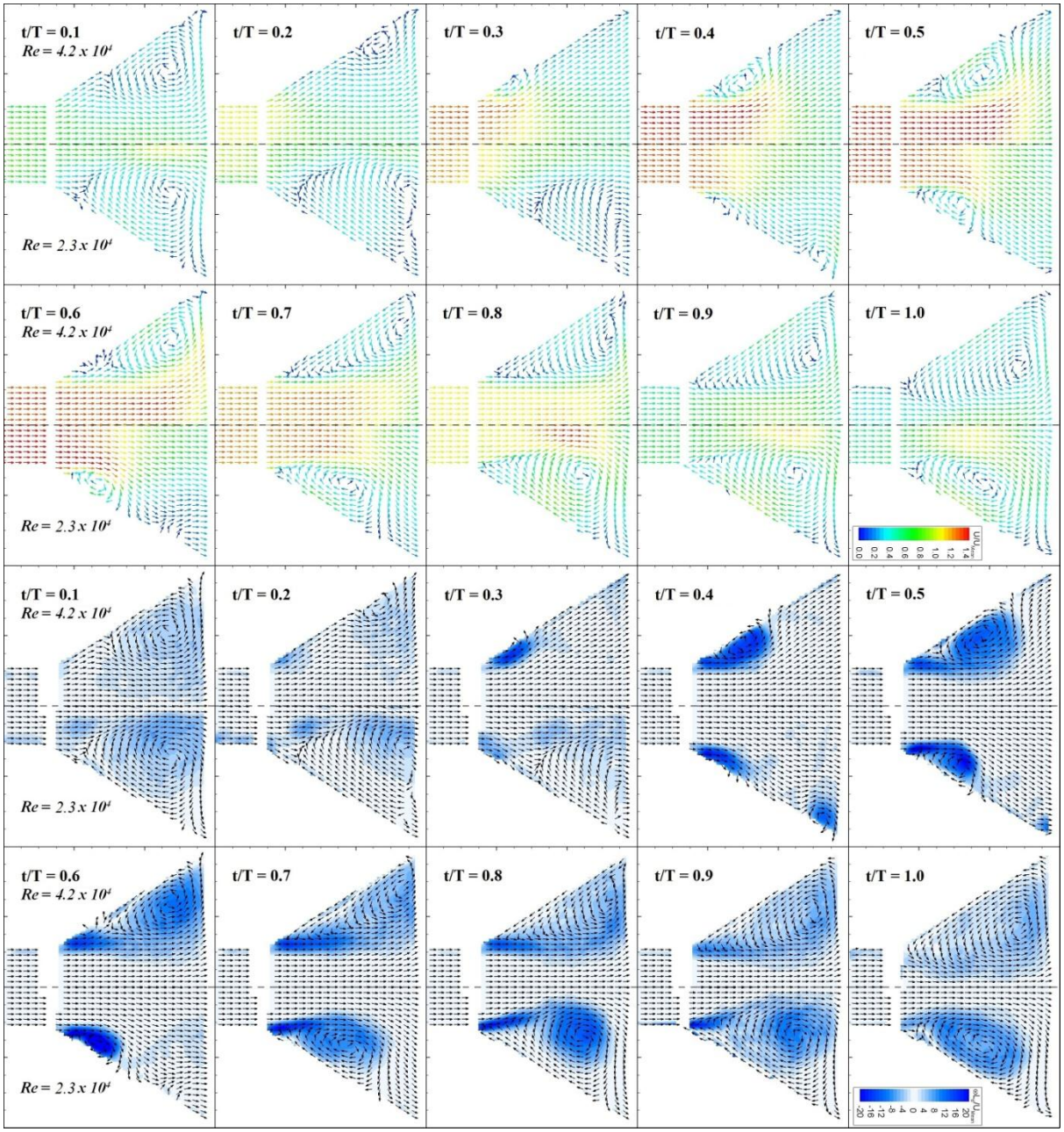

Figure F-2: Normalised phased averaged velocity and vorticity fields for Case 2 (J = 3.6, Re = 2.2 x 10^4, 50 Hz) and Case 4 (J = 6.8, Re = 4.2 x 10^4, 50 Hz) for L = 100 mm. Fields are normalised by the cycle-averaged mean inlet velocity

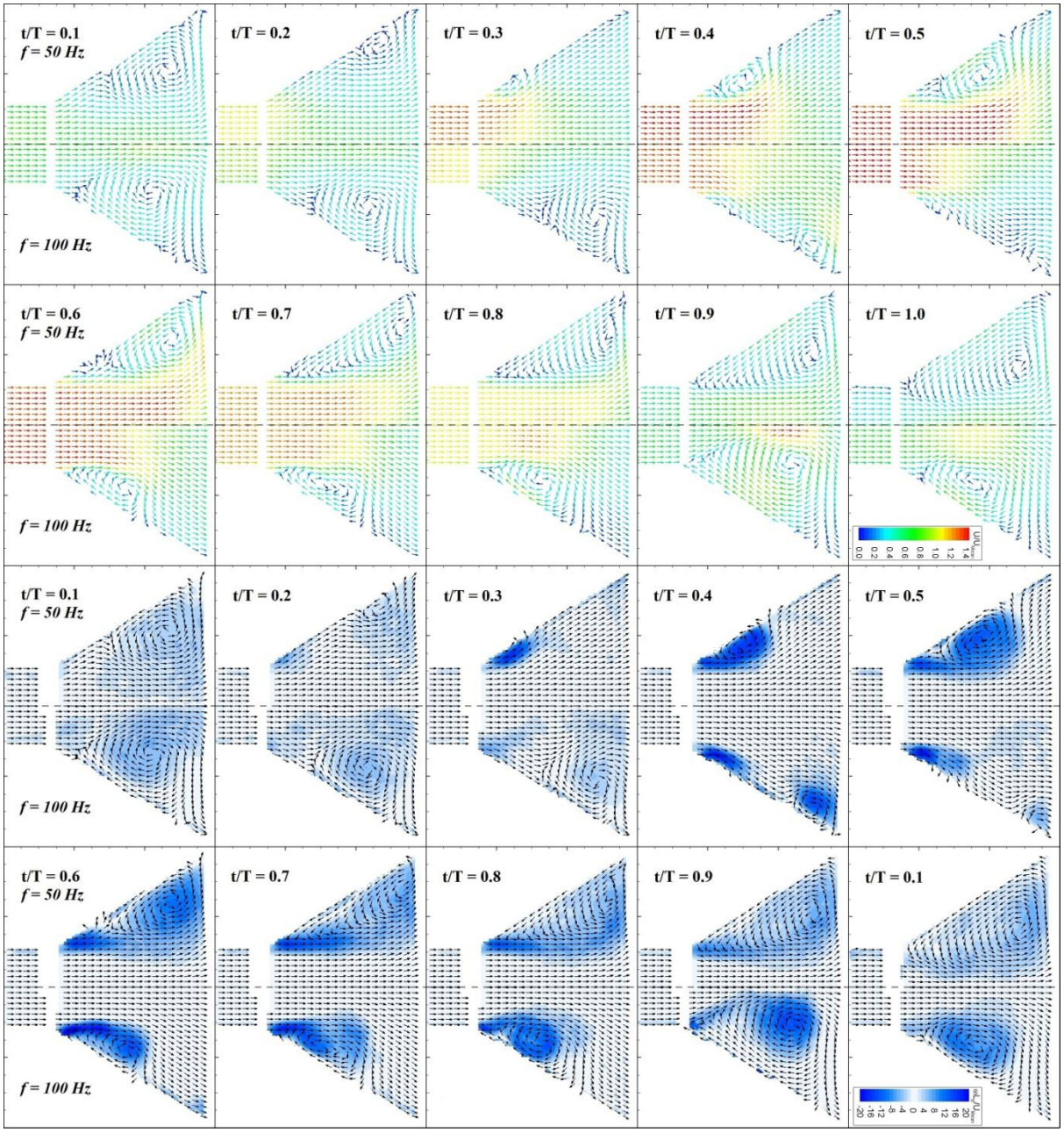

Figure F-3: Normalised phase-averaged velocity and vorticity fields for Case 4 (J = 6.8, Re = 4.2 x 10^4, 50 Hz) and Case 6 (J = 3.4, Re = 4.2 x 10^4, 100 Hz) for L = 100 mm. Fields are normalised by the cycle-averaged mean inlet velocity

Appendix G: Error calculations for the entrance effect study

The Furness Controls pressure transmitter Model FCO318-4W (± 10 kPa) has an accuracy of ±0.25% reading and was used to measure the pressure drop across monoliths. U_1 was measured using HWA with uncertainty of ±1%.

An error calculation for $\alpha = 30^O$, L = 27 mm and Re_a= 4065 is shown below

a. Monolith pressure drop, P_L

For L = 27 mm, P_L is given by

$$P_L = 1.116U_2^2 + 21.094U_2$$

At Re = 4065, U_2 = 38.252 m/s is obtained from HWA and has an error of ±1%.

$$P_L = (1.116*(38.252^2))\ (\pm 2\%) + (21.094*38.252)\ (\pm 1\%)$$

$$= (2440 \pm 41)\ \text{Pa}$$

$$= 2440\ \text{Pa} \pm 1.6\%$$

b. Oblique pressure drop, P_{Obl}

From Equation, P_{Obl} is given by

$$P_{Obl} = (P_{S1} - P_{S2}) + \frac{1}{2}\rho\left(U_1^2 - U_2^2\right) - P_L$$

= 2533(±0.25%) + 0.5*1.194*[(42.931^2)(±2%) - (38.252^2)(±2%)] –2440(±1.6%)

= (320 ± 87) Pa or 320 Pa ±27%

Appendix H: Derivations of field functions in STAR-CCM+

During simulations, the field functions were used to calculate the oblique entry loss for flow entering the monolith. Tables F-1 and F-2 show the parameters required to simulate the flow maldistribution across the axisymmetric ceramic monolith 400 cpsi. The parameters are defined as follows:-

Pv = Total axial viscous resistance [kg/m^{3}s]

ua = Approach velocity [m/s]

alfa = Incidence angle [deg]

alfacrit = Critical incidence angle [deg]

sin2alfa = $\sin^2\alpha$ [-]

Viscosity = Kinematic viscosity [m^2/s]

Porosity = Void fraction of catalyst [-]

L = Monolith length [m]

dh = Hydraulic diameter of the monolith channel [m]

Dens = Air density [kg/m^3]

Rea = Approach Reynolds number [-]

Table H-1: Simulations for with K-W correlation, no critical angle, i.e. $\alpha_c \sim 90^o$

Function name	Definition
Pv	568.332+$K-W
K-W	0.5*$Dens*pow($ua,2)*$sin2alfa/$L/$$Velocity[0]
alfa	atan($$Velocity [1]/$$Velocity[0])*180/3.142
alfacrit	89.99
sin2alfa	$alfa< $alfacrit ? pow(sin($alfa*3.142/180),2) : pow(sin($alfacrit*3.142/180),2)
ua	$alfa< $alfacrit ? pow(pow($$Velocity[0]/cos($alfa*3.142/180),2),0.5): pow(pow($$Velocity[0]/cos($alfacrit*3.142/180),2),0.5)
Viscosity	0.00001489
Dens	1.211
dh	0.001117
L	0.075

Table H-2: Simulations with Quadri et al. (2009b) correlation, $\alpha_c = 81^o$

Function name	Definition
Pv	568.332+$Quadri
Quadri	$alfa< 45 ? 0.5*$Dens*pow($ua,2)*0.021*pow($Rea,0.5)*$sin2alfa/$L/$$Velocity[0]: $alfa< 55 ? 0.5*$Dens*pow($ua,2)*0.06*pow($Rea,0.37)*$sin2alfa/$L/$$Velocity[0]: $alfa< 70 ? 0.5*$Dens*pow($ua,2)*0.18*pow($Rea,0.24)*$sin2alfa/$L/$$Velocity[0]: 0.5*$Dens*pow($ua,2)*0.525*pow($Rea,0.1)*pow(sin($alfa*3.142/180),2)/$L/$$Velocity[0]
alfa	atan($$Velocity [1]/$$Velocity[0])*180/3.142
alfacrit	81
Rea	$ua*$dh/($Porosity*$Viscosity)
sin2alfa	$alfa< $alfacrit ? pow(sin($alfa*3.142/180),2) : pow(sin($alfacrit*3.142/180),2)
ua	$alfa< $alfacrit ? pow(pow($$Velocity[0]/cos($alfa*3.142/180),2),0.5): pow(pow($$Velocity[0]/cos($alfacrit*3.142/180),2),0.5)
Viscosity	0.00001489
Dens	1.211
dh	0.001117
L	0.075
Porosity	0.774

Appendix I: Macro for STAR-CCM+ simulations

```
// STAR-CCM+ macro: kamal.java
package macro;

import java.util.*;

import star.common.*;
import star.base.neo.*;

public class kamal extends StarMacro {

  public void execute() {
    execute0();
  }

  private void execute0() {

    Simulation simulation_0 =
      getActiveSimulation();

for (int i = 0;i<5000;i++)
          {
    simulation_0.getSimulationIterator().step(1);

    simulation_0.getSimulationIterator().step(1);

    simulation_0.getSimulationIterator().step(1);

    simulation_0.getSimulationIterator().step(1);

    simulation_0.getSimulationIterator().step(1);

    XyzInternalTable xyzInternalTable_0 =
      ((XyzInternalTable) simulation_0.getTableManager().getTable("ploss"));

    xyzInternalTable_0.extract();
       }
  }
}
```